An artificial intelligence approach for biomass devolatilisation in an industrial CFD model with advanced turbulence-chemistry interaction

by

Philip du Toit

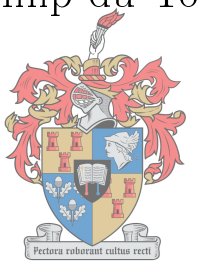

UNIVERSITEIT
iYUNIVESITHI
STELLENBOSCH
UNIVERSITY

Dissertation presented for the degree of Doctor of Philosophy in the Faculty of Engineering at Stellenbosch University

Supervisor: Prof. Chris Meyer
Co-supervisor: Dr. Ryno Laubscher

March 2018

Declaration

By submitting this dissertation electronically, I declare that the entirety of the work contained therein is my own, original work, that I am the sole author thereof (save to the extent explicitly otherwise stated), that reproduction and publication thereof by Stellenbosch University will not infringe any third party rights and that I have not previously in its entirety or in part submitted it for obtaining any qualification.

Date: March 2018 .....

UNIVERSITEIT•STELLENBOSCH•UNIVERSITY
jou kennisvennoot • your knowledge partner

Plagiaatverklaring / Plagiarism *Declaration*

1 Plagiaat is die oorneem en gebruik van die idees, materiaal en ander intellektuele eiendom van ander persone asof dit jou eie werk is.
Plagiarism is the use of ideas, material and other intellectual property of another's work and to present is as my own.

2 Ek erken dat die pleeg van plagiaat 'n strafbare oortreding is aangesien dit 'n vorm van diefstal is.
I agree that plagiarism is a punishable offence because it constitutes theft.

3 Ek verstaan ook dat direkte vertalings plagiaat is.
I also understand that direct translations are plagiarism.

4 Dienooreenkomstig is alle aanhalings en bydraes vanuit enige bron (ingesluit die internet) volledig verwys (erken). Ek erken dat die woordelikse aanhaal van teks sonder aanhalingstekens (selfs al word die bron volledig erken) plagiaat is.
Accordingly all quotations and contributions from any source whatsoever (including the internet) have been cited fully. I understand that the reproduction of text without quotation marks (even when the source is cited) is plagiarism.

5 Ek verklaar dat die werk in hierdie skryfstuk vervat, behalwe waar anders aangedui, my eie oorspronklike werk is en dat ek dit nie vantevore in die geheel of gedeeltelik ingehandig het vir bepunting in hierdie module/werkstuk of 'n ander module/werkstuk nie.
I declare that the work contained in this assignment, except where otherwise stated, is my original work and that I have not previously (in its entirety or in part) submitted it for grading in this module/assignment or another module/assignment.

12500623 **Studentenommer / *Student number***	**Handtekening / *Signature***
P.C. DU TOIT **Voorletters en van / *Initials and surname***	2018/03 **Datum / *Date***

Abstract

An artificial intelligence approach for biomass devolatilisation in an industrial CFD model with advanced turbulence-chemistry interaction

P. du Toit

Department of Mechanical and Mechatronic Engineering,
University of Stellenbosch,
Private Bag X1, Matieland 7602, South Africa.

Dissertation: PhD (Mech)

March 2018

The ground work to include more detailed chemistry than global approaches in a combustion simulation was completed. A reduced-order model of the Biomass Chemical Percolation Devolatilisation model, ANN-Bio-CPD, was developed and implemented with artificial neural networks in order to achieve ease of execution and computational cost reduction with regard to an industrial computational fluids dynamics application. ANN-Bio-CPD was validated with wire-mesh reactor- and drop-tube furnace experiments from literature. Subsequently, the Eddy Dissipation Concept (EDC) turbulence-chemistry interaction model was implemented and validated with ANN-Bio-CPD in a bagasse-fired boiler simulation. The EDC model constants were adjusted to achieve the correct temperature and intermediate species results in combination with a two-step global reaction mechanism.

Uittreksel

'n Kunsmatige intelligensiebenadering vir biomassa-devolatilisering in 'n industriële CFD-model met gevorderde turbulensie-chemie-interaksie

("An artificial intelligence approach for biomass devolatilisation in an industrial CFD model with advanced turbulence-chemistry interaction")

P. du Toit

Departement Meganiese en Megatroniese Ingenieurswese,
Universiteit van Stellenbosch,
Privaatsak X1, Matieland 7602, Suid Afrika.

Proefskrif: PhD (Meg)

Maart 2018

Die basis om meer gedetailleerde chemie as globale benaderings in 'n verbrandingsimulasie in te sluit, is voltooi. 'n Verminderde-orde model van die Biomassa Chemiese Perkolasie Devolatilisering model, ANN-Bio-CPD, is ontwikkel en met kunsmatige neurale netwerke geïmplementeer om uitvoering te vergemaklik en berekeningskostes te verminder rakende die toepassing van numeriese vloeidinamika op 'n industriële skaal. ANN-Bio-CPD is gevalideer met die eksperimente van draad-maas reaktors- en valbuis-oonde uit die literatuur. Vervolgens is die "Eddy Dissipation Concept"(EDC) turbulensie-chemie interaksie model geïmplementeer en gevalideer met ANN-Bio-CPD in 'n bagasse-gestookte ketelsimulasie. Die EDC-modelkonstantes is aangepas om die korrekte temperatuur en intermediêre spesies resultate te bereik in kombinasie met 'n tweestap globale reaksie meganisme.

Acknowledgements

I would like to express my sincere acknowledgement of the following people:

My supervisors Prof. Meyer and Dr. Laubscher, for guidance and help with this difficult topic.

The staff at Qfinsoft and the combustion department of ANSYS® in the USA for the technical support through-out the work.

My colleagues at John Thompson for comparison of the model results with years of practical experience.

Dedications

To Selina

Contents

List of Figures

List of Tables

Nomenclature

Constants

$C_{D1} =$	0.135
$C_{D2} =$	0.5
$C_{\gamma} =$	2.1377
$C_{\tau} =$	0.4082
g =	$9.81\,\mathrm{m/s^2}$
$R =$	$8314.34\,\mathrm{J/kmol.K}$
$\sigma =$	$5.67 \times 10^{-8}\,\mathrm{W/m^2.K^4}$

Variables

A	Pre-exponential factor or area	$[1/\mathrm{s}, \mathrm{m}^2]$
a	Scalar output of neuron	[ ]
B_m	Spalding mass number	[ ]
b	Artificial neural network bias	[ ]
C_D	Drag coefficient	[ ]
c	Char bridge	[ ]
c_p	Specific heat at constant pressure	$[\mathrm{J/kg.K}]$
D	Diffusion coefficient	$[\mathrm{m^2/s}]$
Da	Damköhler number	[ ]
d	Diameter or vector length	$[\mathrm{m}]$
E	Total energy or activation energy	$[\mathrm{J}, \mathrm{J/kmol}]$
E_c	Difference in activation energy between bridge breaking and char formation	$[\mathrm{J/kmol}]$
e	In-sample error for observation	[ ]
F	Force	$[\mathrm{N}]$
f	Mass fraction	[ ]
g_1	Light gas from side chain path	[ ]

g_2	Light gas from char bridge path	[ ]
H_{reac}	Heat released by surface reaction	[J/kg]
h	Species enthalpy or convective heat transfer coefficient	[J/kg, W/m^{2}K]
h_{fg}	Latent heat	[J/kg]
J	Diffusion flux	[kg/m^2]
k	Thermal conductivity of gas mixture or kinetic energy	[W/mK, m^2/s^2]
k	Kinetic rate or iteration counter	[1/s]
k_c	Mass transfer coefficient	[m/s]
l_t	Energy containing range of turbulence spectrum length scale	[m]
m	Mass	[kg]
m^*	Fine structure mass transfer rate	[1/s]
$\dot{m}$	Mass flow rate	[kg/s]
M_w	Molecular weight	[kmol/kg]
$M_{w,\delta}$	Side chain molecular weight	[kmol/kg]
$M_{w,1}$	Cluster molecular weight	[kmol/kg]
n	Cumulative signal	[ ]
n_K	Kolmogorov velocity scale	[m/s]
Nu	Nusselt number	[ ]
P	Absolute pressure	[Pa]
Pr	Prandtl number	[ ]
p	Total population of bridges	[ ]
p	Scalar input of neuron	[ ]
q	Molar rate of creation/destruction or amount of data-set observations	[kmol/m^{3}s]
R	Amount of inputs to artificial neural network	[ ]
R	Rate of creation or destruction or time scale ratio	[kg/m^{3}s]
Re	Reynolds number	[ ]
S	Amount of neurons in layer	[ ]
S_b	Stoichiometry in mass of oxidant per mass of char	[ ]
Sc	Schmidt number	[ ]
S_j	Source term for species	[kg/m^{3}s]
S_h	Source term for energy	[kg/m^{3}s]
S_m	Source term for mass	[kg/m^{3}s]
T	Temperature	[K]
T_t	Energy containing range of turbulence spectrum time scale	[s]

t	Time or output from artificial neural network	[s]
t_k	Kolmogorov time scale	[ ]
u	Velocity	[m/s]
u'	Energy containing range of turbulence spectrum velocity scale	[ ]
u_K	Kolmogorov velocity scale	[ ]
V	Volume or volatile fraction	[m^3]
v_1	Volatile fraction at previous particle temperature	[ ]
v_2	Volatile fraction at current particle temperature	[ ]
w	Artificial neural network weight	[ ]
X	Symbol for species	[ ]
x	Position	[m]
Y	Species mass fraction	[ ]
Y^*	Fine structure regions species mass fractions	[ ]
Y^o	Surrounding fluid regions species mass fractions	[ ]
$\overline{Y}$	Cell averaged species mass fraction	[ ]
Z	Total number of reactions	[ ]
α	Learning rate	[ ]
β	Temperature exponent	[ ]
δ	Side chains	[ ]
δ_{ij}	Kronecker delta coefficient	[ ]
ϵ	Turbulence energy dissipation rate or emissivity	[m^2/s^3]
η	Kolmogorov length scale or neural network learning rate parameter	[m]
λ	Reacting fraction of fine structure	[ ]
γ	Fine structure length fraction	[ ]
γ^*	Fine structure volume fraction	[ ]
ρ	Density of gas mixture, char to gas kinetic ratio	[kg/m^3]
σ_{ij}	Fluid stress tensor	[N]
$\sigma + 1$	Lattice coordination number	[ ]
τ^*	Fine structure time scale	[s]
τ_K	Kolmogorov time scale	[s]
τ_{mix}	Linear relaxation process time scale or mixing time scale	[s]
τ_{chem}	Chemical time scale	[s]
θ	Radiation temperature	[K]
μ	Molecular viscosity or performance scalar	[Pa.s]

μ_t	Eddy viscosity	[ ]
$\dot{\omega}$	Chemical reaction rate	[kg/m^{3}s]
ν	Kinematic viscosity	[m^2/s]
ν'	Stoichiometric coefficients of the reactants	[ ]
ν''	Stoichiometric coefficients of the products	[ ]
$\pounds$	Original population of labile bridges	[ ]
$\pounds^*$	Reactive bridges	[ ]

Matrices and Vectors

a	Output vector of artificial neural network layer	[ ]
b	Bias vector of artificial neural network layer	[ ]
e	Error vector of artificial neural network	[ ]
g	Gradient	[ ]
H	Hessian matrix	[ ]
I	Identity matrix	[ ]
J	Jacobian matrix	[ ]
p	Input vector of artificial neural network layer	[ ]
W	Weight matrix of artificial neural network layer	[ ]
x	Weights and biases vector of artificial neural network	[ ]

Subscripts

b	Site
b	Bridge or bridge breaking
c	Char
$cross$	Cross-linking
$char$	Char
D	Drag
eff	Effective
f	Forward
$frag$	Tar precursor fragments
g	Gas release
gas	Light gas
i	Components of tensor
in	Input

h	Energy
j	Components of tensor or species designation
k	Components of tensor or species designation
m	Mass
p	Particle
OX	Oxidant
o	Initial
out	Output
r	Reaction designation or reverse
sph	Sphere
s	Surface
t	Turbulent
v	Volatiles
w	Evaporating / boiling material
∞	Continuous phase or final
δ	Side chains
σ	Standard deviation

Abbreviations

AI	Artificial intelligence
ANN	Artificial neural network
BDF	Backward differencing formulation
Bio	Biomass
BYU	Brigham Young University
CHL	Cellulose Hemicellulose Lignin
CPD	Chemical Percolation Devolatilisation Model
DI	Direct integration
DO	Discrete Ordinates
DPM	Discrete Phase Model
DTF	Drop tube furnace
EDC	Eddy Dissipation Concept
EDM	Eddy Dissipation Model
FF	Atmospheric flat-flame burner
FD	Forced draught

FLOX	Flameless Oxidation
GLM	Generalised linear model
GPR	Gaussian process regression
HHV	Higher heating value
HiTAC	High Temperature Air Combustion
ID	Induced draught
IGCC	Integrated Gasification Combined Cycle
ISAT	In-situ-tabulation
JL	Jones and Lindstedt
JT	John Thompson
LES	Large Eddy Simulation
MCR	Maximum continuous rating
MILD	Moderate and Intense Low-oxygen Dilution
MSE	Mean-squared error
NMR	Nuclear magnetic resonance
ODE	Ordinary differential equation
OEM	Original equipment manufacturer
PDF	Probability-density function
PFR	Plug flow reactor
PSR	Perfectly-stirred reactor
RANS	Reynolds-averaged Navier Stokes
RNG	Renormalisation group
ROM	Reduced-order model
RSM	Reynolds Stress Model
SNCR	Selective non-catalytic reduction
SVR	Support vector regression
TGA	Thermogravimetric analysis
TKE	Turbulent kinetic energy
UDF	User-defined function
UFM	Unsteady Flamelet Model
VODE	Variable coefficient ordinary differential equation solver
WD	Westbrook and Dryer
WSR	Well-stirred reactor

Chapter 1

Introduction

The availability of energy is of great concern to human society. As fossil fuels are being depleted, there is a need to find new energy sources. At the same time, climate change has highlighted the impact of reckless consumption on the environment. Energy from biomass combustion plants is CO_2 neutral and sustainable in an agricultural system [Shiehnejadhesar *et al.* (2014)] and is therefore an attractive alternative energy source.

Bio-energy is thus one of the largest sources of renewable energy amongst hydro-, geothermal-, solar- and wind energy [Lins (2016)].

Bagasse is a waste product from the sugar extraction process. Globally, it is common to use the thermochemical conversion of this material to power sugar mills and the peripheral communities. Located at Sezela on the south coast of KwaZulu-Natal, the largest factory in South Africa is owned by Illovo and burns bagasse to generate power. South Africa's newest mill is RCL Komati in Mpumalanga.

Amongst a wide variety of fibrous fuels used worldwide, bagasse forms a large part of the pool and it was therefore chosen for the current project on biomass combustion. RCL Komati was used as a case study.

Combustion involves turbulent fluid flow, chemical reaction, heat transfer and other complicated physical and chemical processes, especially when solid fuels are burnt. Computational fluid dynamics (CFD) lends itself very well to the modelling of combustion [Versteeg and Malalasekera (2007)].

CFD integrates the understandings in combustion fundamentals in the best possible way. It is a powerful and cost-effective tool in the design and optimisation of combustion processes [Zhao *et al.* (2017)].

John Thompson (JT) is a division of ACTOM (Pty) Ltd with its principal focus on boiler and environmental solutions. The complete life cycle of bagasse-fired boilers is a core technology of the company. As an employee, the author conducted the current research at JT.

This study is a continuation of the master's thesis of Du Toit (2015). In

the previous research, a model of a bagasse-fired boiler was developed using the commercial CFD software package ANSYS® Fluent. The simulation included heterogeneous and homogenous combustion with species transport after chemical reaction. Since the focus of that study was on the heat transfer to a tube bank in the combustion zone, the required grid resolution in the bank and turbulence model were investigated in detail. The current body of work focuses on the combustion lower down in the furnace.

More detailed chemistry needs to be included in the combustion simulation developed during the master's project in order to predict air-pollution emissions. Devolatilisation is the starting point of the combustion process and is especially important in a bagasse-fired boiler where flame stability plays a large role. The aforementioned aspects require advanced combustion- and devolatilisation models respectively in order to implement higher order chemistry, which is the topic of this thesis.

Due to the increased computational cost and numerical complexity associated with advanced models, another field of science, namely artificial intelligence (AI), is combined with the central topic of combustion. AI is the study of computations that make it possible to perceive, reason and act, according to Winston (1993). An AI approach is used in this body of work in order to create a reduced-order devolatilisation model.

1.1 Turbulence-chemistry interaction modelling

The topic of this thesis is non-premixed solid fuel combustion. There are three main approaches to model the turbulence-chemistry interaction of non-premixed combustion, namely:

- Composition probability density function (PDF) transport
  A transport equation for the single-point, joint PDF of the species and energy equations can be derived as an alternative to Reynolds-averaging. This PDF (P) represents the fraction of time that the fluid spends at each species, temperature and pressure state. Any single-point thermo-chemical moment can be calculated from P. Detailed chemistry can be handled with this approach.

- Species transport
  Conservation equations describing convection, diffusion and reaction sources for each species is solved. Multiple simultaneous reactions can be modelled. The Eddy Dissipation Concept (EDC) is the only turbulence-chemistry interaction model suitable for kinetics with species transport.

- Non-premixed combustion
  Transport equations for only one or two scalars are solved; the mixture fraction and its variance. The species concentrations are derived from these mixture fraction fields. Interaction of turbulence and chemistry is accounted for with an assumed-shape PDF. The chemistry is solved with chemical equilibrium analysis, the steady- or the unsteady diffusion flamelet model.

The composition PDF transport model is the most accurate approach available and is capable of handling detailed chemistry. However, it is too computationally expensive at an industrial scale [ANSYS (2016)]. The non-premixed combustion model requires the lowest computational effort for detailed chemistry, but it is not valid for laminar flow and not accurate for slow kinetics. The unsteady diffusion flamelet model is more accurate than the steady diffusion flamelet model for slow kinetics. In an industrial boiler, there are laminar regions and cold regions with slow kinetics; therefore, species transport with the EDC was chosen for this project.

1.2 Devolatilisation modelling

Bagasse burns on the grate and in suspension; therefore, the heat transfer to the fuel particles varies considerably. Devolatilisation is sensitive to heating rate and final temperature and is a very important link between the heterogeneous and homogeneous phases of the biomass combustion process. The following approaches can be followed to model biomass devolatilisation:

- Constant rate
  The volatiles are released at a constant rate after the vaporisation temperature is reached.

- Single-rate
  The rate of devolatilisation is first-order dependent on the amount of volatiles remaining in the particle. The kinetic rate is defined by an Arrhenius-type pre-exponential factor and activation energy. The rate of devolatilisation can also be m^{th}-order dependent on the amount of volatiles remaining in the particle and multiple parallel reactions can also be used.

- Chemical Percolation Devolatilisation (CPD) model
  Compared to the empirical rate relationships above, the physical and chemical transformations of the fuel structure is taken into account [Fletcher *et al.* (1990)].

- Cellulose Hemicellulose Lignin (CHL) multi-step model
  The material balance, energy balance and description of physical and chemical processes during devolatilisation are simulated [Biagini *et al.* (2006)].

Of the mentioned models above, the only two approaches that can capture the heating rate effects of devolatilisation are the CPD and CHL models. The complexity, high number of parameters and high computational cost of the CHL model means it is unsuitable for industrial scale CFD simulations; therefore, the CPD model was chosen for this project [Biagini *et al.* (2006)].

1.3 Machine learning in CFD

The Bio-CPD model involves the time integration of several non-linear ordinary differential equations (ODEs). This process requires a variable time step to minimise error and reduce computational effort. Solver libraries, e.g. Sundials, are available and can be added to the ANSYS® Fluent source code while compiling the "User-Defined function" (UDF). However, the range of spatial and temporal scales in an industrial application are so wide that an appropriate solver needs to be chosen and specifically set up or suitable limits need to be imposed.

The use of commercial CFD software is not ideal for this level of customisation. For example, the limited hooks for the Discrete Phase Model (DPM) module of the ANSYS® Fluent version 17.2 source code makes it computationally inefficient for time integration in parallel with the time stepping of the basic DPM conservation equations.

A reduced-order model without time integration is an attractive alternative when considering computational effort- and numerical stability. Additional solver libraries are unnecessary and no restrictions are imposed on time step sizes. Realistic limits can be set on the inputs based on the model validity. Therefore, the outputs are inherently numerically stable.

Recent advances in machine learning makes it a suitable method to determine the relationship between variables in a multi-dimensional feature (input/output) space and it is therefore ideal for reduced-order modelling.

There are five main machine learning techniques available to predict continuous responses via regression, namely:

- Linear regression
  Linear regression is an approach to model the relationship between a scalar-dependent variable Y and one or more explanatory variables X with a linear function. The generalised linear model (GLM) allows the linear model to be related to the response variable via a link function. The magnitude of the variance is a function of the predicted value.

- Support vector regression (SVR) or Gaussian process regression (GPR)
  SVR is a non-parametric technique relying on kernel functions. GPR is a method of interpolation. The interpolated values are modelled by a Gaussian process instead of a piecewise-polynomial spline.

- Ensemble methods
  Ensemble methods use multiple learning algorithms to increase accuracy. For example Bagging assigns equal weights to models and Boosting trains new models that have been added to the ensemble to focus on areas where models under performed.

- Decision trees
  Decision trees map observations to conclusions via a tree-like graph. It is a flowchart-like structure with internal nodes as tests. The leaves can take on continuous values and the branches represent features that lead to these target variables.

- Neural networks
  Neural networks are inspired by biological networks of neurons. Artificial neurons are organised in layers. Different layers perform different transformations on inputs as the signals travel from the input to the output layer. Learning is achieved by passing the information in the reverse direction and adjusting the network to reflect the information.

Of the techniques mentioned above, neural networks are the most accurate and customisable. However, it comes at the price of longer setup and training time. It was found to be the most suited technique to formulate a general method of implementing a submodel for CFD application. Capturing total volatile yield of the Bio-CPD model could be done with a simpler approach; however, more parameters of the Bio-CPD or a combination of different models could be needed in the future. Neural networks are more adaptable for these purposes.

1.4 Problem statement and objectives

The current state-of-the-art turbulence-chemistry interaction for species transport is the Eddy Dissipation Model (EDM) of Magnussen and Hjertager (1976). The EDM predicts the rate of reaction based on the concentration of the reactants and the inverse of the integral time scale. This assumes that the chemistry is fast and the rate of combustion is determined by the rate of intermixing on a molecular scale of the fuel and oxygen eddies. This model is not universally valid over a wide range of flow conditions and therefore needs to be tuned to a specific application

as done by Du Toit (2015). The EDM is also limited to a two-step quasi-global chemical mechanism.

The EDC of Magnussen (1981) is an extended version of the EDM. The model assumes that mixing of the reactants takes place in concentrated, isolated regions that occupy only a small fraction of the fluid volume, namely the fine scale regions. The mass transfer from the surrounding fluid to the fine scales is calculated from the turbulent kinetic energy and dissipation rate of the mean flow. The EDC is therefore a reactor concept valid over a broad range of turbulent flow conditions and can incorporate detailed chemistry.

The primary objective of this study is to implement and validate the EDC on an industrial scale in a bagasse-fired boiler simulation.

The current state-of-the-art solid-fuel devolatilisation model is the single-rate approach. This model is not sensitive to the heating rate and is thus limited to a narrow band of heat transfer conditions for specific kinetic constants. The single-rate model also requires the use of a pseudo volatile molecule and the fractions of tar and light gases cannot be quantified. The CPD model accounts for these effects by taking into account the physical and chemical transformations of the fuel structure [Fletcher *et al.* (1990)]. A very wide range of heating rates and temperatures exists in a bagasse-fired boiler with tar cracking at the high temperature spectrum.

The secondary objective of the study is, therefore, to implement the CPD model with the EDC on an industrial scale. The CPD model has not been used for bagasse combustion on an industrial scale. The combination of these models is a novel contribution to the boiler industry.

Since Bio-CPD of Fletcher *et al.* (2012), the version of the CPD model suitable for biomass, is not available in commercial or open-source CFD software, it will be added to the commercial software package, ANSYS® Fluent, by means of UDFs.

Recent advances in machine learning makes it a suitable method to determine the relationship between variables in a multi-dimensional data space. It was therefore identified as the ideal technique for creating a reduced-order model (ROM) of Bio-CPD. The resulting formulation is easier to implement and computationally more efficient compared with traditional ODE solvers. Artificial neural networks (ANNs) will be used to create the ROM since this technique is more accurate and adaptable than others.

It is hypothesised that the EDC can be implemented and validated on an industrial scale in a bagasse-fired boiler simulation. The hypothesis also states that a reduced-order model of Bio-CPD can be created with ANNs and combined with the EDC in the boiler model.

The following procedure will be applied in this body of work to prove the hypothesis:

- Research previous CFD work involved with turbulence-chemistry interaction, devolatilisation and machine learning
- Research theory of combustion modelling, specifically turbulence-chemistry interaction and devolatilisation; study machine learning theory
- Develop ROM of Bio-CPD by using ANNs
- Validate ROM by modelling laboratory-scale experiments
- Apply ROM in boiler simulation with advanced turbulence-chemistry interaction

1.5 Motivation

Since the completion of the master's project, the developed model has been used extensively at JT. However, there were modelling applications that the current approach is insensitive or inapplicable to, namely:

- Selective non-catalytic reduction (SNCR) of NO_x
- Gas-phase reactions of ash-forming elements that lead to fouling
- Combustion instabilities due to high-moisture bagasse
- Gasification
- Torrefaction

Secondary air systems have been successfully designed using the EDM [Norman *et al.* (2012)]. It is believed that using the EDC will lead to even better designs and reduction of CO, dioxins and other pollutants.

A SNCR system involves the injection of urea in the upper furnace volume of the boiler. The mixing of liquid and combustion gas is crucial. The urea also needs to be introduced at the correct gas temperature. These aspects determine the efficiency of the process and are ideal applications of CFD analysis.

The EDC is required to model the chemistry involved with the formation of NO_x in a bagasse-fired boiler. Devolatilisation is also very important in terms of NO_x formation and the Bio-CPD model can predict the release of fuel-bound nitrogen. The inclusion of tar and light gas fractions of volatiles released by Bio-CPD also improves the accuracy of the chemistry. Achieving the emissions limits without resorting to a costly selective catalytic reduction (SCR) system is the motivation for this research.

JT adapted the fouling model of Kaer (2001) for the DPM in ANSYS® Fluent. Currently, only the evaporation of potassium chloride is considered and the gas-phase reactions of sulphur, chlorine, potassium and sodium are neglected. The EDC is required in order to add these gas-phase reactions to the combustion mechanism. The resulting fouling model can be applied more universally, will be more accurate and will provide a starting point to predict aerosols from fouling fuels.

The more the moisture content of bagasse increases, the more the combustion is influenced by the delay to ignition due to drying. A cyclic explosive phenomenon is seen with more combustion on the grate.

These combustion instabilities can be seen as cyclic flame ignition and extinction and, therefore, require the inclusion of kinetics with the EDC in combination with Bio-CPD in order to model the phenomena properly.

The simulation of these effects will enable the designer to find the correct combination of fuel spreader, grate flow distribution, furnace refractory layout and secondary air system to mitigate combustion instabilities.

Gasification is an efficient and environmentally friendly alternative to the direct combustion of problematic fuels. Due to the lower temperature environment, kinetics and devolatilisation become more important and the EDC in combination with Bio-CPD is required. The prediction of tar is also important as even low tar yields can cause problems in industrial plants by corroding equipment, causing damage to gas turbines and gas engines, lowering catalyst efficiency when present in syngas and condensing in gas transfer lines [Lewis (2011)] [Lewis (2014)].

During the process of torrefaction biomass is upgraded in energy density. Therefore, if the fraction of char in the torrefied material can be maximised with the least amount of volatiles consumed, the energy density can be optimised.

The Bio-CPD model is required to predict the volatile-char ratio as well as the heating rate effects. A CFD model of the kiln can be used to potentially improve the torrefaction process.

Chapter 2

Literature study

Since this project involves the unique combination of two submodels and a new submodel implementation method, the literature review has been structured in three parts, namely turbulence-chemistry interaction modelling, devolatilisation modelling and machine learning in CFD. The models discussed are mainly the EDC and Bio-CPD. Minimal literature on the combination of these two models was found and, therefore, mainly the separate applications of these models will be discussed.

Due to the difficulties involved and the computational demand of implementing Bio-CPD in the commercial CFD software ANSYS® Fluent via UDF, a final section is devoted to reduced-order modelling by means of machine learning.

Each section begins by explaining the main concepts without the underlying mathematical theory. Applications by research groups are discussed thereafter.

2.1 Turbulence-chemistry interaction modelling

The EDC is based on the turbulent energy cascade and was developed by Magnussen (1981). A key concept of the model is that the mixing of the reactants takes place in concentrated, isolated regions that occupy only a small fraction of the fluid volume, namely the fine scale regions. The mass transfer from the surrounding fluid to the fine scales is calculated from the turbulent kinetic energy and dissipation rate of the mean flow. The fine scales are locally treated as isobaric, adiabatic, perfectly-stirred reactors (PSRs).

After many inquiries about the considerations behind the EDC, Ertesvag and Magnussen (1999) published a paper to explain the turbulence energy cascade model. The connection between the larger eddies and fine structures is addressed in this publication.

Different interpretations and incorrect application of the EDC led to another publication by Magnussen (2005). In this paper, the most recent formulation is presented.

Since the emphasis of this project is the industrial application of the EDC turbulence-chemistry interaction, the author focused on the following areas during the review of the work done by the different research groups:

- Scale of the geometry,
- Application,
- Fuel,
- Meshing,
- Turbulence model,
- Chemical mechanism,
- Heterogeneous combustion and submodels, if applicable,
- Level of validation

Meldgaard (2009) simulated a typical industrial boiler furnace burning wood at 50 % moisture. The aim of the study was to find methods of reducing CO emissions. A hexahedral mesh of 1.4 million cells was used for a domain of 5 m deep, 5 m wide and 18 m high. The realizable k-ϵ turbulence model was used with the EDC and detailed chemical kinetics, namely the GRI-1.2 mechanism. It consists of 177 reactions. A standalone bed model was used with the products of evaporation, devolatilisation and char combustion evenly distributed over the area of the grate. Interaction between the fuel bed and furnace was not considered; therefore, only the primary air delivered the heat for moisture evaporation and devolatilisation. No validation was done. The results were only discussed in comparison to typical patterns expected in biomass boilers. It compared well qualitatively, apart from the area close to the bed, as expected, due to bed model's isolation from the freeboard. A solution procedure was followed, but although average temperature values at different elevations converged, CO did not converge. Different numerical strategies were followed in order to improve convergence. In the end, the flow field was held constant and energy and species solved until convergence. Due to the extra run-time required, the flow field was not activated again, although it is the recommended procedure.

Chungen *et al.* (2010) modelled a 150 kW swirl-stabilised dual-feed burner flow reactor burning wheat straw with coal. The purpose of the project was to find a

reliable modelling methodology for pulverised biomass and coal co-firing. A quadrilateral mesh of 60 000 cells was used. Results using the standard- and realizable k-ϵ turbulence models were compared. The Jones and Lindstedt (JL) four-step quasi-global chemical mechanism with the EDC was compared to the Westbrook and Dryer (WD) two-step scheme combined with the finite-rate EDM hybrid approach. The standard mass and energy transfer models available for DPM was compared to a thermally thick particle model. A single kinetic rate devolatilisation model was used. The predicted O_2, CO_2, H_2O and CO was compared to experimental data. The EDC with JL four-step predicted the flame volume more accurately.

Zahirovic *et al.* (2006) simulated the Sandia CH_4 D flame and Sandia $CO/H_2/N_2$ B flame. The burner consists of a main round jet and a concentric pilot. It was placed in a wind tunnel for the experiments. Comprehensive data of species and temperatures are available for these experiments. The aim of the study was to ultimately develop a model for improved combustion prediction in biomass furnaces. An axi-symmetric 2D mesh of 8 500 hexahedral cells was used for Reynolds-averaged Navier Stokes (RANS) simulations and 194 000 hexahedral cells for Large Eddy Simulation (LES) simulations. The realizable k-ϵ turbulence model outperformed the standard k-ϵ model. There was also no significant improvement using the Reynolds Stress (RSM) turbulence model. The ARM 9 and ARM 19 reduced mechanisms, Kilpinen 92 detailed mechanism and the global mechanism of Brink (1998) were used. The LES simulations indicated that the ARM 19 performs better than ARM 9. The Kilpinen 92 produced lower temperatures closer to the experimental data. The global mechanism performed well from a qualitative perspective.

Schmidt *et al.* (2013) modelled a 440 kW thermal biomass grate furnace burning fibre board in order to predict NO_x emissions. The mesh size was 275 000 cells. The realizable k-ϵ turbulence model was used with the EDM finite-rate hybrid turbulence-chemistry interaction. The global three-step mechanism for CH_4, CO, CO_2, H_2 and H_2O of Brink was utilised. A standalone empirical-bed model accounted for the solid biomass combustion on the grate. The NO_x formation was predicted in a post-processor mode with the EDC, and the Kilpinen 92 detailed mechanism as a coupled simulation of flow and chemistry was too time-consuming. The results of NO_x emissions compared well quantitatively and qualitatively with the measurements in the furnace.

Scharler *et al.* (2011) and Scharler *et al.* (2004) discussed various other case studies, namely an overfeed pellet boiler, a wood log fired boiler, wood log fired stoves and an underfeed multi-fuel boiler. These plants are all under 100 kW thermal. A 7.2 MW thermal industrial-scale biomass grate furnace firing wood was also modelled. The modelling methodology discussed above was used in all cases. Ideal reactor calculations were performed in order to check the results of the Kilpinen 92

mechanism against more comprehensive reaction mechanisms. These calculations consisted of plug flow reactor (PFR) and PSR approaches and no major deviations were found. This is interesting and confirms the validity of the most popular implementation of the EDC involving the use of a PFR integrated over the time scale of the reaction. Magnussen (2005) recommended a PSR integrated to steady state. This, however, adds additional complexity due to the highly non-linear algebraic equations that need to be solved. The predicted NO_x emissions at the boiler outlet of the industrial-scale plant compared well with measurements. There were larger deviations in other areas of the boiler simulation due to the limitations of the EDM and the empirical fixed-bed model used for the basic combustion simulation.

Shiehnejadhesar *et al.* (2014) simulated the Sandia A, B and D flame. These flames cover laminar, transition and turbulent combustion conditions, respectively. The purpose of the study was to develop and calibrate a hybrid gas-phase combustion model suitable for low and high turbulent combustion conditions as found in industrial biomass grate fired boilers. A 2D axisymmetric grid with 4 000 cells was used. The standard k-ϵ turbulence model with the $C_{\epsilon 1}$ constant changed from 1.44 to 1.58, to compensate for the round-jet anomaly, was utilised. The reduced chemical mechanism DRM-22 used in the simulations performed identically to the detailed GRI 2.11. The hybrid model is a combination of the EDC and finite-rate chemistry weighted with the turbulent Reynolds number of the flow. It displayed great potential for application in all ranges of flow conditions when compared to the experimental data.

Mehrabian *et al.* (2014) modelled the combustion of spruce pellets in a laboratory-scale fixed-bed reactor in order to take bed shrinkage and variation of porosity into account. The DRM-22, GRI 2.11 and Kilpinen 97 mechanisms were used. The conditions in the reactor are laminar and therefore only finite rate chemistry was utilised. The DRM-22 mechanism performed the same as the GRI 2.11. The Kilpinen 97 also compared well to the GRI 2.11 for engineering application.

Magnussen (1981) showed very good correlation between calculated and experimental data of temperature and NO for a hydrogen diffusion flame, soot concentrations for turbulent diffusion flames and oxygen concentrations in a premixed flame in his original EDC paper. He also presented results of a bluff-body stabilised flame simulation using fast- and detailed chemistry. Excellent correlation was achieved, apart from the fast chemistry simulation which over-predicted peak temperature considerably. The RSM turbulence model was used [Magnussen (2005)].

Weydahl *et al.* (2002) modelled a well-defined laboratory flame investigated by Lapp *et al.* (1983). A mixture of CO, H_2, N_2 and CH_4 was used as fuel. The purpose of the project was to investigate the NO_x formation from fuel-bound nitrogen in turbulent non-premixed flames. Two 2D axisymmetric meshes of 1 400 and 1 900 cells were constructed. The standard k-ϵ turbulence model with modified

constants was utilised to give the best representation of the reacting turbulent round-jet flow. The model contained the detailed chemical mechanism, GRI 2.11. An interesting difference between this model and those of other authors discussed is the use of a PSR integrated to steady state as intended by Magnussen in his original EDC formulation. The focus of the validation was on NO and NO_x species. It was shown that the model captured the overall effects of NO_x formation from fuel-bound nitrogen. The application of the model was illustrated by simulating a wood stove. The size of the mesh was 34 425 cells. The combustion of CH_4 and CO was modelled with a single-step mechanism according to the fast chemistry assumption of the EDC. Production of thermal NO_x is insignificant below 1 700 K; therefore, detailed chemistry is required to study the fuel-bound NO_x formation in a wood stove since the peak temperature predicted was 1 300 K.

Lysenko *et al.* (2014) simulated the Sandia D flame with a RANS and LES approach. The long term goal of the research is to develop a LES model for high turbulent Reynolds number flows to be adapted further for combustion modelling. Two grids consisting of 4 400 and 8 800 cells were used for the RANS simulations. The standard k-ϵ turbulence model was used with the detailed GRI 3.0 mechanism. The chemistry was integrated to steady state with the PSR concept. The main reasons for the discrepancies between the RANS results and experimental data was believed to be due to the round-jet anomaly of the standard k-ϵ turbulence model.

Myhrvold *et al.* (2003) modelled a premixed flame in a turbulent low-Reynolds-number Couette flow. A low-Reynolds-number version of the EDC was proposed for this turbulent-reacting-near-wall flow. The methane flame is V-shaped and held in position by a flame holder, where one branch interacts with a cold wall. A 2D mesh of 1764 cells was used. A single-step chemical mechanism with the low-Reynolds number turbulence model of Jones and Launder was used. The low-Reynolds-number EDC is based on weighting between the EDC and finite-rate chemistry by calculating the turbulent Reynolds number of the flow. The results were compared to direct numerical simulation (DNS) and showed that the proposed model might be a way to extend the EDC to reacting flows near walls.

Magel *et al.* (1995) simulated a 350 kW thermal pulverised coal flame and a coal-fired utility boiler. The purpose of the study was to develop a model in order to simulate air staging and the near-burner field of swirl flames. This model can be used to modify boiler plants to achieve lower emissions and more efficient combustion. The burner mesh contained 12 100 cells and boiler mesh consisted of 186 000 cells. The standard k-ϵ turbulence model was used. The coal particles were handled with an Eulerian approach, which is uncommon. A two-step global reaction was used as proposed by Zimont and Trushin and Howard. The volatile kinetic rate was increased by an order of magnitude. A PSR approach was followed

by solving the steady state algebraic set of equations for the fine structure species and temperature of the EDC. No measurements of temperature was available for the burner simulations, but species and velocity data correlated well with the EDC results. The same correlation could not be achieved using the EDM, even with tuned constants. CO measurements at the lowest burner level of the utility boiler corresponded well to the EDC results. The EDM under-predicted the CO.

Miltner *et al.* (2006) modelled a 2 MW thermal combustion chamber for a solid stem-shaped biofuel in the form of a bale. The objective of the study was to minimise gaseous emissions such as volatile organic compounds (VOC), CO and NO_x. The combustion efficiency of the bale also had to be maximised. The SST-k-ω turbulence model by Menter was used. Global chemistry mechanisms were used with the EDC. The volatile, CO, H_2 and NO_x precursors were included with kinetic parameters from Brink *et al.* (2001), Hill and Smoot (2000) and Westbrook and Dryer (1981). The heterogeneous combustion submodels were included as sources in a porous zone. No validation data was included in the publication.

Jordan and Harasek (2011) simulated a 1 MW thermal boiler burning wood-chips and grain. The purpose of the study was to develop a small-scale combustion unit based on grate firing with a thermal output in the range 300 to 350 kW. The design had to overcome the emission and fouling problems associated with burning wood, straw and grains. The mesh consisted of 1 million hexahedral cells. The EDC turbulence-chemistry interaction with the SST-k-ω turbulence model by Menter was used. A chemical mechanism by Saxena consisting of 30 reactions was utilised. An empirical-bed model was linked to the CFD model with source terms in a porous zone. The validation consisted of average species measurements at the outlet of the boiler, and infrared thermal images of boiler surfaces and the fuel bed which corresponded well with the model predictions.

Andersen (2009) modelled a 50 kW thermal reactor burning natural gas constructed to simulate the conditions in the freeboard of a grate-fired boiler. The aim of the PhD was to provide validation data for CFD models relevant for grate-firing combustion conditions. NO_x emissions were also investigated and the long-term scope of the study is to develop a CFD-based method capable of predicting NO_x chemistry in the freeboard section of a grate-fired boiler. The WD two-step mechanism, JL four-step and the skeletal mechanism of Yang and Pope (SKEL) were utilised with the standard k-ϵ turbulence model. A comprehensive validation campaign indicated that only when the EDC calculations were superimposed on the flow-field from the EDM modelling, did the more advanced model provide satisfactory results. Post processing of NO_x was done within the EDC framework.

Farokhi and Birouk (2016*a*) modelled Flame A of Barlow and Frank (1998) at low turbulence and Sandia Flame B with high turbulence. The motivation of the study was to investigate the influence of EDC model constants on its predictions.

The final goal was to model a grate-fired biomass boiler. The flame choices are representative of the volume above the fuel bed and in the vicinity of the secondary air jets. Methane fuel was used in both cases. The flame geometries are similar and, therefore, the same meshing strategy as Zahirovic *et al.* (2006) was utilised. The renormalisation group (RNG) k-ϵ turbulence model was applied with the DRM-22 chemical mechanism a reduced form of GRI 1.2. Comprehensive data of species and temperatures are available for these experiments and were compared to the predictions of the EDC with different model constants.

The influence of molecular diffusion was found important since Flame A could not be simulated without considering it. Flame A could also not be stabilised with the default value of C_τ. It was found that when the turbulent Reynolds number (Re_t) is below the limit ($Re_{t,min} = 64$ with the default value of C_γ), using a higher value of C_τ resulted in under-predicting temperature and CO. A lower value of C_τ improved the predictions. Under these conditions, the size of the fine structure is fixed on its maxima and the reaction rate is only dependent on C_τ. When Re_t is above $Re_{t,min}$, the influence of both model constants becomes important and a lower value of C_γ leads to smaller reactions zones. Under these conditions, a higher value of C_τ results in higher peak temperatures in contrast to the effect when Re_t is smaller than $Re_{t,min}$. The trends of temperature and species for all model constant combinations were consistent.

In the simulations of Flame B, the effect of C_γ on the predictions of temperature and species is more pronounced than C_τ. The same temperature peaks were seen with different values of C_τ and constant C_γ; however, higher values of C_τ resulted in lower temperature profiles before and after the peaks. This indicates that the mixing time scale controls the reactions at the peaks due to the high temperature and fast chemistry. However, away from the peaks, the competition between chemical and mixing time scales becomes important and hence the influence of C_τ on the predictions. As for the species, when using a lower value of C_γ and hence a smaller value of $Re_{t,min}$, both model constants exert an influence on predictions especially for slow chemistry species (CO). At a higher $Re_{t,min}$ the predictions showed a dependence on only C_γ. The ratio of turbulent time scale over the characteristic mixing time scale was found almost unchanged under high turbulent flow conditions, although mathematically it is a function of the size of the fine structures and model constants.

It was concluded that the EDC can be applied to low turbulent flow regions by modifying the model constants and basing the choice of constants on Re_t. The accuracy of the model could also be improved for highly turbulent conditions by changing the constants. When Re_t is larger than $Re_{t,min}$, both model constants and the characteristics of the turbulence field have a complex dependency on the reaction rate. However, when Re_t is lower than $Re_{t,min}$, only C_τ affects the pre-

dictions.

Farokhi and Birouk (2016*b*) modelled the 8 to 11 kW lab-scale biomass furnace experiments of Klason and Bai (2006). The cylindrical combustor has a diameter of 0.2 m and height of 1.7 m. The aim of the study was to investigate the capability of the modified EDC for simulating biomass combustion. The fuel utilised in the experiments was wood pellets. A 3D non-uniform mesh of 690 000 cells was used. The RNG turbulence model and a two-step global chemical mechanism with CO as the intermediate species was utilised. An empirical-bed model was applied for the heterogeneous processes. The model results were compared to measurements of temperature, CO, CO_2 and O_2 along the centre line of the furnace.

Since it was found that the ratio of turbulent time scale over the characteristic mixing time scale is independent of the size of the fine structures for high turbulent flow regions, where R_t is higher than $R_{t,min}$, it was decided to increase $R_{t,min}$ from 64 to 100 by increasing C_γ from 2.1377 to 2.37. The corresponding value of $C_\tau = 5.62$ was calculated based on the fact that the term $(1-\gamma^3)^{-1})$ is close to unity in most of the domain where the turbulence is high. Additionally, the term T_t/τ_{mix} is unity because the reaction rate is controlled by turbulent mixing, thus setting the mixing time scale equal to the turbulent time scale as recommended by Rehm *et al.* (2008) for case no. 3. Another case was run with $C_\gamma = 1.75$ in order to decrease $R_{t,min}$ from 64 to 30, corresponding to the low turbulent flow regions close to the walls. The value of C_τ was kept at 5.62, effectively increasing the value of the mixing time scale beyond the turbulent time scale ($1.8T_t$) in the highly turbulent regions where $(1-\gamma^3)^{-1})$ is close to unity for case no. 2. This value is still lower than the largest value found to be used in literature, the Taylor time scale applied by Kjäldman *et al.* (1999) of $4T_t$ for modelling natural gas in a sudden-expansion reactor geometry. Case no. 1 was run with the default model constants.

It was found that the modified constants had a slight impact on the velocity field. The flow in most regions of the combustor is highly turbulent and thus the findings with Flame B, that the influence of C_τ on the results of temperature and species is weaker than C_γ, was confirmed. The effect of the constants was mostly visible in the vicinity of the bed and the predictions almost independent of the coefficients downstream. Case no. 2 produced the best correlation of temperature with measurements, and case no. 3 for CO. It was confirmed that the modified EDC can lead to more accurate predictions of temperature and species, especially slow-forming pollutants such as CO in industrial biomass furnaces, due to the wide range of flow conditions in these plants. Prior knowledge of the flow field, i.e. turbulent Reynolds number and Kolmogorov time scale, is required. From these findings, a reactor model based on combustion in the surrounding fluid and fine structures is recommended for industrial biomass furnace models, as suggested by Rehm *et al.* (2008), Kjäldman *et al.* (1999) and Magnussen (2005).

Limited studies using the EDC for biomass combustion on an industrial scale were found. Most of these projects utilised the model as a post processor due to the high computational cost compared to the EDM. The application of Meldgaard (2009) is the closest to the current body of work; however, the flow field was frozen due to convergence issues and validation lacked. The applicability of the EDC for the current research could thus not be confirmed by an example from literature.

However, the suitability of the model for a laboratory scale- and pilot plant application were confirmed. The accuracy achieved at a low computational cost compared to the composition PDF model is also encouraging. Limitations of the current implementation of the EDC in ANSYS® Fluent were also highlighted, namely inaccuracies for low Reynolds flow and prediction of slow-forming species.

The prediction of the implementation of the EDC in this body of work can be improved by modifying the model constants based on prior knowledge of the flow field, i.e. turbulent Reynolds number and Kolmogorov time scale. A hybrid EDC model that switches to laminar kinetics improves the low Reynolds number flow deficiency. A modification to the EDC to include reactions in the surrounding fluid is recommended for slow-forming species.

2.2 Devolatilisation modelling

The CPD model was originally developed for coal by modelling it as aromatic clusters connected by labile bridges. When heated, the bridges become activated and the reactions proceed along two competing pathways. The one path forms side chains and subsequent light gas, while the other path forms light gas and stable char bridges. These competing reaction rates are a function of kinetic parameters. The rate at which bridges rupture is modelled and percolation statistics for Bethe lattices predict the cleaved bridges and detached clusters.

Bio-CPD considers biomass as a mass-weighted average of cellulose, hemicellulose and lignin. The base structural unit of lignin is coniferyl, coumaryl and sinapyl alcohols. The fixed anomeric carbon and attached hydrogen is used as the base cluster for cellulose and hemicellulose.

Since the emphasis of this study is the application of the CPD model in biomass combustion on an industrial scale, the following areas are focused on during the review of the work done by different research groups:

- Scale of geometry,
- Application,
- Material,
- Mesh and amount of particles,

- Combustion models, if applicable,
- Level of validation

Sheng and Azevedo (2002) extended the CPD model originally developed for coal to the three main components of biomass, namely cellulose, hemicellulose and lignin. The same reaction scheme applied for coal was used. Bridge breaking, bridge rearrangement, side-chain cracking and gas release, tar distillation and cross-linking were considered. The secondary reaction of tar was included as it was found important at high temperature. Structural and kinetic parameters of the CPD model were changed according to the three main components of biomass.

The model is to be applied in the simulation of biomass combustion systems for power generation. During this stage of the development, only high heating rate devolatilisation experiments were modelled.

The results of lignin devolatilisation at 1 000 K/s showed reasonable agreement of char, tar and light gas fractions with the experimental data. Bagasse was modelled as cellulose and lignin, and silver birch as cellulose, hemicellulose and lignin. The model under-predicted the yields of both materials for the lower temperatures. Heating rates of 1 000 K/s and 1 K/s in wire-mesh reactors were used. However, the cooling stage was not simulated, which may account for the difference. The model also predicted higher yields at the lower heating rate compared to the higher heating rate contrast to the experiments, which could also be attributed to the omission of cooling. At high temperature, the tar yield was predicted at an intermediate level. The char was over-predicted at the high heating rates. The model was also compared to sweet gum hardwood devolatilisation at 1 000 K/s. An empirical correlation based on the proximate analysis of the material was used to determine the fractions of cellulose, hemicellulose and lignin. The results of char, tar and light gas fractions as a function of peak temperature agreed well with the experimental measurements.

Da Silva (2008) used the kinetic and structural parameters of Sheng and Azevedo (2002) in order to model devolatilisation experiments from literature. Experiments with sawdust in a drop tube furnace (DTF) at 1 350 K was modelled. The volatile release was predicted too early and final volatile yield was under-predicted. Predictions of lower heating rate experiments were more accurate.

Due to the under-prediction of the high temperature, high heating-rate conditions, Bio-CPD was not used in the CFD simulation of the pulverised fuel fired furnace.

Houkema *et al.* (2012) used the CPD model with the EDC in order to simulate pulverised biomass and coal combustion. However, it is not clear if Bio-CPD was used for the biomass component. Oxy-fuel combustion simulations of a 3 m long reactor with a burner firing a coal and shea meal blend was run. Measurements

of gas temperature, O_2 and CO gas species compared well to the results of the simulations.

Rabacal *et al.* (2014) used the tar cracking model of Vizzini *et al.* (2008) as a post-processing step following the work of Lewis and Fletcher (2013). As an addition to the correlation method of Sheng and Azevedo (2002), a triangulation method was employed to determine the biomass component fractions of cellulose, hemicellulose and lignin.

The model is intended for the use of CFD modellers, biomass combustion and gasification plant designers.

Two experimental studies of fast pyrolysis from literature were modelled. These tests were conducted in a DTF. The materials used were sawdust and Beech wood. Reactor temperatures varied from 973 to 1 673 K. For both the correlation- and triangulation method of determining the biomass composition, the total volatile yield over time was under-predicted, regardless of reactor temperature. The results from using both these methods were also similar. In contrast to the predictions, a decreasing char yield with temperature trend was seen in the experiments. Bio-CPD predictions present a change in slope of total volatile yield versus time. This corresponds to the release of hemicellulose and is typically seen in Thermogravimetric analysis (TGA) experiments. A sensitivity analysis revealed that total volatile yield predictions did not vary significantly within the whole spectra of the composition. For a variation of 20 % in the composition of the biomass, the total volatile yield does not vary more than 10 %. However, gas and tar predictions are sensitive to the composition. Cellulose governs the production of light gas, whereas hemicellulose and lignin govern the production of char and tar.

Biagini *et al.* (2006) adapted the CPD model to biomass in the same way as Sheng and Azevedo (2002). However, the formulation of the mass balances was substantially revised. A population balance was used for the liquid n-mers. The tar yields in the vapour phase and the liquid metaplast remaining in the particle were differentiated. Tar cracking in the gas phase was considered in this way. As an estimate of the vapour and liquid present, a simple form of Raoult's law was used as vapour pressure correlation.

Due to the computational efficiency of the Bio-CPD model, it is to be incorporated in comprehensive 3D combustion codes according to Biagini *et al.* (2006). Numerical experiments were simulated.

Data of numerical experiments were generated with the CHL model. Temporal profiles of gas, tar and char were used. Cellulose, hemicellulose and lignin was modelled at a heating rate of 14 000 K/s. The model parameters were optimised as a non-linear least-squares problem subject to bounds on the variables. Predictions for cellulose compared well to the CHL data.

Vizzini *et al.* (2008) continued the work of Biagini *et al.* (2006). A procedure

based on the hypothesis of speciation for char, metaplast and tar released was used. In this way, the light gas elemental speciation is achieved by closing of the material balance. A Chemkin routine for light gas equilibrium calculations was also added. The yields of main gas species was predicted through these modifications.

Devolatilisation experiments from literature of Avicel cellulose and Red Maple sawdust at a heating rate of 14 000 K/s were modelled. The results show fine agreement with the measurements. The yields of gas, char and tar of cellulose agreed better with the experiments. The predictions also suggest that high temperature kinetic mechanisms become very important in pyrolysis, because it can slow species evolution toward equilibrium.

Fletcher *et al.* (2012) followed a similar approach to Sheng and Azevedo (2002) to adapt the CPD model to Biomass. The structural parameters were set with Nuclear magnetic resonance (NMR) measurements and known structures. Initial kinetic parameters were taken from the work of previous researchers e.g. Sheng and Azevedo (2002). Three parameters needed to be fitted to volatile yield data, namely cluster cross linking activation energy (E_{cross}), char to gas kinetic ratio (ρ) and initial fraction of char bridges (c_o). An optimisation program was used to fine-tune these parameters. Secondary tar reactions were not modelled.

The model was formulated for inclusion in ANSYS® Fluent and PCGC-3 CFD packages. The research will be combined with models of black liquor char gasification and mineral decomposition in a form for engineering simulation of recovery boilers. Heated grid data from literature of Lignin devolatilisation at a heating rate of 1 000 K/s and cooling rate of 200 K/s with no hold time was modelled. The results of tar and light gas yields compared well to the measurements. Cellulose devolatilisation tests from literature in a laminar-flow reactor were also modelled. Heating rates varied from 1 400 to 3 200 K/s. A hold time of 0.3 s and cooling ramp of 600 K/s were used. The model was fine-tuned to this data. Experiments of the hemicellulose components, xylan and glucomannan, were modelled. These TGA tests were performed at 20 K/s. Both components showed a change in total volatiles released just before 600 K. The model agreed remarkably well with the data.

Lewis (2011) continued the work of Fletcher *et al.* (2012). The tar-cracking model of Vizzini *et al.* (2008) was added for the secondary tar reaction into light gas. The empirical relationships of Sheng and Azevedo (2002) were used in order to calculate the fractions of cellulose, hemicellulose and lignin from the proximate analysis for some of the biomass samples.

The objective of the study was to model biomass pyrolysis more accurately in order to design more efficient gasifiers for power generation by means of Integrated Gasification Combined Cycle (IGCC).

Atmospheric flat-flame burner (FFB) devolatilisation experiments of softwood

sawdust were conducted and modelled. Very high heating rates from 250 000 to 720 000 K/s were used. The predictions of char yields were good across the range of temperatures. The predicted pyrolysis yields were within 8 % of the measured values. The predictions of tar and light gas yields were accurate at the higher temperature and heating-rate conditions. At the lower temperature and heating-rate conditions, the predictions had an average discrepancy of 18.3 %. It was subsequently improved to 5.3 % by using tar-cracking kinetics specific to sawdust instead of the kinetics for cellulose, hemicellulose and lignin. Without tar-cracking, the predicted tar yield matched the measured gas yield, clearly illustrating the need for a tar-cracking model above 773 K.

Devolatilisation experiments from literature were also modelled. Fluidised bed devolatilisation tests of Maple, Poplar-Aspen and Aspen bark at 680 K/s were modelled. The model over-predicted char values below 773 K, but agreed within 14 % above this temperature. It also under-predicted the tar yield below 773 K. Sweet Gum sawdust pyrolysis tests from an electrical screen heater at 1 000 K/s, a cooling rate of 200 K/s and no hold time were modelled. Model predictions were within 6.7 % of the experimental char yields, except at 800 K where predicted tar yields were almost twice the measurements. This version of Bio-CPD with kinetic parameters regressed from experiments at higher heating rates, thus over predicted tar yields at lower heating rates. Pine sawdust devolatilisation experiments in a DTF, at conditions where minimal tar cracking occurred, were also modelled. The heating rates varied from 400 to 3 000 K/s. Despite the short residence time and low temperatures to suppress tar cracking, a slight decreasing tar yields and increasing gas yields were seen from 773 to 873 K. Although the predicted char yield at 723 K was 12 % high, the discrepancy decreased as pyrolysis temperature increased. This discrepancy can be explained by the material losses in the collection system, reported to be 10 % on average. Another explanation is that there is an effect of high heating rate on biomass volatile yields that is not fully captured by the CPD model.

Beech sawdust pyrolysis experiments from literature were also modelled by Lewis and Fletcher (2013). These tests were conducted in a TGA at a low heating rate of 17 K/s to final temperatures ranging from 573 to 708 K. Tar cracking was not considered. The results of char yields were within 9 % of measurements at 637 K and within 3.9 % at 708 K. However, at the lower temperatures of 573 and 593 K, the Bio-CPD model over-predicted the final char yield by an average of 24 %. Most industrial processes involves pyrolysis at high temperatures except torrefaction, for which the kinetic parameter will have to be adjusted.

Lewis (2014) conducted and modelled FFB devolatilisation experiments of hardwood sawdust (Poplar), straw and switchgrass. The Bio-CPD model with tar cracking predicted full pyrolysis after the first collection point, as measured.

The model correctly predicted yields comprising light gas with no tar, but the char was over-predicted by 8.9, 4.9 and 8 % for Poplar sawdust, straw and switchgrass, respectively. The predicted tar yield was close to the measured gas yield without the tar cracking model, which demonstrates the importance of tar cracking above 773 K.

Prince (2014) used the Bio-CPD model with the structural and kinetic parameters of previous research done at Brigham Young University (BYU), Utah, United States. The CPD model was adapted for MATLAB® from FORTRAN 77. A new flash routine was written following the Rachford-Rice procedure. The predictor-corrector scheme used to solve the system of ODEs was replaced by a matrix exponential method that decreased the computational time marginally and permitted larger time steps. A conservation of mass error for some biomass components at long residence times resulted in unstable model calculations. Since it was caused by negative mass fractions as input to the flash routine, it could be corrected by scaling positive mass fractions in order to conserve total mass. The model was also integrated into an object-oriented class that allowed any number of CPD objects to be instantiated and manipulated concurrently. It allowed mass release of multiple components and leaf locations to run side-by-side. 1D conduction through the leaf was determined from the temperature of the internal nodes at each new time step that depend on the mass release from the previous time step.

The objective of the study was to increase the understanding of fire spread in live sparse shrubs. Ultimately, a fire-spread model could provide operational support to fire fighters.

FFB devolatilisation and water release experiments of Manzanita shrubs were conducted and modelled. The gas temperature was approximately 1 273 K. The Bio-CPD model in combination with a water-release model compared well to measurements of mass loss. The temperatures of mass release were higher than often reported for biomass; however, the modelled and measured values agreed well and the local temperatures of mass release increased with the increasing heating rate, as expected.

The applicability of the Bio-CPD model for the current research on biomass combustion could not be confirmed by an example of an industrial biomass combustion CFD application from literature. Various authors modified the CPD model for biomass and achieved good results for laboratory scale devolatilisation experiments at different heating rates and with different fuels, although only Sheng and Azevedo (2002) modelled bagasse.

An under-prediction in volatile yield at high heating rates suggests that an effect is not fully captured by the CPD model. As developers of the original CPD model, the most comprehensive development and validation of Bio-CPD was

conducted at BYU. Therefore, the latest version of their CPD model with settings from Lewis and Fletcher (2013) was found appropriate for the current body of work.

2.3 Machine learning in CFD

ANNs contains connections between neurons arranged in layers. As an example, a system of three layers is considered. The first layer has input neurons that sends data to the hidden layer and from there it is passed to the output layer. An ANN is defined by the connection pattern between layers, the weights of the connections updated during learning and an activation function to convert the neuron's weighted input to its output activation.

Since the emphasis of this study is the application of machine learning on reduced-order modelling of CFD submodels on an industrial scale, the following areas are focused on during the review of the work done by different research groups:

- Scale of geometry,
- Application,
- Material if applicable,
- Mesh and amount of particles if applicable,
- Combustion models if applicable,
- Level of validation

Muller *et al.* (1999) used biologically inspired modelling and optimisation techniques such as ANN and evolution strategies. The applications are drag minimisation of cylinders, boundary layer modelling, enhanced jet mixing and turbine blade film cooling.

A reduced-order model of near wall structures was successfully formulated with linear and non-linear neural networks. The application is feedback control algorithms. The non-linear ANN out performed the linear ANN when comparing the predictions to the analytical solution of the stochastically forced Burger's equation. Turbulent channel flow simulation results were also compared to the two ANNs. Again, the non-linear ANN outperformed the linear model. A snapshot of the stream-wise and span-wise averaged u^+ profile compared well to the model reconstructions.

Yarlanki *et al.* (2012) trained an ANN to find the error between the results of a CFD model and measurements for a given set of turbulence model constants.

The application was heat transfer in data centres. Temperature measurements were used to determine the modelling errors. The constants of the k-ϵ turbulence model were optimised and resulted in lowering the RMS error by 25 % and the absolute average error by 35 %.

Guillas *et al.* (2014) constructed a fast statistical surrogate of a CFD model using Bayesian networks. The reduced-order model was used to quantify the uncertainty of the turbulent kinetic energy (TKE) outputs due to uncertainties of the CFD parametrisation, the numerical code and measurements. The standard k-ϵ turbulence model constants were tuned in order to improve the predictions.

A 3D simulation of a wind tunnel experiment was conducted. The mesh sizes varied from 690 400 to 5 142 980 cells. The application is to understand street canyon flow better to help assess and prevent risk to human health from pollution or the release of toxic gases. Measurements of velocity vectors and TKE from the wind tunnel experiments compared much better with the CFD model after modification of the turbulence model constants.

Wang *et al.* (2017) used decision trees to learn the Reynolds stress discrepancy for predictive turbulence modelling. Reynolds stresses were predicted in different flows and propagated to mean flow fields. The learning-prediction performance was improved by enriching the input features via an integrity invariants basis of raw mean flow variables.

The application is aerospace. Fully developed turbulent duct flow was modelled. Data of Reynolds numbers of 2 200, 2 600 and 2 900 was used to train and predict flow at a higher Reynolds number of 3 500. The flow contains recirculation bubbles in the corners of the duct. The Launder Gibson RSTM model was used for the baseline simulations since linear eddy viscosity models cannot predict the mean flow features of the secondary motions. Based on testing, an ensemble of 200 trees was large enough to capture the discrepancy function. DNS data was used for validation. Velocity profiles, a Barycentric map of anisotropy, rotation angle of Reynolds stresses, TKE, contour plots of normal Reynolds stress components, normal Reynolds stress imbalance and Reynolds stress shear component of the predictions compared very well to DNS data. The goal of matching in-plane velocity profiles with the DNS data was achieved. The contour and vector plots of the secondary mean flow motions also compared very well. The same tests without the expanded feature space did not deliver the same accuracy. It justified increasing the input features from 10 to 57.

Laubscher (2017) trained an ANN in order to predict the incremental species changes due to chemical reactions.

The goal of the study was to investigate an alternative chemistry integration

approach with reduced solving time compared to the traditional direct integration (DI) and in-situ-tabulation (ISAT). The application was to model the SANDIA D flame with detailed chemistry in a time frame that is suitable for design purposes of industrial furnaces without the need for high-performance computing clusters.

A PFR was modelled by using backward differencing formulation (BDF) and the variable coefficient ordinary differential equation solver (VODE). Random data was generated within a mixture fraction and temperature band of the reacting zone for training of the ANN. It was also used for validation. The activation functions of the ANN used were the hyperbolic-tangent with a linear output function at the final layer. The best network architecture using the stochastic gradient descent with momentum modification as training algorithm, was a single hidden layer and the same amount of neurons in the hidden as the output layer. The prediction error of the ANN was quantified at 2 to 3 % for a quasi global- and 1 % for a detailed mechanism. The solving time was 4 575 times faster than DI, depending on the size of the chemical mechanism.

The ANN chemistry integrator was used with the EDC to model a piloted methane-air turbulent jet diffusion flame, Sandia Flame D. The CFD simulation was 2D-axisymmetric, 700 mm long and 350 mm wide. The mesh size was 2 352 cells. The RSM turbulence model with quadratic pressure strain was chosen for the final results since the peaks of CO and temperature aligned better than using the two equation turbulence models, namely, realizable k-ϵ and k-ω SST. The WD 5 step quasi-global chemical mechanism was used. The magnitude of predicted CO values were lower compared to the measurements due to the global chemical mechanism. For the same reason the temperature predictions were higher than the measurements. The results using the EDC-ANN combination were compared to using the standard EDC implementation with DI and ISAT. All three approaches show comparable accuracy with regard to measurements. The ANN over-predicted H_2 due to the small quantities involved. It was shown that the EDC-ANN and EDM turbulence-chemistry interaction models require almost the same time to solve. Therefore, the EDC-ANN model makes it feasible to solve detailed kinetics in an industrial simulation.

Awais *et al.* (1999) applied a neural network to capture the trends of fuel-bound NO_x release during devolatilisation. The data was obtained from a flat flame turbulent jet apparatus. Large heating rates of the order of 1×10^5 K/s and maximum temperatures of 1 900 K were achieved. The turbulent jet contained combustion gases. These conditions simulate a real boiler environment. Five different pulverised coals were used. The mean flow conditions remained unchanged so that the NO_x measured only depended on the nitrogen released with the volatiles. The structure of the model is a single hidden layer with 2 neurons, 13 inputs and 1 output. The hidden layer utilised a sigmoid activation function and the output layer

function was linear. The proximate analysis, elemental analysis, load, measured O_2 and measured CO_2 were used as inputs with NO_x as output. The steepest descent optimisation technique with momentum modification was used to minimise the error during training. The effect of number of iterations and differing weight initialisation on the model was checked to analyse the stability of the structure. A third data set was used in order to improve the generalisation of the network. The amount of neurons in the hidden layer was increased until the error was acceptable. The model results were within the accuracy tolerance of the experimental data of 10 %. It was concluded that neural networks can be used to predict NO_x emissions from coals in a bench-top experimental device. It is thus a reliable alternative for modelling the complexities of coal combustion.

Deidda *et al.* (2001) trained an ANN to predict the kinetic parameters required in order to determine the devolatilisation characteristics of biomass during combustion. The kinetic rate was a function of the fractions of cellulose, hemicellulose and lignin of the biomass. The size of the particle, temperature, residence time and heating rate were also inputs to the ANN model. A one-step reaction model was used. ANN over training was investigated with a strategy to determine model function smoothness and detection of outliers in the training data.

The application of the model is to predict devolatilisation in CFD combustion codes. Training data was generated from a data-base of 130 experiments on 115 different biomasses and residues. The database included results from TGA, fluidised bed, wire-mesh reactor and pyroprobe experiments. The CHL model was used to generate data for very high heating-rate conditions. Three layers of neurons were used: input, output and hidden layers. Seven input nodes and 12 hidden nodes were used. The sigmoidal function was used as output function. The optimisation algorithm as implemented in the commercial software, MATLAB®, was used to adjust the weights and biases during the learning process. The mean square error was 0.41, equating to a prediction error of 4.6 %. The resulting ANN devolatilisation model was proved to be suitable for CFD combustion codes due to its accuracy and speed. The model was successfully used to predict the amount of volatiles released during the first stages of combustion of biomass and biomass coal blends.

The use of machine learning with CFD is new, but a small group of diverse applications found in literature illustrated the potential. Reduced-order modelling in CFD by means of ANNs was successfully achieved with the desired accuracy and speed-up; in particular, the capturing of time integration of ODEs showed a remarkable reduction in computational cost. An example of the use of ANNs for devolatilisation modelling with the aim to be utilised in CFD was found, confirming the suitability of this artificial intelligence approach in the current study. However, good practice with regard to over-training and quality of data is required.

Chapter 3

Numerical model

The physics modelled in this body of work are the flow of air to a combustion chamber and the mixing with the fuel in the form of injected solid particles. The heterogeneous and homogenous combustion with species transport after chemical reaction and the associated heat transfer are simulated in detail.

Euler and Lagrangian reference frames are used for the continuous gas phase and discrete solid phase, respectively. The two phases interact through the exchange of mass, momentum and energy. The governing differential equations are discretised by a finite volume method.

A brief section covering the conservation equations and closure involved in CFD modelling is included. Since the heterogeneous process of devolatilisation was considered in detail, a concise description of the solid particle phase is added.

An in-depth discussion of the theory behind the advanced models and techniques utilised follows. As in the literature study, turbulence-chemistry interaction, devolatilisation and machine learning are focused on.

3.1 Conservation equations of the fluid phase

Since the flow is predominantly turbulent, the Reynolds averaged form of the governing equations were utilised (dropping the time-dependent term since a steady state was solved for the final application of the research and the over bar on the mean velocity, $\overline{u}$):

$$\frac{\partial}{\partial x_i}(\rho u_i) = S_m \tag{3.1}$$

$$\frac{\partial}{\partial x_j}(\rho u_i u_j) = -\frac{\partial P}{\partial x_i} + \frac{\partial}{\partial x_j}\left[\mu\left(\frac{\partial u_i}{\partial x_j} + \frac{\partial u_j}{\partial x_i} - \frac{2}{3}\delta_{ij}\frac{\partial u_k}{\partial x_k}\right)\right] + \frac{\partial}{\partial x_j}(-\overline{\rho u_i' u_j'}) + \rho g + F \tag{3.2}$$

where ρ and μ is the density and molecular viscosity, respectively.

The RANS equations contain six new variables that can be related to the mean velocity gradients by the Boussinesq hypothesis:

$$-\overline{\rho u_i' u_j'} = \mu_t\left(\frac{\partial u_i}{\partial x_j} + \frac{\partial u_j}{\partial x_i}\right) - \frac{2}{3}\left(\rho k + \mu_t\frac{\partial u_k}{\partial x_k}\right)\delta_{ij} \tag{3.3}$$

The Boussinesq approach is implemented in this work through the k-ϵ turbulence model where two transport equations are solved for the turbulent kinetic energy, k ($k = \frac{1}{2}\overline{u_i' u_i'}$), and the turbulence dissipation rate, ϵ. The turbulent viscosity μ_t is calculated as a function of k and ϵ.

Substituting Equation (3.3) into (3.2) results in:

$$\frac{\partial}{\partial x_j}(\rho u_i u_j) = -\frac{\partial P}{\partial x_i} + \frac{\partial}{\partial x_j}\left[(\mu + \mu_t)\left(\frac{\partial u_i}{\partial x_j} + \frac{\partial u_j}{\partial x_i} - \frac{2}{3}\delta_{ij}\frac{\partial u_k}{\partial x_k}\right) - \frac{2}{3}\delta_{ij}\rho k\right] + \rho g + F \tag{3.4}$$

The mass transfer from the discrete phase takes places via the source term, S_m. In this body of work, it is due to evaporation, boiling, devolatilisation and combustion of the fuel particles.

P is the static pressure, ρg the gravitational body force and F external body forces e.g. from the discrete phase. F can also contain porous-zone and user-defined source terms.

The energy equation is described by the following:

$$\frac{\partial}{\partial x_i}(u_i(\rho E)) = \frac{\partial}{\partial x_i}\left[k_{eff}\frac{\partial T}{\partial x_i} - \sum_j h_j J_{ij}\right] + S_h \tag{3.5}$$

with $E = h$ and equal to the internal energy.

In Equation (3.5) T is temperature. k_{eff} is the effective conductivity ($k + k_t$) with k the thermal- and k_t the turbulent conductivity, depending on the turbulence model. J_{ij} is the diffusion flux vector of species j. S_h is the source term for heat of chemical reaction, radiation, heat transfer between the continuous and discrete phase or any volumetric energy sources defined.

In this research, the variation in density due to pressure is small compared to the variation with temperature. Therefore, the flow was resolved as incompressible

with the pressure-based solver and the variations in density with temperature were accounted for with the ideal-gas relationship. Pressure work, kinetic energy and viscous heating are negligible in this body of work and not included in Equation (3.5).

The species transport equation takes the following form:

$$\frac{\partial}{\partial x_i}(u_i(\rho Y_j)) = \frac{\partial}{\partial x_i} J_{ij} + R_j + S_j \tag{3.6}$$

where Y_j is the mass fraction of species j and R_j is the rate of production or destruction of species j due to chemical reaction. S_j is the rate of creation of species j from the discrete phase and any user defined sources.

Neglecting thermophoretic force, the diffusion flux is written as:

$$J_{ij} = -\left(\rho D_{j,m} + \frac{\mu_t}{Sc_t}\right)\frac{\partial Y_j}{\partial x_i} \tag{3.7}$$

In Equation (3.7) $D_{j,m}$ is the mass diffusion coefficient for species j and Sc_t is the turbulent Schmidt number, $\frac{\mu_t}{\rho D_t}$, with μ_t and D_t the turbulent viscosity and diffusivity, respectively.

3.2 Conservation equations of the solid particle phase

The particle motion with heat- and mass transfer is predicted on the Lagrangian reference frame. The force balance equates the particle inertia with the forces acting on it according to Newton's 2$^{\text{nd}}$ law:

$$\frac{d\mathbf{u}_p)}{dt} = F_D(\mathbf{u} - \mathbf{u}_p) + \frac{\mathbf{g}(\rho_p - \rho)}{\rho_p} \tag{3.8}$$

where $F_D(\mathbf{u} - \mathbf{u}_p)$ is the drag force per unit mass and

$$F_D = \frac{18\mu}{\rho_p d_p^2}\frac{C_D Re_d}{24} \tag{3.9}$$

In Equations (3.8) and (3.9) $\mathbf{u}$ is the fluid phase velocity, $\mathbf{u}_p$ is the particle velocity, μ is the molecular viscosity of the fluid, ρ is the fluid density, ρ_p is the density of the particle and d_p is the particle diameter. Re_d is the relative Reynolds number defined as:

$$Re_d = \frac{\rho d_p |\mathbf{u}_p - \mathbf{u}|}{\mu} \tag{3.10}$$

The drag coefficient C_D is calculated using the non-spherical particle correlation of Haider and Levenspiel (1989):

$$C_D = \frac{24}{Re_{sph}}(1 + b_1 Re_{sph}^{b2}) + \frac{b_3 Re_{sph}}{b_4 + Re_{sph}} \tag{3.11}$$

where

$$b_1 = e^{(2.3288 - 6.4581\phi + 2.4486\phi^2)} \tag{3.12}$$

$$b_2 = 0.0964 + 0.5565\phi \tag{3.13}$$

$$b_3 = e^{(4.905 - 13.8944\phi + 18.4222\phi^2 - 10.2599\phi^3)} \tag{3.14}$$

$$b_4 = e^{(1.4681 + 12.2584\phi - 20.7322\phi^2 + 15.8855\phi^3)} \tag{3.15}$$

The shape factor is defined as:

$$\phi = \frac{s}{S} \tag{3.16}$$

with S the surface area of the particle and s the surface area of a sphere having the same volume as the particle.

The heterogeneous processes involved in the combustion process happen sequentially and are described accordingly:

1. **Inert heating**
   The particle is heated by convection and radiation to the evaporation temperature of the inherent moisture:

   $$m_p c_p \frac{dT_p}{dt} = hA_p(T_\infty - T_p) + \epsilon_p A_p \sigma(\theta_R^4 - T_p^4) \tag{3.17}$$

   where m_p is the particle mass, c_p is the specific heat of the particle, T_p is the particle temperature, h is the convective heat transfer coefficient, A_p is the surface area of the particle, T_∞ is the local temperature of the continuous phase, ϵ_p is the particle emissivity, σ is the Stefan-Boltzmann constant and $\theta_R = (\int_{\Omega=4\pi} I d\Omega / 4\sigma)^{0.25}$ is the radiation temperature. The correlation of Ranz and Marshall (1952a) is used for h:

   $$Nu = \frac{hd_p}{k_\infty} = 2.0 + 0.6 Re_d^{0.5} Pr^{0.333} \tag{3.18}$$

2. **Moisture evaporation**
Since the vaporisation rate of the water in this research is high, the effect of the convective mass transfer from the droplet to the gas is important [Miller *et al.* (1998)][Sazhin (2006)]:

$$\frac{dm_p}{dt} = k_c A_p \rho_\infty ln(1 + B_m) \tag{3.19}$$

where m_p is the water droplet mass, k_c is the mass transfer coefficient, A_p is the droplet surface area and ρ_∞ is the density of the bulk flow. The mass transfer coefficient is calculated from the Sherwood correlation [Ranz and Marshall (1952a)][Ranz and Marshall (1952b)]:

$$Sh_{AB} = \frac{k_c d_p}{D_{j,m}} = 2.0 + 0.6 Re_d^{0.5} Sc^{0.333} \tag{3.20}$$

where $D_{j,m}$ is the diffusion coefficient of vapor in the bulk flow and Sc is the Schmidt number, $\frac{\mu}{\rho D_{j,m}}$.

The Spalding number B_m is given by:

$$B_m = \frac{Y_{i,s} - Y_{i,\infty}}{1 - Y_{i,s}} \tag{3.21}$$

where $Y_{i,s}$ is the vapour mass fraction at the surface and $Y_{i,\infty}$ is the vapour mass fraction in the bulk flow.

The heating of the droplet during evaporation is handled by adding a latent heat term, $-\frac{dm_p}{dt} h_{fg}$, to the right-hand side of Equation (3.17) and h calculated with a modified Nu for convective mass transfer.

3. **Boiling**
When the droplet temperature reaches the boiling point, a boiling rate equation is applied at constant temperature [Kuo (2005)]:

$$\frac{d(d_p)}{dt} = \frac{4k_\infty}{\rho c_{p,\infty} d_p}(1 + 0.23\sqrt{Re_d}) ln\left[1 + \frac{c_{p,\infty}(T_\infty - T_p)}{h_{fg}}\right] \tag{3.22}$$

where $c_{p,\infty}$ is the heat capacity of the gas and k_∞ is the thermal conductivity of the gas.

4. **Devolatilisation**
Devolatilisation takes place when the particle reaches the vaporisation temperature. The single-rate model assumes that the rate of volatile release is first order dependent on the amount of volatiles remaining:

$$-\frac{dm_p}{dt} = k[m_p - (1 - f_{v,0})(1 - f_{w,0})m_{p,0}] \tag{3.23}$$

where $f_{v,0}$ is the fraction of volatiles initially present in the particle, $f_{w,0}$ is the initial fraction of evaporating or boiling material and $m_{p,0}$ is the initial particle mass. The kinetic rate is calculated by:

$$k = Ae^{-\frac{E}{RT_p}} \tag{3.24}$$

where A and E is the pre-exponential factor and activation energy respectively. The temperature of the particle is calculated with Equation (3.17) during devolatilisation.

5. **Surface combustion**
After the volatiles are consumed, combustion of the char takes place according to the diffusion-limited model of Baum and Street (1971):

$$\frac{dm_p}{dt} = -4\pi d_p D_{j,m} \frac{Y_{OX} T_\infty \rho}{S_b(T_p + T_\infty)} \tag{3.25}$$

where $D_{j,m}$ is the diffusion coefficient for the oxidant in the bulk flow, Y_{OX} is the local mass fraction of the oxidant and S_b is the stoichiometry in mass of oxidant per mass of char. The heating of the particle during combustion is handled by adding a heat of reaction term, $-f_h \frac{dm_p}{dt} H_{reac}$, to the right-hand side of Equation (3.17). H_{reac} is the heat released by the surface reaction and f_h is the fraction of this energy that is absorbed by the particle.

3.3 The EDC

The EDC has the advantage of incorporating finite-rate kinetics at a moderate computational expense compared to the composition PDF transport model. This benefit comes at the expense of a less accurate representation of the turbulent temperature fluctuations.

The effect of turbulence on the chemical reactions is taken into account by referring to a phenomenological description in terms of the turbulent energy cascade. Important variables in this description is the energy dissipation rate ϵ and characteristics of the viscous scale of the flow (Kolmogorov scale) which depends on ϵ and kinematic viscosity, ν. The length, time and velocity scales of the energy-containing range of the spectrum are denoted by l_t, T_t and u', respectively. The turbulent Reynolds number then follows:

$$Re_t = \frac{u' l_t}{\nu} \tag{3.26}$$

The length, time and velocity scales are calculated from a turbulence model. In the case of k-ϵ models $l_t = \frac{k^{3/2}}{\epsilon}$, $T_t = \frac{k}{\epsilon}$, $u' = \sqrt{k}$ and $Re_t = \frac{k^2}{\nu\epsilon}$.

The turbulent Reynolds number relates the Kolmogorov scales of length, time and velocity, η, τ_K, n_K, to the scales of the energy containing range via:

$$Re_t = \left(\frac{T_t}{\tau_K}\right)^2 = \left(\frac{l_t}{\eta}\right)^{4/3} = \left(\frac{u'}{u_K}\right)^4 \tag{3.27}$$

Reactions occur in the fine scales where the combustible fluid is mixed at the micro-scale level. The computational cell is therefore divided into two sub-zones namely the fine structure and surrounding fluid, as shown in Figure 3.1. All the homogeneous chemical reactions take place in the fine structure zone where it is treated as adiabatic, isobaric, PSRs. Mass and energy is transported to the surrounding fluid where only turbulent mixing takes place without chemical reaction. The reaction rate is calculated from a mass balance of the fine scales reactor:

$$\overline{\dot{\omega}_k} = \frac{\overline{\rho}\gamma^2\lambda}{\tau^*}(Y_k^* - Y_k^o) \tag{3.28}$$

where Y_k^* and Y_k^o are the mass fractions of species, k, in the fine structure and surrounding fluid, respectively. The mean residence time, τ^* is the inverse of the mass transfer rate between the two sub-zones. The fraction of the fine structure where chemical reactions take place is given by λ. A sensitivity analysis conducted by Orszag *et al.* (1993) revealed that $\lambda = 1$ is recommended for detailed chemistry. The length fraction of the fine structure is denoted by γ and $\overline{\rho}$ represents the average density in the computational cell.

The mean mass fraction of species k is a linear combination of the properties in the two sub-zones:

$$\overline{Y}_k = \gamma^3 Y_k^* + (1 - \gamma^3) Y_k^0 \tag{3.29}$$

Combining Equations (3.28) and (3.29):

$$\overline{\dot{\omega}_k} = \frac{\overline{\rho}\gamma^2}{\tau^*(1 - \gamma^3)}(Y_k^* - \overline{Y}_k) \tag{3.30}$$

The length fraction of the fine structure, γ, and mean residence time, τ^*, are calculated as follows:

$$\gamma = C_\gamma \left(\frac{\nu\epsilon}{k^2}\right)^{1/4} = C_\gamma \left(\frac{l_t}{\eta}\right)^{-1/3} = C_\gamma Re_t^{-1/4} \tag{3.31}$$

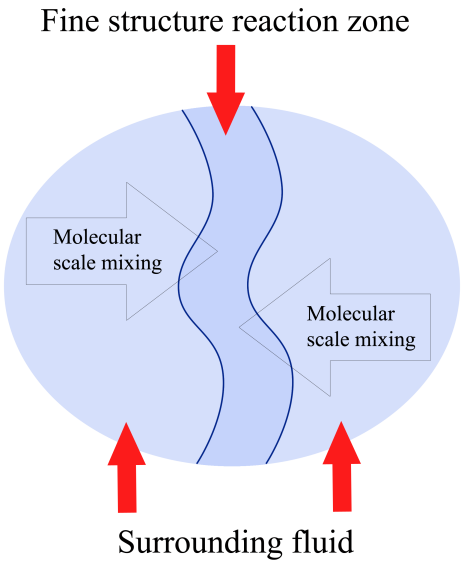

Figure 3.1: Schematic of cell based on EDC

$$\tau^* = C_\tau \left(\frac{\nu}{\epsilon}\right)^{1/2} = C_\tau \tau_K = C_\tau Re_t^{-1/2} T_t = C_\tau Re_t^{-1/2} \frac{k}{\epsilon} \tag{3.32}$$

where the model constants have the default values $C_\gamma = 2.1377$ and $C_\tau = 0.4082$. These values follow from related model constants $C_{D1} = 0.135$ and $C_{D2} = 0.5$. The former is dependent on the turbulence model and the latter fitted to experimental data as described by Laubscher (2017):

$$C_\gamma = \left(\frac{3C_{D2}}{4C_{D1}}\right)^{0.25} \tag{3.33}$$

$$C_\tau = \left(\frac{C_{D2}}{3}\right)^{0.5} \tag{3.34}$$

Equations 3.26 to 3.32 are from De *et al.* (2011). The variable Y_k^* is the species mass fraction reached from the current value $\overline{Y}_k$ applying the chemical reaction over a time τ^*. In the original formulation of the EDC, it was stated that the steady state condition of a well-stirred reactor (WSR) should be used to calculate Y_k^*. This approach requires solving a set of non-linear algebraic equations that are numerically stiff due to the Arrhenius form reactions rates. It was shown by

Jessee *et al.* (1993) that a PFR approach can be used to simplify the solution and increase numerical stability since it is integrated over the residence time. The PFR and WSR approaches deliver similar results for conditions of slight exothermicity and very small conversion [De *et al.* (2011)]. The following equation is used for a PFR in this research as implemented in ANSYS® Fluent:

$$\frac{dY_k^*}{d\tau^*} = \frac{\dot{\omega}_k}{\rho} \tag{3.35}$$

A chemical mechanism of N species and Z reactions can be described by:

$$\sum_{k=1}^{N} \nu'_{r,k} X_k \leftrightarrow \sum_{k=1}^{N} \nu''_{r,k} X_k \quad r = 1, 2, 3, ..., Z \tag{3.36}$$

where X is the molecular formula for species k. $\nu'_{r,k}$ and $\nu''_{r,k}$ is the stoichiometric coefficient of species k in reaction r as reactant and product, respectively.

The reaction rate term $\dot{\omega}_k$ in Equation (3.35) is then calculated using the following:

$$\dot{\omega}_k = M_{w,k} \sum_{r=1}^{Z} (\nu''_{r,k} - \nu'_{r,k}) q_r \tag{3.37}$$

In Equation (3.37) $M_{w,k}$ is the molecular weight and q_r is the rate of reaction r defined by:

$$q_r = k_{fr} \prod_{k=1}^{N} [C_k]^{\nu'_{r,k}} - k_{rr} \prod_{k=1}^{N} [C_k]^{\nu''_{r,k}} \tag{3.38}$$

C_k is the molar concentration $\left(\frac{\rho Y_k}{M_k}\right)$ of species k in Equation (3.38). k_{fr} and k_{rr} is the forward and reverse reaction rate, respectively [Kuo (2005)]. These reaction rates are calculated by the Arrhenius law:

$$k_r = A_r T^{\beta_r} e^{\frac{-E_r}{RT}} \tag{3.39}$$

where A_r is the pre-exponential factor, β_r is the temperature exponent, R is the universal gas constant and E_r is the activation energy. The activation energy and pre-exponential factor are experimentally determined for elementary reactions. The stoichiometric values in Equation (3.38) are replaced with reaction orders for global and quasi-global mechanisms [Kuo (2005)].

By inspecting Equation (3.30) it can be seen that the mean chemical state evolves via a linear relaxation process, typical of mixing, towards a reacted state involving a non-linear reaction process after time τ^*. The time scale of mixing is

of the order of the time scale of the energy containing scales of turbulence which is larger than τ^*:

$$\frac{1}{\tau_{mix}} = \frac{\gamma^2}{(1-\gamma^3)}\frac{1}{\tau^*} = \frac{1}{(1-\gamma^3)}\left(\frac{C_\gamma^2}{C_\tau}\frac{1}{T_t}\right) \tag{3.40}$$

This research is focused on industrial application with varying length and temporal scales, which is a challenging environment for model validity. It is therefore of interest to check the sensitivity of the predicted reaction rate to the model constants, C_γ and C_τ. The constant C_τ is a multiplicative factor for the time scale τ^* and thus the reaction rate term. The time scale ratio is calculated as follows:

$$R = \frac{\tau^*}{\tau_{mix}} = \frac{\gamma^2}{(1-\gamma^3)} \tag{3.41}$$

For consistency, γ and R must be lower than one. The default value of C_γ limits the model applicability to $Re_t > 64$. For $R = 1$, using the PFR approach equation (3.30) reduces to:

$$\overline{\dot{\omega}_k} = \frac{\overline{\rho}}{\tau^*}(Y^*_{k(t+\tau^*)} - \overline{Y}_{k(t)}) \tag{3.42}$$

Equation (3.42) can be described as a first-order discretisation of laminar finite-rate chemical kinetics.

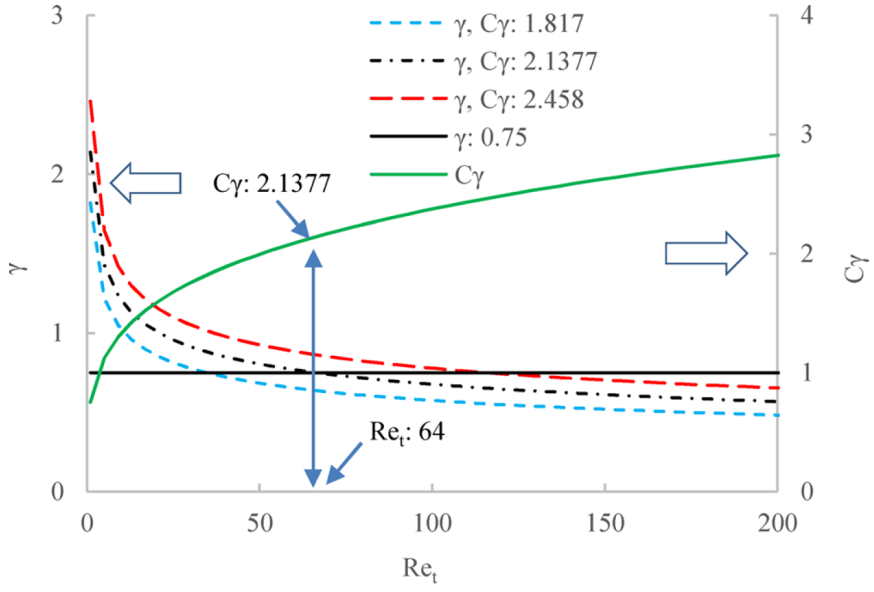

Figure 3.2: Dependence of γ and C_γ on Re_t [Farokhi and Birouk (2016*a*)]

Using the commercial CFD software ANSYS® Fluent in this research, the hard limit of $Re_t = 64$ sets γ to 0.75, as seen in Figure 3.2 for $C_\gamma = 2.1377$. This predicts unrealistic high reaction rates for $Re_t < 64$ due to the turbulent diffusion of species in combination with laminar kinetics. It is also shown in Figure 3.2 that changing C_γ to a lower value forces the switch to laminar kinetics at a lower Re_t, making it possible to apply the EDC to low turbulent flow regions.

There is also room for improvement in high turbulent flows where the chemical kinetics is very fast compared to the mixing. It was shown by Rehm *et al.* (2008) that results can be improved by using the time scale of the energy-containing range of the turbulence spectrum for the reactor residence time. Setting $\frac{T_t}{\tau_{mix}} = 1$ in Equation (3.40) with $\frac{1}{(1-\gamma^3)}$ approaching 1 results in:

$$C_\tau = C_\gamma^2 \tag{3.43}$$

Thus by using Equation (3.43) as an indication of an upper limit for C_τ with respect to C_γ, the reaction rate can be reduced in high turbulent flows if the EDC model over-predicts temperature according to Farokhi and Birouk (2016*b*). The highest value applied for the mixing time scale in literature is the Taylor time scale used by Kjäldman *et al.* (1999) which is $4k/\epsilon$. This translates into substituting double the value of C_γ into Equation (3.43). The default value of C_τ can be considered as a lower limit since it translates into a fraction of the Kolmogorov time scale for the reactor residence time.

Another deficiency of the EDC implementation in ANSYS® Fluent is the prediction of the reaction rate for species that are related to slow chemistry or low Damköhler number. The following definition for Damköhler number from Kuo (1986) is used in this body of work:

$$Da = \frac{\tau_{mix}}{\tau_{chem}} \tag{3.44}$$

where τ_{mix} is the mixing time scale and τ_{chem} is the chemical time scale. Using the Kolmogorov time scale, $(\nu/\epsilon)^{1/2}$, for mixing and the inverse of the chemical-reaction rate constant, $1/k$, for the chemical time scale results in:

$$Da = k\left(\frac{\nu}{\epsilon}\right)^{1/2} \tag{3.45}$$

Since the default value of C_τ is already the lower limit, the reaction rate can be increased with a higher value of C_γ. In this way, the volume of the fine structure is extended to the surrounding fluid and a part of the surrounding fluid is accounted for in the reaction zone. This approach has been suggested by Kjäldman *et al.* (1999) for slow chemical reactions. However, as shown in Figure 3.2, it shifts the

switch to laminar kinetics in the direction of higher Re_t, making low Reynolds number regions less accurate.

From the preceding paragraphs it is evident that a modification of the EDC model constants must be performed by considering the chemistry and flow together. For example, while a lower value of C_γ may improve the predictions at low turbulent flow conditions, it could under-predict slow chemistry.

The two main deficiencies of the current EDC implementation in ANSYS® Fluent, namely low Reynolds conditions and slow chemistry, can be corrected by customisation of the code; however, it is out of the scope of the current research. The hybrid low-Reynolds model of Shiehnejadhesar *et al.* (2014) can be used in combination with a modification of Equation (3.28) to account for the reactions in the surrounding fluid as shown by Magnussen (2005).

3.4 The CPD model

The CPD model characterises the chemical and physical processes by considering the biomass as a lattice or chemical bridges that connects the structural clusters in a network. The modelling of bridge cleavage and generation of light gas, tar and char is shown in Figure 3.3. The variable $\pounds$ represents the original population of labile bridges. When heated, these bridges become reactive bridges, $\pounds^*$. Two competing pathways exist for the reactive bridges. In one path, side chains, δ, are formed that may detach to form light gas, g_1. As bridges are cleaved, a fraction of the biomass becomes detached from the lattice. These detached clusters are the heavy-molecular-weight tar precursors that form the metaplast. The metaplast vaporise to form tar. It can also reattach to the lattice matrix; a process referred to as cross linking. In the other path, char, c, is formed with the release of light gas, g_2. The total population of bridges can be represented by the variable p, where $p = \pounds + c$.

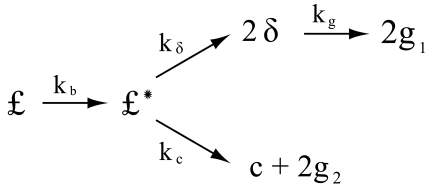

Figure 3.3: Chemical reaction scheme

With reference to Figure 3.3 where the variables that characterise the biomass lattice structure during devolatilisation is shown, the following reaction rates can be defined with a steady state assumption for the reactive bridges:

$$\frac{d\pounds}{dt} = -k_b \pounds \tag{3.46}$$

$$\frac{dc}{dt} = k_b \frac{\pounds}{\rho + 1} \tag{3.47}$$

$$\frac{d\delta}{dt} = \left[2\rho k_b \frac{\pounds}{\rho + 1} \right] - k_g \delta \tag{3.48}$$

$$\frac{dg_1}{dt} = k_g \delta \tag{3.49}$$

$$\frac{dg_2}{dt} = 2\frac{dc}{dt} \tag{3.50}$$

The bridge-breaking and gas-release rates, k_b and k_g, are expressed in Arrhenius form with a distributed activation energy, E_σ:

$$k = Ae^{-\frac{(E \pm E_\sigma)}{RT}} \tag{3.51}$$

where A, E, and E_σ is the pre-exponential factor, activation energy and the standard deviation of activation energy, respectively. $\rho = k_\delta / k_c$ is the char-to-gas kinetic ratio. Mass conservation is imposed with the following relationships:

$$g = g_1 + g_2 \tag{3.52}$$

$$g_1 = 2f - \sigma \tag{3.53}$$

$$g_2 = 2(c - c_0) \tag{3.54}$$

where f is the fraction of broken bridges, $f = 1 - p$. The initial conditions of the ordinary differential equation system are the following:

$$c(0) = c_0 \tag{3.55}$$

$$\pounds(0) = \pounds_0 = p_0 - c_0 \tag{3.56}$$

$$\delta(0) = 2f_0 = 2(1 - c_0 - \pounds_0) \tag{3.57}$$

$$g(0) = g_1(0) = g_2(0) = 0 \tag{3.58}$$

c_0, $\pounds_0$ and p_0 is the initial fraction of char-, labile- and total bridges, respectively.

The fractional change in biomass mass is divided in light gas (f_{gas}), tar precursor fragments (f_{frag}) and char (f_{char}). The following relationships relate the set of reaction equations for the biomass structure to the changes in mass and related volatile products:

$$f_{gas}(t) = \frac{r(g_1 + g_2)(\sigma + 1)}{4 + 2r(1 - c_0)(\sigma + 1)} \tag{3.59}$$

$$f_{frag}(t) = \frac{2}{2 + r(1 - c_0)(\sigma + 1)}[\phi F(p) + r\Omega K(p)] \tag{3.60}$$

$$f_{char}(t) = 1 - f_{gas}(t) - f_{frag}(t) \tag{3.61}$$

The statistical relationships ϕ, Ω, $F(p)$ and $K(p)$ are related to the cleaving of bridges via percolation lattice statistics and described by the following:

$$\phi = 1 + r\left[\frac{\pounds}{p} + \frac{(\sigma - 1)\delta}{4(1 - p)}\right] \tag{3.62}$$

$$\Omega = \frac{\delta}{2(1 - p)} - \frac{\pounds}{p} \tag{3.63}$$

$$F(p) = \left(\frac{p'}{p}\right)^{\frac{\sigma+1}{\sigma-1}} \tag{3.64}$$

$$K(p) = \left[1 - \left(\frac{\sigma + 1}{2}\right)p'\right]\left(\frac{p'}{p}\right)^{\frac{\sigma+1}{\sigma-1}} \tag{3.65}$$

The ratio of bridge- to site mass is given by:

$$r = \frac{m_b}{m_a} \tag{3.66}$$

$$m_b = 2M_{w,\delta} \tag{3.67}$$

$$m_a = M_{w,1} - (\sigma + 1)M_{w,\delta} \tag{3.68}$$

$M_{w,\delta}$ and $M_{w,1}$ is the side-chain- and cluster molecular weight, respectively.$\sigma+1$ is the lattice coordination number and p' is the root of the following:

$$p'(1 - p')^{\sigma-1} = p(1 - p)^{\sigma-1} \tag{3.69}$$

The part of the metaplast that vaporises is treated in an approach similar to flash vaporisation. It is assumed that vapour/liquid phase equilibrium happens on a time scale that is very fast compared to the bridge reactions. A vapour pressure correlation based on Raoult's Law is used as an estimate of the phase composition. The following equation is used for the cross-linking of the metaplast to the biomass lattice:

$$\frac{dm_{cross}}{dt} = m_{frag} A_{cross} e^{\frac{-E_{cross}}{RT}} \tag{3.70}$$

m_{cross} is the amount of mass reattaching to the matrix and m_{frag} is the mass in the metaplast. A_{cross} and E_{cross} is the pre-exponential factor and activation energy of the cross-linking rate, respectively. Equations 3.46 to 3.70 are from Fletcher *et al.* (1992).

The devolatilisation of biomass is modelled as a mass-weighted combination of the components, namely cellulose, hemicellulose and lignin. Therefore, the theory explained above is applied for each component with its respective structural and kinetic parameters.

The CPD model requires a base structural unit. Lewis and Fletcher (2013) defined the fixed anomeric carbon and attached hydrogen as the base cluster for cellulose and hemicellulose as shown in Figure 3.4. Coniferyl, coumaryl and sinapyl alcohols were used as the base unit for lignin. The parameters used in this body of work from Lewis and Fletcher (2013) are based on these structures and NMR measurements as given in Table 3.1.

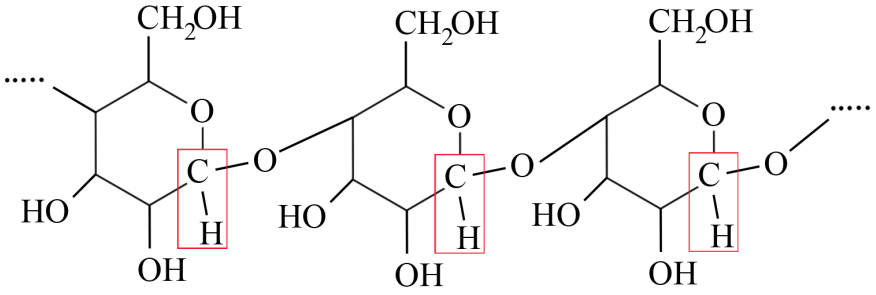

Figure 3.4: Anomeric carbon in cellulose

The kinetic parameters utilised in this research came from fine-tuning using pyrolysis data and an optimisation routine by Fletcher *et al.* (2012). It is shown in Table 3.2 with E_c the difference in activation energy between bridge breaking and char formation.

Table 3.1: Structural parameters for biomass components

Structural parameter	$M_{w,l}$	M_δ	p_0	$\sigma + 1$	c_0
Cellulose	81	22.7	1.0	3.0	0.0
Softwood hemicellulose	81	22.7	1.0	3.0	0.0
Softwood lignin	186	34	0.71	3.5	0.0

Table 3.2: Kinetic parameters for biomass components

kinetic parameter	cellulose	hemicellulose	lignin
E_b kcal/mol	55.4	51.5	55.4
A_b s^{-1}	2.0×10^{16}	1.2×10^{20}	7.0×10^{16}
$E_{\sigma,b}$ kcal/mol	4.1	0.1	0.5
E_g kcal/mol	61.2	38.2	69.0
A_g s^{-1}	3.0×10^{15}	3.0×10^{15}	2.3×10^{19}
$E_{\sigma,g}$ kcal/mol	8.1	5.0	2.6
ρ	100	1.35	1.7
E_c kcal/mol	0.0	0.0	0.0
E_{cross} kcal/mol	65.0	65.0	65.0
A_{cross} s^{-1}	3.0×10^{15}	3.0×10^{15}	3.0×10^{15}

3.5 Artificial neural networks

ANNs is a technique used in machine learning, computer- and cognitive science to approximate complex functions with a high dimensional space [Laubscher (2017)].

ANNs are inspired by biological neurons in the human and animal brain. The human brain consists of 10^{11} neurons with approximately 10^4 connections per element. Neurons have three main components: the dendrites, cell body and axon, as shown in Figure 3.5. The tree-like receptive networks of dendrites carry the electrical signals to the cell body. The cell body sums and thresholds the signals. The axon is a single long fibre that transmits the signal to another neuron's dendrite via a synapse.

There are two key similarities between artificial and biological networks. Both are computational devices that are highly interconnected and the connections between neurons determine the function of the network [Hagan and Demuth (2014)].

The mathematical equivalent of a single neuron is shown in Figure 3.6. The scalar input p is multiplied by the scalar weight w. The other input 1 is multiplied

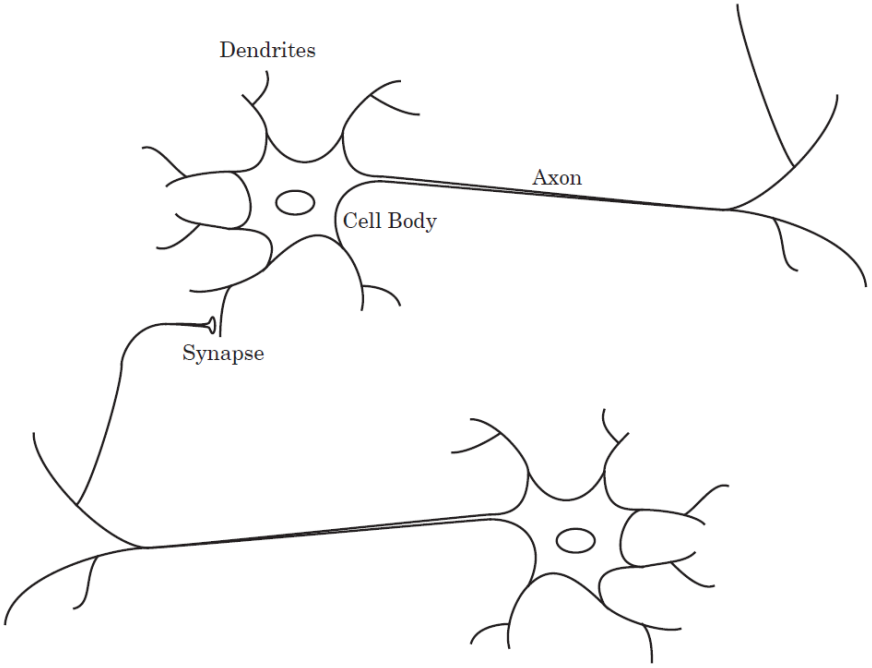

Figure 3.5: Schematic drawing of biological neurons [Hagan and Demuth (2014)]

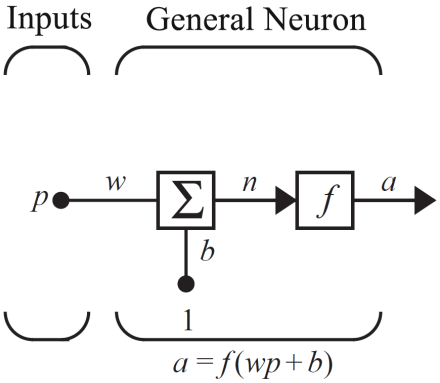

Figure 3.6: Single input neuron [Hagan and Demuth (2014)]

by a bias b and added to $w \times p$. The output from the summer is passed through a transfer or activation function to give the output from the neuron.

In relation to its biological counterpart: the weight w corresponds to the strength of a synapse, the cell body is the summer with activation function and the output a is the signal on the axon.

ANNs are formed by multiple layers of multiple neurons. The first and last layer is called the input layer and output layer, respectively, with the ones in-between called hidden layers. This type of ANN is a feedforward multi-layer perceptron neural network.

The two modes of ANN operation are feedforward- and backward propagation. The former is used to calculate the network output from the input variables of the feature space for a single data set observation. The latter technique is used to adjust the weights and biases in order to map data set input-output pairs via the network.

3.5.1 Feedforward propagation

The feedforward propagation is described by Figure 3.7 for a single layer.

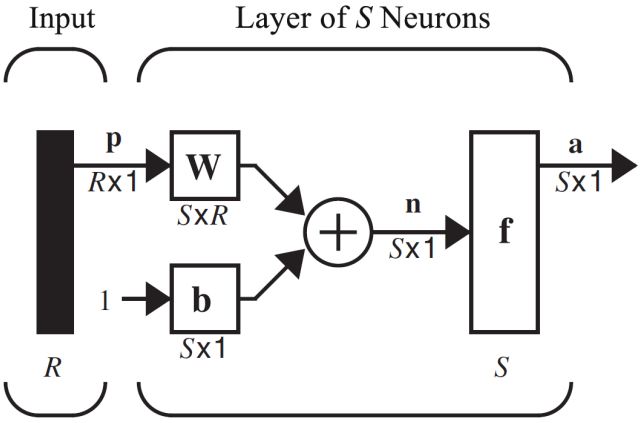

Figure 3.7: Layer of S neurons with R inputs in matrix notation [Hagan and Demuth (2014)]

The output of the layer is calculated as:

$$\mathbf{a} = f(\mathbf{W}\mathbf{p} + \mathbf{b}) \tag{3.71}$$

with:

$$\mathbf{a} = \begin{bmatrix} a_1 \\ a_2 \\ \vdots \\ a_S \end{bmatrix} \mathbf{W} = \begin{bmatrix} w_{1,1} & w_{1,2} & \dots & w_{1,R} \\ w_{2,1} & w_{2,2} & \dots & w_{2,R} \\ \vdots & \vdots & \vdots & \vdots \\ w_{S,1} & w_{S,2} & \dots & w_{S,R} \end{bmatrix} \mathbf{p} = \begin{bmatrix} p_1 \\ p_2 \\ \vdots \\ p_R \end{bmatrix} \mathbf{b} = \begin{bmatrix} b_1 \\ b_2 \\ \vdots \\ b_S \end{bmatrix}$$

The following operation is performed per neuron, using the first neuron as an example:

$$n_1 = w_{1,1}p_1 + w_{1,2}p_2 + ... + w_{1,R}p_R + b_1 \tag{3.72}$$

The general formulation of Equation 3.72 for the i^{th} neuron is:

$$n_i = \sum_{j=1}^{R} w_{i,j}p_j + b_i \tag{3.73}$$

The cumulative signal is passed into an activation function. The following functions are examples:

$$a_i = n_i \quad \text{Linear function}$$

$$a_i = \frac{1}{1 + e^{-n_i}} \quad \text{Log-sigmoid function}$$

$$a_i = \frac{e^{n_i} - e^{-n_i}}{e^{n_i} + e^{-n_i}} = tanh(n_i) \quad \text{Hyperbolic-tangent sigmoid function}$$

Multiple layers can be combined to form networks. The inputs can be from a previous layer or the actual values from the data set observation. Similarly, the outputs can be transferred to the next layer or it can be the output of the network to be compared to the actual values from the data set observation.

We can define an input $\mathbf{p}$ and output $\mathbf{t}$ data set with q observations. The input data is thus a vector of size q: $\mathbf{p} = \mathbf{p}_1, \mathbf{p}_2, \mathbf{p}_3, \dots, \mathbf{p}_q$, similarly for the output data: $\mathbf{t} = \mathbf{t}_1, \mathbf{t}_2, \mathbf{t}_3, \dots, \mathbf{t}_q$. Each input and output observation is a vector of length d_{in} and d_{out}, respectively corresponding to its dimensionality.

A performance function is required to determine the accuracy of the ANN with respect to the desired outputs from the data set. The mean-squared error (MSE) is commonly used. The in-sample error for an observation is:

$$e(\mathbf{x}) = \sum_{i=1}^{d_{out}} (t_i - a_i)^2 \tag{3.74}$$

where $\mathbf{a}$ is a vector of length d_{out} corresponding to the outputs from the network with input vector $\mathbf{p}$ and $\mathbf{x}$ is a vector containing all network weights and biases.

It can be seen from Equation (3.74) that the in-sample error is a function of the outputs from the ANN that is determined by the weights and biases. The weights and biases thus need to be optimised to minimise the in-sample error. This procedure is called learning.

3.5.2 Backward propagation

There are three categories of learning methods: supervised-, unsupervised- and reinforcement learning. In the current research a training set is provided for the ANN behaviour and this falls under supervised learning. The weights and biases are optimised using back propagation and the Levenberg-Marquardt algorithms. Since the Levenberg-Marquardt algorithm is a variation of the optimisation involved during the process, the standard formulation is described first. As the dimensionality of the feature and response space increases, the ANN requires more flexibility and the amount of fitting variables increases. The trough of the resulting high-dimensional plane corresponding to the lowest error must be found. Gradient descent is used to adjust the weights in the direction of the steepest gradient, thus minimising Equation (3.74). The following equations are used:

$$w_{i,j}(k+1) = w_{i,j}(k) - \alpha \frac{\partial e(\mathbf{x})}{\partial w_{i,j}} \tag{3.75}$$

$$b_i(k+1) = b_i(k) - \alpha \frac{\partial e(\mathbf{x})}{\partial b_i} \tag{3.76}$$

where k is the iteration counter and α the learning rate.

The learning rate relaxes the solution and reduces overshoot. The back-propagation procedure relates a specific weight and bias in the network to the performance function through the $\partial e(\mathbf{x})/\partial w_{i,j}$ and $\partial e(\mathbf{x})/\partial b_i$ terms in Equations (3.75) and (3.76), respectively. A large change to a particular weight or bias is made if the change leads to a large reduction in error. Changes in the final layer is computed first. The procedure is repeated for the penultimate layer and ultimately to the first hidden layer. Therefore, the network is updated in the reverse direction and the method is called back-propagation. Following Equations (3.75) and (3.76) and applying the chain rule:

$$\frac{\partial e(\mathbf{x})}{\partial w_{i,j}} = \delta_i^{(l)} \times p_j \tag{3.77}$$

$$\frac{\partial e(\mathbf{x})}{\partial b_i} = \delta_i^{(l)} \tag{3.78}$$

where $\delta_i^{(l)} = \partial e(\mathbf{x})/\partial n_i$ and changes between different layers in a multilayer network. For the hyperbolic-tangent sigmoid activation function in the final layer it is expressed as:

$$\delta_i^{(L)} = 2(tanh(n_i) - t_i)(1 - tanh^2(n_i)) \tag{3.79}$$

For any other layer in the network with the hyperbolic-tangent sigmoid activation function:

$$\delta_i^{(l)} = [1 - a_i^2] \sum_{j=1}^{d^{(l+1)}} w_{i,j}^{(l+1)} \delta_j^{(l+1)} \tag{3.80}$$

where a_i is the output of the layer for the i^{th} neuron, $w_{i,j}^{(l+1)}$ is the weight in the transposed matrix of the next layer and $\delta_j^{(l+1)}$ is calculated for the next layer. $d^{(l+1)}$ is the amount of neurons in the next layer. The calculation starts at the final layer based on Equation 3.79. The derivation of Equation (3.80) is shown in Hagan and Demuth (2014). Similar to the feedforward propagation, the backward propagation equations are vectorised:

$$\overline{\delta}^{(l)} = \mathbf{U}^{(l)} \cdot (\Gamma^{(l+1)} \overline{\delta^{(l+1)}}) \tag{3.81}$$

where in equation (3.81) the following variables are defined in a similar way to [Laubscher (2017)]:

$$\overline{\delta^{(l+1)}} = \begin{bmatrix} \delta_1^{(l+1)} \\ \delta_2^{(l+1)} \\ \delta_3^{(l+1)} \\ \vdots \\ \delta_{d^{(l+1)}}^{(l+1)} \end{bmatrix} \quad \mathbf{U}^{(l)} = \begin{bmatrix} 1 - a_1^2 \\ 1 - a_2^2 \\ 1 - a_3^2 \\ \vdots \\ 1 - a_{d^{(l+1)}}^2 \end{bmatrix}$$

$$\Gamma^{(l+1)} = \begin{bmatrix} w_{1,1}^{(l+1)} & w_{1,2}^{(l+1)} & \dots & w_{1,d^{(l+1)}}^{(l+1)} \\ w_{2,1}^{(l+1)} & w_{2,2}^{(l+1)} & \dots & w_{2,d^{(l+1)}}^{(l+1)} \\ \vdots & \vdots & \vdots & \vdots \\ w_{d^{(l)},1}^{(l+1)} & w_{d^{(l)},2}^{(l+1)} & \dots & w_{d^{(l)},d^{(l+1)}}^{(l+1)} \end{bmatrix}$$

The Levenberg-Marquard algorithm was designed for second-order training speed without the need of the Hessian matrix. For Equation (3.74), the Hessian matrix can be approximated as:

$$\mathbf{H} = \mathbf{J}^T \mathbf{J} \tag{3.82}$$

The gradient is calculated as follows:

$$\mathbf{g} = \mathbf{J}^T\mathbf{e} \tag{3.83}$$

where $\mathbf{J}$ is the Jacobian matrix with first derivatives of network errors with respect to the weights and biases. $\mathbf{e}$ is a vector of network errors. Equations (3.75) and (3.76) are re-written as:

$$\mathbf{x}(k+1) = \mathbf{x}(k) - [\mathbf{J}^T\mathbf{J} + \mu\mathbf{I}]^{-1}\mathbf{J}^T\mathbf{e} \tag{3.84}$$

where $\mathbf{I}$ is the identity matrix and μ a scalar which is decreased when the performance function reduces and increased with an increase in error. When μ is zero, it is Newton's method with the approximated Hessian matrix, and when μ is large, it becomes gradient descent with a small step size. Since Newton's method is faster and more accurate near an error minimum, the goal is to shift to Newton's as soon as possible while still ensuring that the Hessian matrix is positive-definite [Marquardt (1963)] [Hagan and Menhaj (1999)].

The Levenberg-Marquard method was chosen for this study since it is more accurate than gradient descent. Laubscher (2017) used a momentum modification to the gradient descent algorithm in order to decrease the probability of getting stuck in a local minimum in the high-dimensional solution space of weights.

The training data set used in this research was generated solving a set of ODEs and, therefore, there is no noise in the data. For this reason, regularisation was not used.

Chapter 4

Development of reduced-order model

The following section describes the procedure followed in order to develop and implement a reduced-order submodel in the commercial CFD code, ANSYS® Fluent.

Machine learning was used to develop the model since it is suited to determine the relationship between variables in a multi-dimensional data space.

ANNs is a very accurate and customisable machine-learning technique. It was therefore chosen in view of formulating a general framework.

The current research captured only total volatile yield of the Bio-CPD model as a function of time and temperature. However, more parameters of the Bio-CPD or a combination of different models and experimental data for training could be required in the future. Neural networks are more adaptable for these purposes.

4.1 Training data set generation

Before the training data can be generated, it has to be specified within the constraints of the application. A neural network requires input-output pairs in order to apply the training algorithm. Therefore, the minimum amount of inputs to calculate a desired output has to be determined. In the case of commercial CFD submodels, there are also restrictions on the variables available due to the interfacing with the main source code. ANNs excel in interpolation, but extrapolation is not recommended. The limits of the model is therefore also very important and determines the applicability.

The current study upgraded the devolatilisation model in ANSYS® Fluent to be sensitive to heating rate. This is the only benefit of using Bio-CPD with a pseudo volatile chemical species released from the surface of the particle, as is the current implementation in ANSYS® Fluent. More benefits of using an advanced

devolatilisation model such as Bio-CPD can be pursued by specifying the volatile composition in terms of tar, light gases and nitrogen. The split between these components could be taken from the Bio-CPD model instead of using constant values based on a mass energy balance of the ASTM proximate analysis.

A hybrid model consisting of an ANN and a one-step reaction is used. This model assumes that the rate of devolatilisation is first-order dependent on the amount of volatiles remaining in the particle:

$$\frac{dV}{dt} = k(V_\infty - V) \tag{4.1}$$

where V is the current - and V_∞ the final volatile yield. The kinetic rate, k is usually defined in Arrhenius form. In this research, it is calculated by the ANN based on the operating conditions:

$$k = \frac{(v_2 - v_1)}{\delta t} \frac{1}{(V_\infty - v_1)} \tag{4.2}$$

where v_1 and v_2 is the volatile yield at the previous - and current particle temperature, respectively, for the current time step, δt. The two yields are calculated by accessing the ANN with the heating rate of the particle. Figure 4.1 shows the structure of the hybrid model and interface with the CFD code.

The minimum inputs to the hybrid submodel is thus current particle temperature, time step size and particle temperature at previous time step. The desired output is the total volatiles released during the time step in order to calculate a rate of devolatilisation. These inputs and output are the interfaces with the CFD source code. In order to specify the input-output data pairs for the ANN training, an understanding of the physics is required. The total volatiles released is a function of temperature and heating rate as can be seen in Figure 4.2. Therefore, a hyper plane can be created with these three variables. The inputs to the ANN is thus particle temperature and heating rate and the output is total volatile yield. This hyper plane is accessed twice per time step in order to calculate the gradient of volatile yield with temperature for a specific heating rate. For a varying heating rate, the following is obtained by combining Equation (4.1) and (4.2) for the volatile rate:

$$\frac{dV}{dt} = \frac{(v_2 - v_1)}{\delta t} \frac{(V_\infty - V)}{(V_\infty - v_1)} \tag{4.3}$$

For a constant heating rate $V = v_1$ and the second term on the right-hand side of Equation (4.3) becomes one. As V approaches V_∞, Equation (4.3) approaches zero.

The same calculation was utilised during cooling by using a positive value for the temperature gradient. The limits of the model was determined by investigating

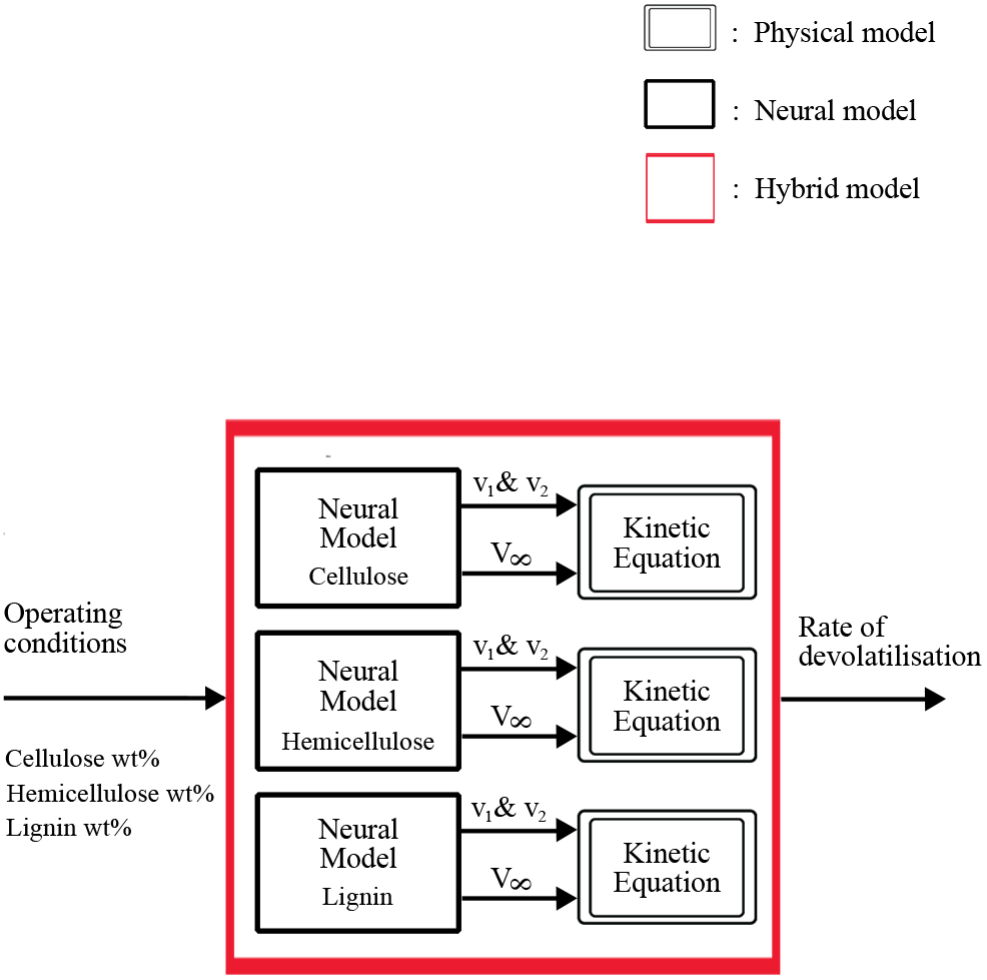

Figure 4.1: Hybrid model and CFD interface

the physics. The Bio-CPD model considers biomass as three main components, namely cellulose, hemicellulose and lignin. The same methodology was followed for each component and the results tracked for every particle. The total volatile release was calculated as the mass-weighted average of the constituents. MATLAB® version 2017A code of the constant heating rate CPD model was received from BYU. This model was used as a simulator to generate data for the ANN training. The upper and lower limits of temperature and volatile yield was determined by using the MATLAB® code with the upper and lower limits of heating rates. These values were chosen by inspecting the time temperature histories of different size particles in the boiler simulation. Values of 1 K/s and 25 000 K/s were used. The lower limit of temperature was chosen as 400 K and the upper limit varied around 1 000 K for the three components. The upper limit of volatile yield was higher for cellulose compared to hemicellulose and lignin.

The quality of the data is the most important aspect of a machine-learning exercise. There is a balance between using enough data points to capture the phenomena without over-fitting the model. Inaccuracies in the data can result in noise, which could also lead to over-training. Fortunately, the current study involves data generated by solving smooth ODEs and therefore contains no noise; however, the sufficient amount of data points had to be determined.

The amount of data points were varied by changing the resolution in heating rate values from the lower to upper limit. For each heating rate the data points from the lower to upper limit of temperature were chosen by the CPD code based on the time step required by the numerical method in order to ensure accuracy and stability. The choice of higher resolution over the temperature range can be explained by Figure 4.2 where it is clear that the largest gradients on the hyper plane exist in the direction of temperature, and by using the resolution of the numerical method, sharp gradients are captured with more data points. The data generation for the hyper plane is very simple and easy to visualise since only three variables are involved. A multi-dimensional data space is, however, very different and the use of random values is recommended by Laubscher (2017). It is good practice to choose the limits of the data space a bit wider than the range of the application due to the normal distribution of the random number generator.

4.2 Network architecture selection and training

Research indicates that two-layer networks with a log-sigmoid or hyperbolic tangent sigmoid function in the first layer and a linear function in the second layer (hidden layer) can capture virtually any trend. Single-layer networks have limited applications to simple functions [Hagan and Demuth (2014)]. Therefore, a two-layer network was chosen. The accuracy of the network for a combination of

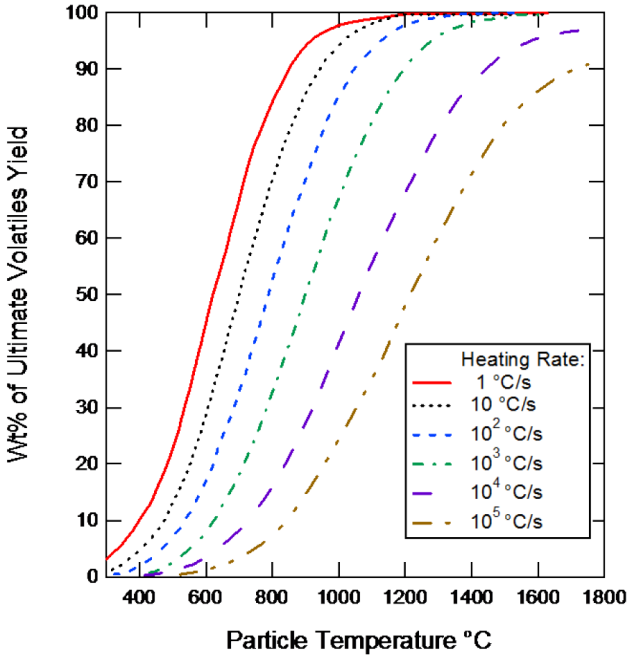

Figure 4.2: Effect of heating rate on weight loss at different temperatures [Lewis (2014)]

activation functions depends on the amount of neurons in the hidden layer. The optimum amount of neurons in the hidden layer can only be predicted for a few problems [Hagan and Demuth (2014)]; therefore, the network designer has to use trial and error to determine the architecture. The first step is to choose the best combination of activation functions for a reasonable amount of neurons. Of all the combinations, using a hyperbolic tangent sigmoid function in both layers delivered the best results in the current study. Comparing Figure 4.2 to 4.3, it can be seen why the hyperbolic tangent sigmoid function is better suited to approximate the devolatilisation characteristics with respect to temperature. LeCun *et al.* (1998) found that hyperbolic tangent sigmoid functions converged faster than log-sigmoid functions and have better non-linear capturing abilities. The remainder of the research utilises only hyperbolic tangent activation functions.

Laubscher (2017) found that by increasing the amount of neurons, the error decreased due to the added flexibility of the network to fit the data. When the number of hidden layers was increased beyond a certain amount, the error increased due to the optimisation routine used by Laubscher (2017), namely stochastic descent with momentum modification. In the current research, the Levenberg-Marquardt optimisation algorithm was used, which is less likely to get stuck in a local minima during optimisation of the network weights. This approach has the added benefit

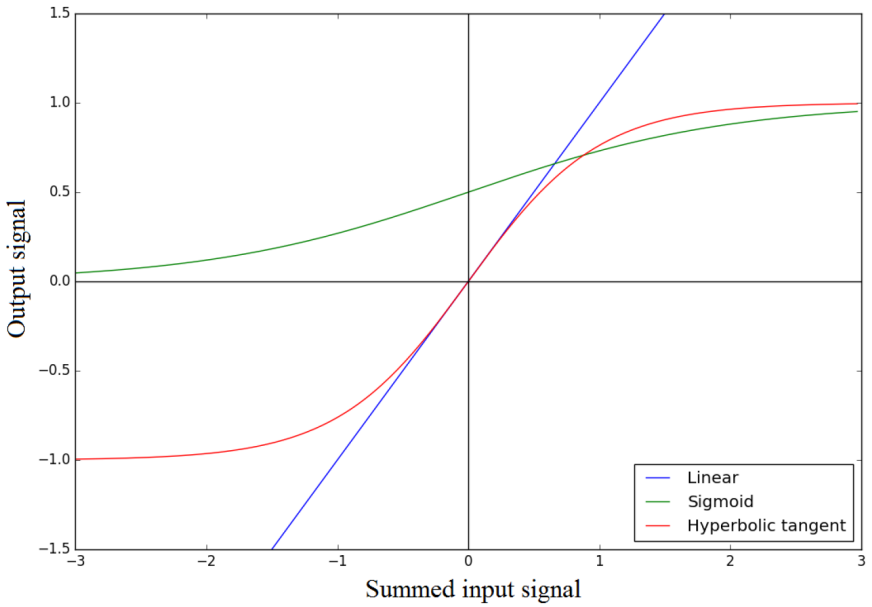

Figure 4.3: Different activation functions used in ANNs [Laubscher (2017)]

of switching to the Newton method to traverse a shallow plateau in the optimisation space quickly. However, increasing the amount of hidden layers was not tested due to the simplicity of the hyper-plane approximation.

The amount of hidden layers and neurons are determined by the sample size, the level of noise in the data and the target function complexity. The data set size was varied with the amount of neurons to find the optimum network architecture. A hidden layer with 10 neurons was chosen after studying the out-of-sample error graphs in Figure 4.4; this is comparable to the value of 7 neurons chosen by Laubscher (2017). It can be seen in Figure 4.4 of the MSE that the largest improvement in accuracy is achieved by increasing the amount of neurons up to 10. It is also evident that a higher level of accuracy can be obtained for lignin. When considering all three components, 30 neurons is the optimum value since the least amount of accuracy improvement is achieved with a higher value of neurons. The in-sample error also follows the out-of-sample error, confirming that the data set size is large enough. It is not shown since the curves are exact.

The average model error considering all three components is 0.6 % comparing well to the model error of Laubscher (2017), which is 2 to 3 % and Deidda *et al.* (2001), which is 4.6 %.

Figures 4.5, 4.6 and 4.7 describe the accuracy of the ANN training for cellulose, hemicellulose and lignin, respectively. It can be seen that most of the predictions fall within the 95 % confidence interval.

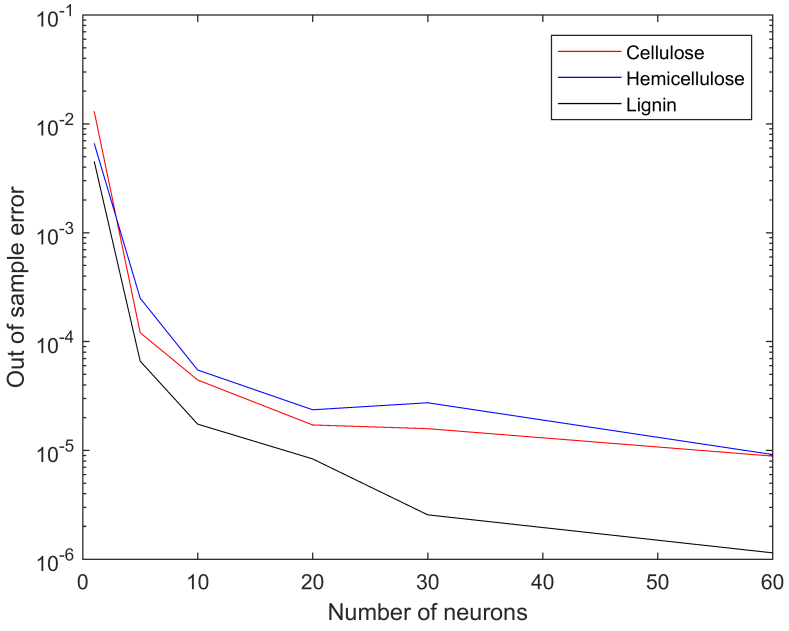

Figure 4.4: Out-of-sample error vs amount of neurons

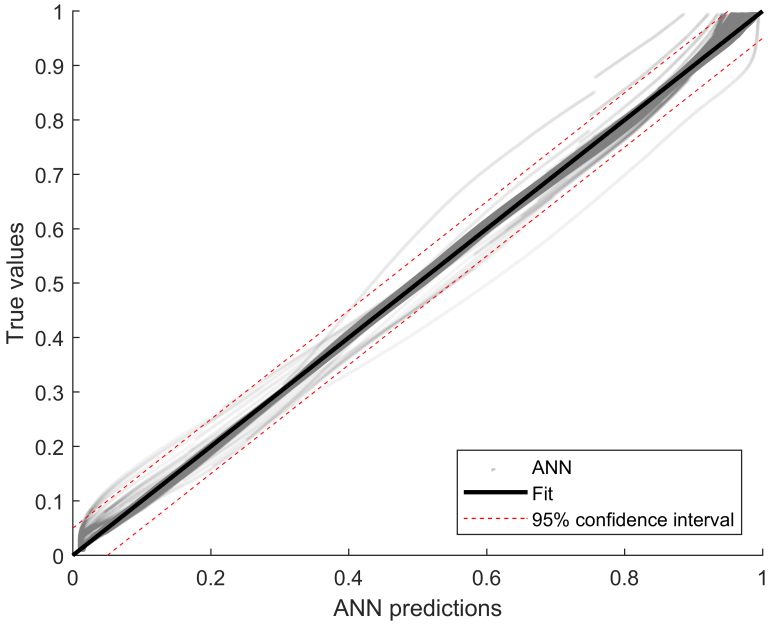

Figure 4.5: Prediction of ANN with 10 neurons for cellulose

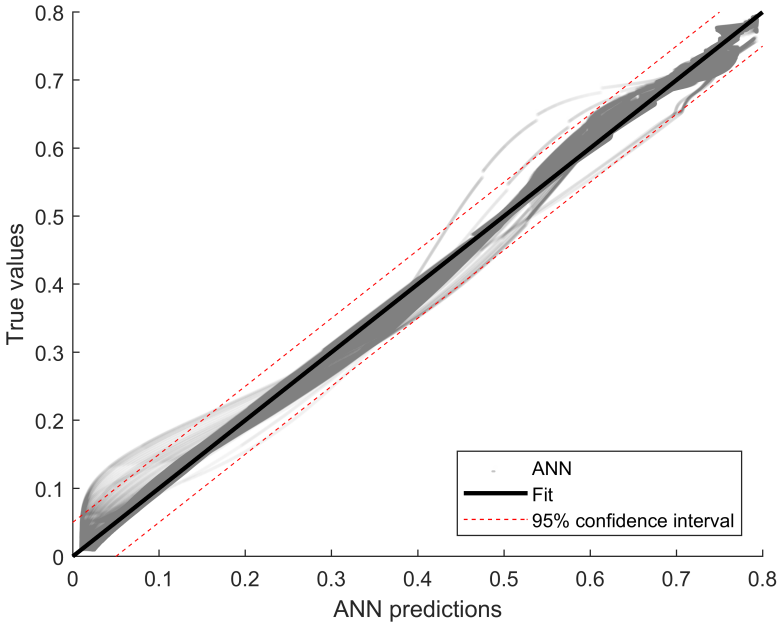

Figure 4.6: Prediction of ANN with 10 neurons for hemicellulose

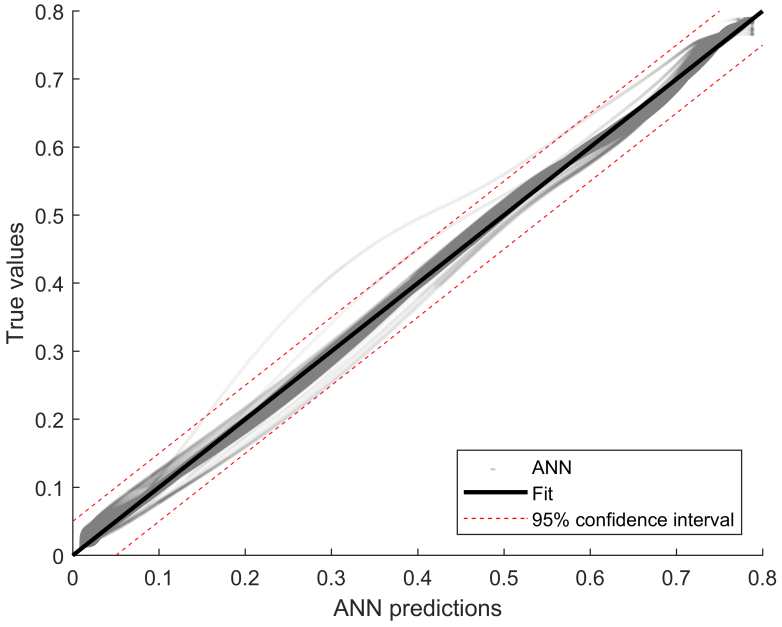

Figure 4.7: Prediction of ANN with 10 neurons for lignin

The accuracy of the network was improved by using 30 neurons. However, the largest reduction in MSE was achieved by partitioning the data space. It was found that using 12 ANNs of 30 neurons each per biomass component for the range of heating rates from 1 to 10 000 K/s, reduced the error to 0.3 % on average. A higher resolution was required from 1 to 1 000 K/s. Therefore, three networks were used in this range. Inspecting the data revealed sharper gradients compared to the rest of the data space.

Laubscher (2017) also partitioned the data space in order to improve the accuracy. However, since the amount of networks are increased, the computational effort increases. This extra computation is small when replacing time integration over a time scale by a single feedforward operation and the dramatic speed-up was shown by Laubscher (2017). However, when interfacing with the DPM module of ANSYS® Fluent per time step for each particle tracked, the extra computational effort is considerable. A single network of 10 neurons for each of the components, namely cellulose, hemicellulose and lignin, was therefore deemed an acceptable compromise and used in the remainder of the research. The resulting increase in computational time compared to the single-rate model for 1 DPM iteration was 20 %.

Data partitioning, more neurons and extra layers would be much more computationally efficient when an ANN is embedded into open-source software. It is believed that the computational expense in the present research is due to the limited hooks available with commercial software as the speed-up for one execution will be shown in the next section. This is exacerbated by the fact that the ANN has to be accessed twice per time step and for every particle.

4.3 Performance

The speed of the ANN compared to the CPD code was tested in MATLAB®. Different amounts of time steps were executed to generate data sets of pairs. These pairs were used as inputs to the ANN. Therefore, it is directly comparable to generate the same results for a constant heating rate. However, for a varying heating rate in the CFD model, the ANN has to be executed twice and thus the speed-up is halved. Bearing in mind that the Bio-CPD model requires the same calculation for each of the three components, the speed-up for the total model is 1.5 times the values in Figure 4.8. This equates to 450 times faster than the traditional ODE solver per time step with the largest data set tested. It can be seen in Figure 4.8 that the speed-up increases with increasing time steps and thus a much larger speed-up is achieved in an industrial simulation with 54 thousand particles and approximately 700 million time steps.

The use of the ANN is also advantageous for time steps where the CPD model

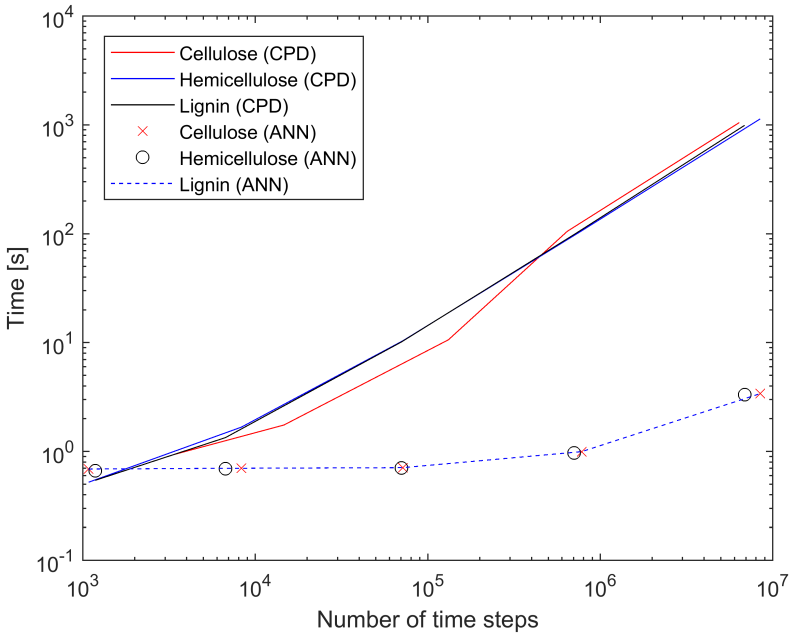

Figure 4.8: Solving time vs amount of time steps

requires a finer discretisation for numerical stability and accuracy compared to the other ODEs of the DPM solved. This benefit is in addition to the speed-up with direct comparison of one time step.

The speed-up will become more apparent when thermally thick particles or a more advanced devolatilisation model, such as CHL, is used. Since it can be concluded that the true benefit of using an ANN approach in-stead of a traditional ODE solver, from a computational-effort perspective, lies in the speed-up increase with increased complexity and operations.

4.4 Reactor model

The next step of the hybrid model development was to replicate the MATLAB® CPD code. The MATLAB® code applies a constant heating rate to a particle and predicts the resulting total volatile yield. Provision was made to change the heating rate once during the process. Therefore, the inputs are: heating rate 1, temperature 1, heating rate 2 and temperature 2. The same functionality was coded accessing the ANN twice per time step and using Equation (4.1) to calculate the change in yield instead of solving the ODEs of the CPD model. Therefore, the code comprises two sections: the feedforward propagation of the ANN algorithm

and the time stepping with varying heating rate.

The benefits of this approach was the following:

- The functionality of the code could be debugged and tested without interfacing with ANSYS® Fluent.
- The effect of the MSE on the ANN volatile prediction could be visually inspected by comparing the results to the CPD model. Refer to Appendix A for the graphical representation. Minor discrepancies were seen.
- The ability of the hybrid model to capture a varying heating rate could be confirmed.
- A combined Bio-CPD formulation of cellulose, hemicellulose and lignin could be tested.

4.5 CFD Implementation

This section explains the procedure followed during the execution of the hybrid model and the interface with the ANSYS® Fluent source code.

The DEFINE_DPM_SCALAR_UPDATE macro is used since extra DPM variables are required to be stored and updated with every DPM time step.These variables are as follows:

- Devolatilisation rate
- Particle temperature
- Total yield of cellulose, hemicellulose and lignin

The devolatilisation rate at the end of the previous time step is required to prevent a zero rate when the particle temperature remains the same during a time step. In this case, it has to revert back to the previous rate. When the routine is parallelised and a particle crosses the boundary of a partition, a check is also required to prevent running the routine when the time step size is zero during part of the crossing.

The particle temperature at the end of the previous time step is required to calculate the heating rate. The yields of the individual biomass components are required in order to track and calculate the total yield as a mass fraction of these parts. The following steps are executed sequentially:

1. The variables mentioned above are initialised.

2. The same procedure is followed for the three components of the biomass. The ANN feedforward propagation is done twice in order to calculate the gradient of volatile yield with regard to the current temperature change and heating rate. The gradient is normalised with the amount of volatiles remaining in the particle at the specific point on the ANN hyper-plane database. This kinetic rate is used in the single-rate formulation based on the amount of volatiles of the specific component left in the particle to calculate the change in volatile yield.

3. The total change in yield is calculated based on the fractions of the individual components. Various limits are imposed to ensure the ANN only interpolates within the trained data space and the rates are only positive in case of statistical noise or negative gradients of the fitted activation functions.

4. The variables mentioned in step 1 are updated for the next time step.

5. The rate is passed to the DEFINE_PR_RATE macro. The implementation is described in Appendix B. This macro was used instead of DEFINE_CUSTOM_LAW due to the fact that it allows particle surface reactions to be specified. This has the benefit of releasing multiple species from the particle surface, which is required for detailed chemistry. Applying a pseudo gas-phase step to break the pseudo volatile species into different chemical species at a very high kinetic rate was found to cause an unrealistic delay in volatile release. Multiple particle surface reactions are also required for releasing different quantities of tar and nitrogen from different particles based on Bio-CPD. It is out of the scope of the current body of work, but recommended for the implementation of detailed chemistry of NO_x. It is also required for the gas-phase reactions of sulphur, chlorine, potassium and sodium when considering fouling in boilers.

A DPM iteration is performed every 30 homogeneous phase iterations. Steady particle streams are tracked over time through the domain. As the particle is tracked through the grid, mass, energy and momentum exchange takes place with the fluid. During a DPM iteration, the DEFINE_DPM_SCALAR_UPDATE and DEFINE_PR_RATE macros loop over all the particles for a single time step. Since steady DPM is used in the final application of the research, a set number of time steps is specified in order to ensure that mass transfer from the DPM to the continuous phase is complete. Therefore, steps 1 to 5 are repeated for the amount of particles multiplied by the amount of time steps chosen. It is therefore computationally expensive and an additional check was built in to only execute the algorithm during devolatilisation. The most basic ANN was also used with no partitioning of the data space in order to reduce the computational effort.

The major difference between this research and the CFD ANN implementation of Laubscher (2017) is now apparent. In this study, the ANN is used during time integration at every step. Laubscher (2017) replaced time integration with a single ANN feed forward operation since only the final value is required for the EDC. It is, however, similar to the model developed by Deidda *et al.* (2001) where a kinetic rate is passed from the ANN to the CFD source code.

Chapter 5

Validation of reduced-order model

The implementation of the EDC on a CFD simulation of a bagasse-fired boiler is the goal of this body of work. The success of this implementation depends on the accuracy of various submodels. The present study focused on devolatilisation and the development of a reduced-order Bio-CPD model was discussed in the previous section, ANN-Bio-CPD.

The next few sections deal with the validation of ANN-Bio-CPD. The reactor model is used to simulate wire-mesh experiments and the CFD implementation is applied to drop-tube tests of inert devolatilisation and combustion.

5.1 Devolatilisation reactor model

This section discusses the validation of ANN-Bio-CPD for bagasse devolatilisation at constant heating rates. Heating rates of 1 K/s and 1 000 K/s were investigated by modelling widely published experiments of Stubington and Aiman (1994) and Drummond and Drummond (1996). The chosen rates are typical extreme cases in bagasse-fired boilers.

The mass fractions used for cellulose, hemicellulose and lignin in the reactor model were 0.508, 0.282 and 0.21, respectively, from Drummond and Drummond (1996) and Sheng and Azevedo (2002).

5.1.1 Description of experimental set-up and procedure

Stubington and Aiman (1994) and Drummond and Drummond (1996) both used a wire-mesh reactor to determine the pyrolysis yields of bagasse. The components of the wire-mesh reactor is shown in Figure 5.1. The 168 mm base of the reactor (a) is made from stainless steel. Two brass electrodes (b) with cooling water (c) support the wire-mesh (d). A Pyrex glass bell jar (e) covers the mesh and is pulled down

by an aluminium clamping ring (f). The inlet for the carrier gas is one side port (g) and the other side port (h) is used for purging. The trap for the tar collection (j) is attached to the screw port (i). The trap is cylindrical with a diameter of 32 mm and length of 140 mm. It also contains a sinter disk (k).

Bagasse was ground and sieved in the size range 70 to 150 μm. These particles were dried in an oven flushed with nitrogen. Approximately 7 mg of dried sample was placed in the central area of an opened mesh. Care was taken to remove particles smaller than the mesh size and to evenly distribute the sample as a mono layer. Due to the small sample size, emphasis was placed on positioning two pairs of thermocouples at representative locations in the mesh and their readings were averaged to obtain the temperature-time history of the sample. The temperature difference was also limited to a range and tests outside this range were rejected. The sample was raised at a constant heating rate to a peak temperature, held at the temperature and allowed to cool.

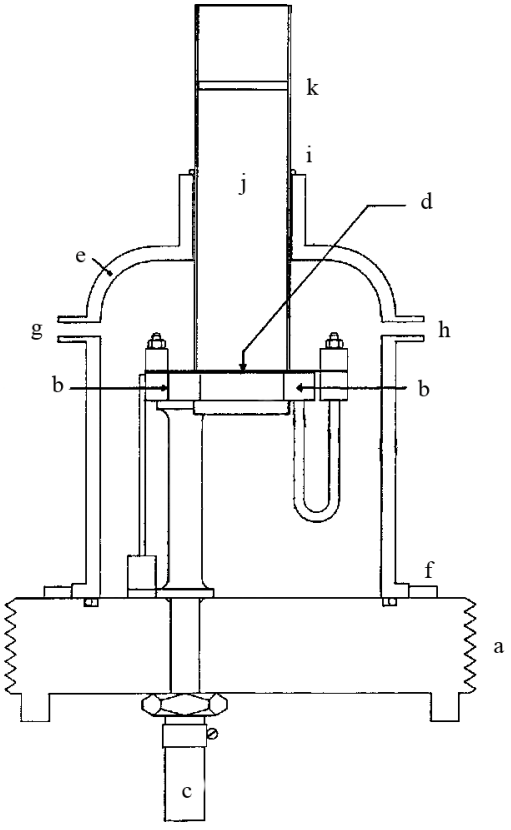

Figure 5.1: Wire-mesh reactor [Drummond and Drummond (1996)]

5.1.2 Results

The temperature of the sample was directly measured during the experimental procedure and the particles were thermally thin. The heating rate was controlled at a constant value and cooling happened naturally. The experiment was modelled accordingly at a constant heating and cooling ramp.

The ANN-Bio-CPD model predictions and experimental data are presented in Figure 5.2. It can be seen that ANN-Bio-CPD corresponds reasonably well to the data of Stubington and Aiman (1994) and Drummond and Drummond (1996) at a heating rate of 1 000 K/s. The data at the lower heating rate of 1 K/s also correlates reasonably well, except at the data point corresponding to the lowest temperature. For this reason, a value interpolated by Drummond and Drummond (1996) was used as the next data point in the direction of increasing temperature. This value is based on experimental data at a hold time of 30 s where all the data in Figure 5.2 is for a hold time of 0 s. The lack of data in this region of the graph is due to the very steep gradient. It is therefore very difficult to measure accurately at 0 s hold time.

Compared to the experimental data, the largest discrepancy is for 1 K/s heating rate where ANN-Bio-CPD predicts an earlier volatile release at 520 K compared to the measured value at 574 K. The effect of heating rate and trend is captured well when compared to Figure 4.2.

A qualitative deficiency of the model is seen for the maximum volatile yield. The maximum yield does not increase with increasing heating rate as seen in the experimental data and widely published [Lewis (2014)]. The value of maximum yield at 1 000 K/s is thus under-predicted. These same deficiencies of Bio-CPD were found by Rabacal *et al.* (2014) for sawdust and Beech wood in a DTF at high heating conditions.

An encouraging qualitative characteristic noted is the change in slope of the curve for the model predictions at 20 % yield. Rabacal *et al.* (2014) noticed the same trend. It corresponds to the release of hemicellulose and is typically seen in TGA experiments.

It can be concluded from the simulation that ANN-Bio-CPD can qualitatively capture the effect of heating rate on bagasse devolatilisation with a slight-under prediction in maximum volatile yield of 5 %. The quantitative values of the lower and higher heating rates also correspond reasonably well to the experimental data. The higher heating rate predictions fall within the two data sets.

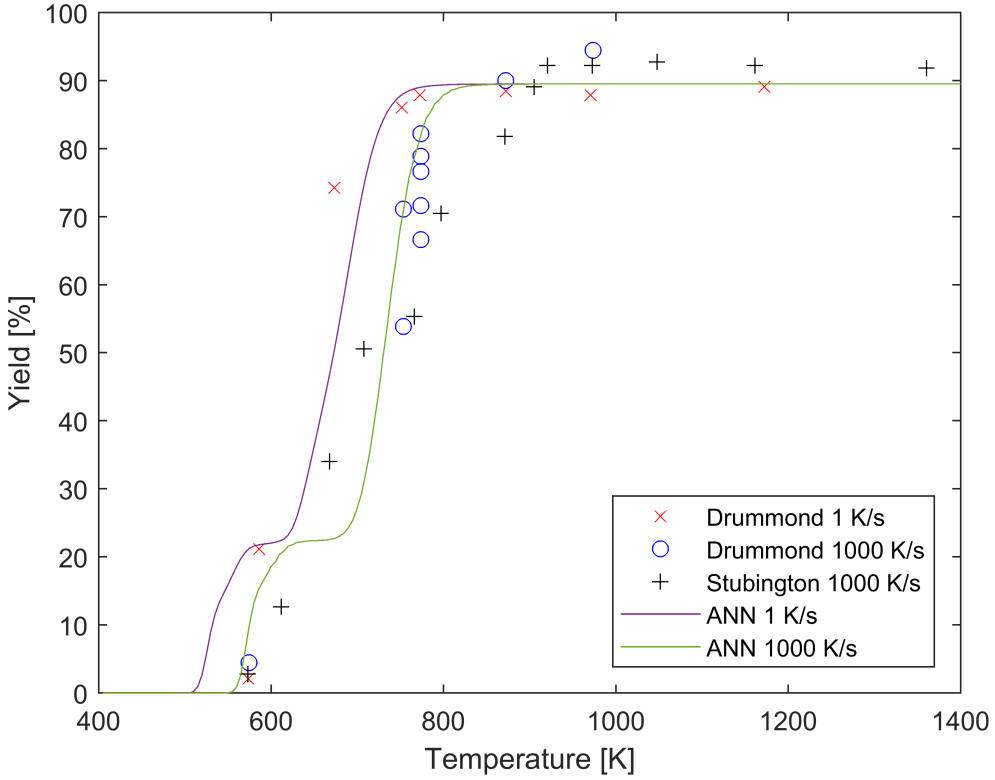

Figure 5.2: ANN vs experimental results

5.2 Devolatilisation CFD simulation

The previous section confirmed that ANN-Bio-CPD can be utilised for bagasse devolatilisation at a constant heating rate in a transient simulation. However, the focus of this study is industrial CFD combustion modelling. Therefore, the following section validates the implementation of ANN-Bio-CPD in the commercial CFD code ANSYS® Fluent.

Laboratory-scale experiments were modelled due to the low computational effort and controlled environment. Besides the reduction in temporal and spatial scales in a laboratory environment compared to an industrial application, parts of the combustion process, e.g. devolatilisation can be isolated. Other effects, such as turbulence and inter-particle effects, can be eliminated. Bands of the particle temperature and residence time spectrum can also be investigated in isolation by varying heating rate and temperature.

In this section, inert devolatilisation is modelled and the CFD implementation

with varying heating rate is confirmed.

The devolatilisation experiments of Wagenaar *et al.* (1993) were modelled by Lewis and Fletcher (2013). These experiments are ideal to validate the performance of ANN-Bio-CPD since it involves a DTF with interaction between flow and biomass particles that can be modelled with CFD. The varying particle heating rate in the DTF can also validate the single-rate approach of the hybrid ANN model. The temperatures and heating rates involved in the experiments correspond well to the conditions in a bagasse-fired boiler. The added benefit of choosing this experiment is the Bio-CPD model results of Lewis and Fletcher (2013), which could be compared.

5.2.1 Description of experimental set up and procedure

The DTF used by Wagenaar *et al.* (1993) consisted of a vertical tube with an inner diameter of 20 mm. This stainless steel tube could be varied in length from 0.3 to 1.2 m. Figure 5.3 shows the main components of the rig, namely reactor (1), sample probe (2), biomass feeder (3), oxidiser heater (4) and injector (5).

Pine sawdust was hammer-milled and screened in the size range 100 to 212 μm particle diameters. However, micro-photographs revealed a cylindrical particle shape with average diameter of 90 μm and average length of 320 μm. The sawdust was dried prior to the experiments.

The sawdust entered the reactor through a water-cooled feeding device. The carrier and secondary gas were inert nitrogen. The particles were transported to the exit of the tube where the gas was mixed with cold equimolar nitrogen flow to achieve a rapid quench of the products. The unconverted solids were collected in a pot positioned below the DTF. The difference in weight between the sample and solid product was used to determine the conversion.

5.2.2 Geometry

The geometry was modelled as a three-dimensional domain as shown in Figure 5.4. The dimensions of the furnace is given in Table 5.1.

Table 5.1: DTF dimensions

Inner diameter of furnace	20 mm
Diameter of carrier gas inlet	7 mm
Length of furnace	406.4 mm

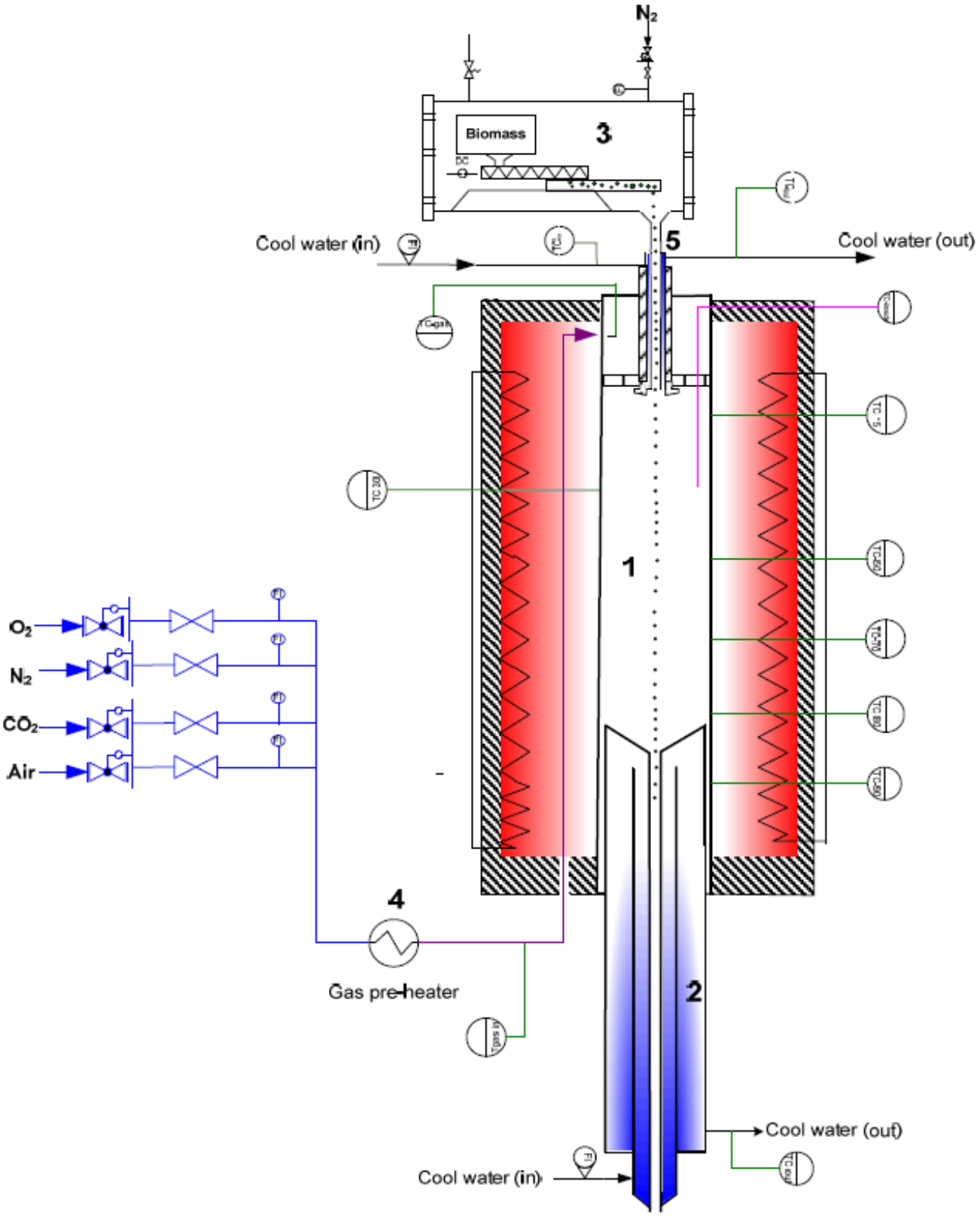

Figure 5.3: Diagram of DTF [Bramer (2017)]

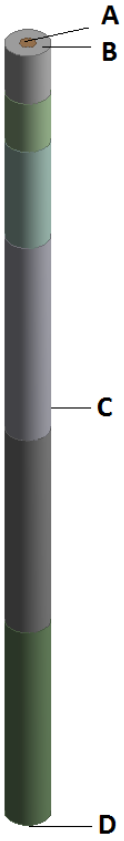

Figure 5.4: Three-dimensional computational domain of DTF

5.2.3 Boundary conditions

The boundary conditions used for the homogeneous phase is given in Table 5.2. The temperature of the walls of the DTF is set equal to the secondary gas temperature, as the heating elements are used to heat both the walls and the gas.

5.2.4 DPM properties

Since the simulation involves particles, the DPM was used. Important parameters with respect to the solid particle phase is given in Table 5.3. A 150 μm particle was used, which is the equivalent spherical diameter for the same volume as the average cylindrical shape. The mass fractions used for cellulose, hemicellulose and lignin were 0.427, 0.29 and 0.283, respectively, from Lewis and Fletcher (2013).

Table 5.2: Boundary conditions

Boundary condition name	**Boundary condition type**	**Assigned values**
Carrier gas inlet (A)	Velocity inlet	Velocity magnitude = 0.011 m/s Temperature = 300 K
Secondary gas inlet (B)	Velocity inlet	Velocity magnitude = 0.577 m/s Temperature = 773, 823, 873 K
Furnace wall (C)	Wall	Temperature = 773, 823, 873 K
Outlet (D)	Pressure outlet	Backflow temperature = 300 K

Table 5.3: DPM properties

Property type	**Assigned values**
Injection	Flow rate = 1.27×10^{-6} kg/s Temperature = 300 K Diameter = 150 μm Shape factor = 0.9
Material	Density = 425 kg/m^3 Specific heat as a function of temperature J/kg.K Swelling coefficient = 0.56 Volatile fraction = 0.8786 Carbon fraction = 0.1214

5.2.5 Multiphase flow simulation setup

The theory section discusses the following models utilised. Similar models were used by Du Toit (2015).

The flow in the reactor is laminar and was solved accordingly.

The species transport model was used to account for the interaction of species with the flow and chemical reactions. No turbulence-chemistry interaction was solved; only laminar finite-rate kinetics was utilised, although no homogeneous phase reactions were applied.

The Discrete Ordinates (DO) model was applied to account for radiation as formulated in ANSYS (2016).

The DPM was used for the solid particle phase. Particle surface reactions were utilised with the multiple surface reactions combustion model in order to

release the volatiles, as described in ANSYS (2016). This approach is required in order to implement ANN-Bio-CPD with the DEFINE_PR_RATE macro. Particle radiation interaction was also accounted for.

The density of the gas mixture was calculated using the ideal gas law. The kinetic theory of gasses was used for conductivity and viscosity. The specific heat, molecular weight, standard state enthalpy and standard state entropy were imported from the GRI 3.0 mechanism thermodynamic properties database with NASA polynomials.

The properties of the solid particles were based on average values from literature (Ragland and Aerts (1991)), (Lewis and Fletcher (2013)).

The steady state pressure-based solver was used with the SIMPLE algorithm for pressure-velocity coupling. The following spatial discretisation was used: least squared cell based for gradients, the standard scheme for pressure and the second-order upwind technique for momentum, k, ϵ, species and energy.

5.2.6 Mesh independence investigation

The mesh counts and amount of particles were incrementally increased in order to verify that the devolatilisation of the particle is independent of the mesh resolution and amount of particles.

The mass transfer to the fluid phase was recorded for the three reactor temperatures. These quantities were compared for each refinement stage. Table 5.4 shows the percentage change and cell counts. The corresponding amount of particles utilised are 35, 56 and 85 for the three grids from coarsest to finest. The table shows that the changes are very small confirming mesh and particle amount independence.

Table 5.4: Mesh refinement data

Mesh size	19 890	44 200	91 770
mass transfer, 773 K	-	0.033 %	0.292 %
mass transfer, 823 K	-	0.03 %	0.08 %
mass transfer, 873 K	-	0.093 %	0.065 %

In order to show that the model is grid-independent for the mesh size of 19 890, the discretisation error was calculated in accordance with Roache (1997) for the first refinement stage. In Table 5.5, the error on the coarse mesh is $E_{U,1}$ and the error on the fine mesh is $E_{U,2}$. The discretisation order was taken as 2 and the

refinement ratio as 2.22 for these calculations. The table indicates a very small error, showing grid independence.

Table 5.5: Discretisation error

Parameter	$E_{U,1}$	$E_{U,2}$
mass transfer, 773 K [kg/s]	-6.094×10^{-11}	-3.009×10^{-10}
mass transfer, 823 K [kg/s]	7.618×10^{-11}	3.762×10^{-10}
mass transfer, 873 K [kg/s]	2.539×10^{-10}	1.2539×10^{-9}

5.2.7 Results

The results of the CFD simulation are compared to the experimental data in Figure 5.5. The mass conversion is plotted against the residence time of the sawdust particles in the reactor for different reactor temperatures.

ANN-bio-CPD captures the trend of mass conversion with particle residence time well, especially at 773 K and 823 K. The model under-predicts the conversion at 873 K with the largest difference at residence times less than 0.15 s. This difference could be due to the fact that cooling was not considered in the current model. Wagenaar *et al.* (1993) mixed cold equimolar nitrogen flow with the nitrogen carrier gas in order to achieve a rapid thermal quench of the products within 40 ms. Very high cooling rates corresponding to this short time period improved the correlation of the model with the data. It was also found that the cooling rate had a larger impact on the higher temperature data where the largest discrepancy with the model is. However, the exact nature of the cooling process is unknown and therefore assumed as instantaneous for the presentation of the model results. The maximum yield is also under-predicted.

Comparing the Bio-CPD values of Lewis and Fletcher (2013) with the predictions of ANN-Bio-CPD, the ANN version consistently predicts a lower conversion, except from 0.3 s where the maximum yield correspond. ANN-Bio-CPD is, however, closer to the experimental data at 773 K and 823 K. The difference between the two models could be attributed to the fact that in the current research the CFD model of the DTF accounts for temperature gradients in the reactor, where Lewis and Fletcher (2013) used an isothermal gas temperature profile. The temperature profile of the CFD model is shown in Appendix C and indicates lower temperatures at the inlet of the reactor leading to lower conversion. The approach of Lewis and Fletcher (2013) with regard to particle cooling is also unknown and slower cooling rates increase the mass conversion correspondingly.

The discrepancy in maximum yield of both models could be due to the material losses in the collection system reported to be 10 % on average. Another explanation is that there is an effect of high heating rate on biomass volatile yields that is not fully captured by the Bio-CPD model as stated by Lewis (2011).

In conclusion, the ANN-Bio-CPD model captures the devolatilisation behaviour of Pine sawdust at high heating-rate conditions reasonably well. The qualitative trends of predicted mass conversion with varying heating rate in the temperature band from 773 K to 873 K compares well to the measurements. The quantitative values also correspond reasonably well, except for an under-prediction in maximum yield of 13 % as found with the bagasse wire-mesh reactor experiments. Therefore, the CFD implementation of ANN-Bio-CPD functions correctly for devolatilisation in an inert environment.

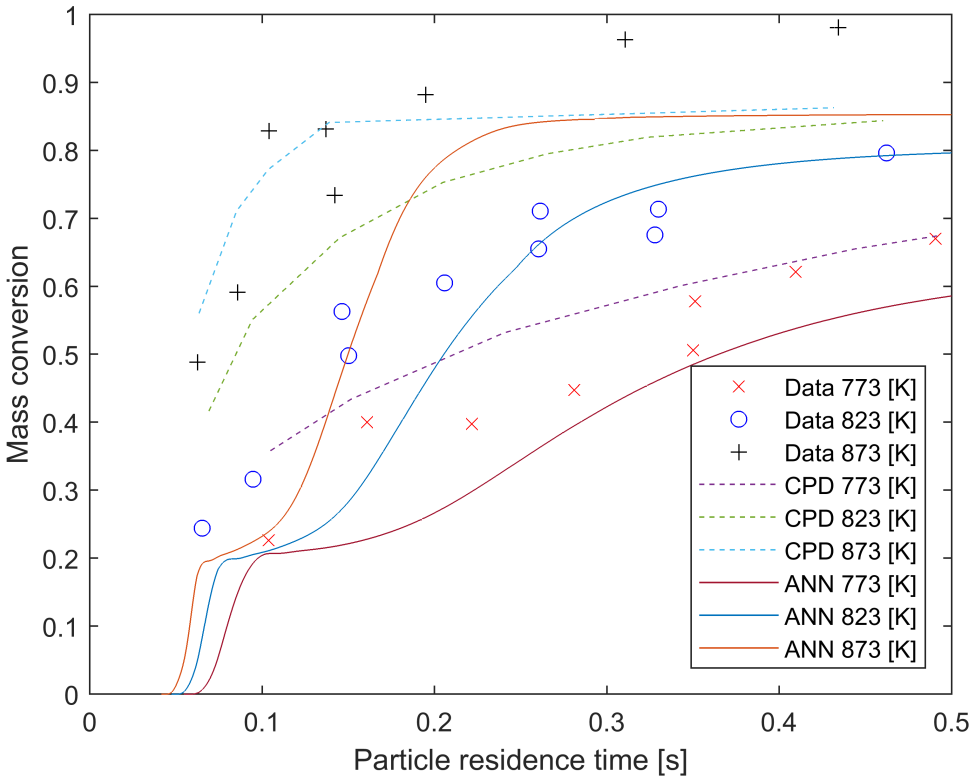

Figure 5.5: Mass conversion as a function of residence time

5.3 Combustion CFD simulation

In this section, the interface of ANN-Bio-CPD with the other heterogeneous processes, such as char combustion, is investigated.

Khatami and Levendis (2015) conducted combustion experiments with single bagasse particles in a DTF. The experiments were designed for boiler conditions. It has all the features of the devolatilisation tests in the previous section, with the addition of homogeneous and heterogeneous reactions. The purpose of the following section is to confirm that ANN-Bio-CPD is executed correctly in combination with a char combustion model. The CFD implementation of the model is also tested at higher heating rates and temperatures compared to the previous section. The added benefits of modelling these experiments are isolating the combustion phenomena from turbulence due to quiescent flow conditions and eliminating inter-particle effects since only a single particle is used. The char combustion model and release of multiple species from the particle surface, which is required for detailed chemistry, can also be validated.

5.3.1 Description of experimental set up and procedure

A DTF was used for the combustion experiments as shown in Figure 5.6. The furnace consisted of an alumina tube with an inner diameter of 70 mm. Molybdenum disilicide heating elements were used. The radiation zone was 250 mm long. A water-cooled injector was situated at the top of the DTF.

Bagasse was washed, dried, chopped in a household blender and sieved to 75 to 150 μm. Scanning electronic microscope images of individual particles revealed a cylindrical particle shape with an average aspect ratio of 10.

Single particles were introduced into the injector with a syringe needle. The furnace wall temperatures were continuously measured. Three observation ports, one at the top and two on the sides, provided optical access. An optical pyrometer and high-speed cinematography camera were used to study the burning of single bagasse particles from the top and sides of the reactor, respectively. The experiments were conducted under a quiescent gas condition by turning the gas flow off 10 s before injecting the particle. The axial profile of the gas temperature on the centerline of the furnace was measured with a thermocouple. The measured temperature stabilised at 1 340 K with a wall set point of 1 400 K. The composition of the gas in the furnace was that of air.

5.3.2 Geometry

The geometry was modelled as a three-dimensional domain as shown in Figure 5.7. The dimensions of the furnace are given in Table 5.6.

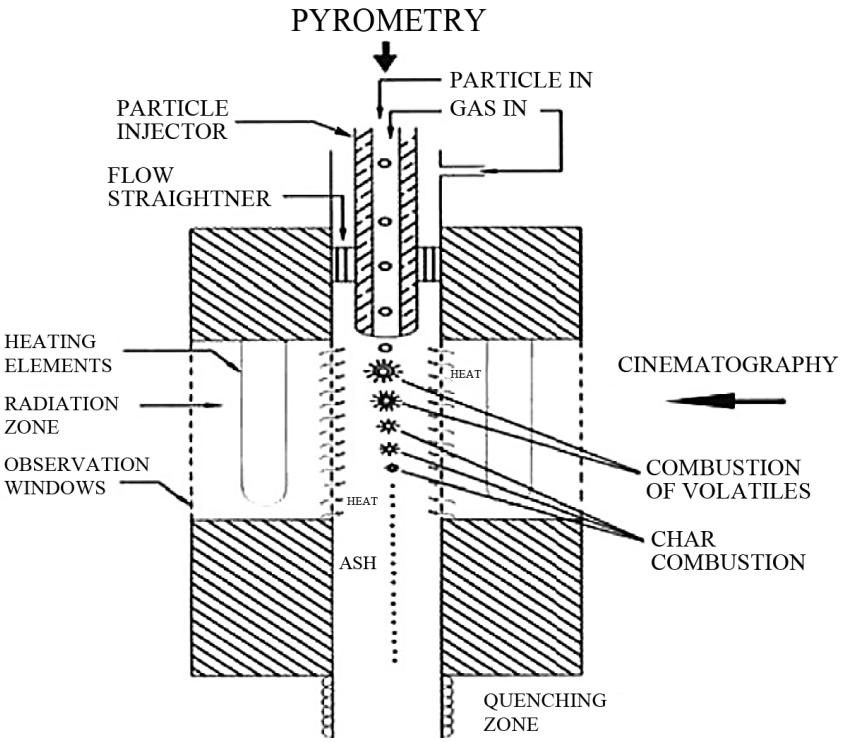

Figure 5.6: Schematic of the experimental setup [Riaza *et al.* (2014)]

Table 5.6: DTF dimensions

Inner diameter of furnace	70 mm
Diameter of carrier gas inlet	12.5 mm
Length of furnace	250 mm

5.3.3 Boundary conditions

Three different models corresponding to the experimental procedure were run, a steady state flow, transient flow and transient combustion simulation. The boundary conditions used for the homogeneous phase of the steady state simulation are given in Table 5.7. Both the transient flow and combustion simulation boundary conditions are given in Table 5.8.

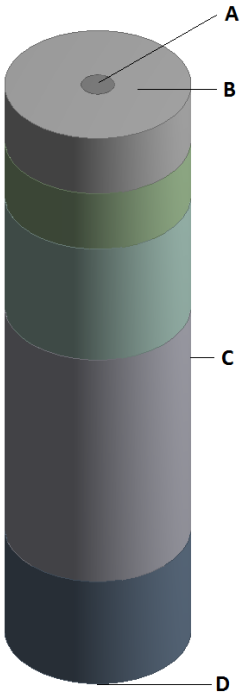

Figure 5.7: Three-dimensional computational domain of the DTF

Table 5.7: Boundary conditions of steady state flow

Boundary condition name	**Boundary condition type**	**Assigned values**
Carrier gas inlet (A)	Velocity inlet	Velocity magnitude = 0.02 m/s Temperature = 300 K
Secondary gas inlet (B)	Velocity inlet	Velocity magnitude = 0.02 m/s Temperature = 1 200 K
Furnace wall (C)	Wall	Temperature = 1 400 K
Outlet (D)	Pressure outlet	Backflow temperature = 300 K

5.3.4 DPM properties

Similar to the devolatilisation model discussed in the previous section, the DPM was used. Important parameters with respect to the solid particle phase are given in Table 5.9. The different values for the volatile- and carbon fraction are for ANN-bio-CPD and the two other devolatilisation models, respectively. The mass

Table 5.8: Boundary conditions of transient flow and combustion

Boundary condition name	**Boundary condition type**	**Assigned values**
Carrier gas inlet	Wall	Temperature = 1 200 K
Secondary gas inlet	Wall	Temperature = 1 200 K
Furnace wall	Wall	Temperature = 1 400 K
Outlet	Wall	Temperature = 300 K

fractions used for cellulose, hemicellulose and lignin were 0.508, 0.282 and 0.21, respectively, from Drummond and Drummond (1996) and Sheng and Azevedo (2002).

Table 5.9: DPM properties

Property type	**Assigned values**
Injection	Flow rate = 2.09×10^{-5} kg/s Temperature = 300 K Diameter = 200 μm Spherical
Material	Density = 500 kg/m^3 Specific heat as a function of temperature Swelling coefficient = 0.56 Volatile fraction = 0.8952, 0.9165 Carbon fraction = 0.1048, 0.0835
Devolatilisation	ANN UDF Single-rate model - Pre-Exponential factor = 3.12×10^6 s^{-1} Activation Energy =7.4×10^7 J/kgmol Constant-rate model - rate = 20 s^{-1} Vaporisation temperature = 400 K
Combustion	Diffusion limited - Binary diffusivity = unity Lewis number

5.3.5 Multiphase flow simulation setup

The theory section discusses the following models utilised. Similar models were utilised by Du Toit (2015).

Since the experiments were conducted under quiescent gas conditions with a single particle, a transient simulation was required. However, the initial conditions of this simulation had to be determined. A process involving three sequential simulations was followed, similar to the experimental steps:

- Steady state flow
  A steady state simulation was run with the same setup as the devolatilisation experiments in the previous section, but without the DPM. The necessary species for the GRI 3.0 chemical mechanism was solved, but no chemical reaction was required.

- Transient flow
  The velocity inlets of the steady state solution were changed to walls and a transient simulation of 10 s was run as per the experimental procedure.

- Transient combustion
  A bagasse particle was injected after the final time step of the transient flow simulation. An unsteady flow and DPM combustion simulation was run from ignition until extinction.

The setup of the simulation is the same as the devolatilisation case discussed in the previous section, except for the following.

The flow in the reactor is stagnant and was solved for laminar flow with chemical reactions.

The experiment involves ignition and extinction which requires detailed chemistry. A sensitivity analysis also revealed that the chemical mechanism used is important; therefore, the GRI 3.0 mechanism with 309 reactions and 50 species was utilised. This mechanism contains the maximum amount of species allowed in ANSYS® Fluent and is commonly used for biomass combustion. It is available in Chemkin format with ANSYS® Fluent. The species, Ar, C_3H_8 and C_3H_7, were removed from the Chemkin input file in order to stay within the 50-species limit. The gas composition released from the particle can be found in Appendix D.

The mass diffusivity of the gas mixture was also identified as an important parameter and kinetic theory was applied.

The diffusion limited combustion model of Baum and Street (1971) was utilised with unity Lewis number for the binary diffusivity. In the case with ANN-Bio-CPD, the combustion model was coded with the DEFINE_PR_RATE macro.

The single- and constant-rate devolatilisation models were compared to ANN-bio-CPD. A kinetic rate from Gera *et al.* (1999) was used for the single-rate devolatilisation model. A rate of $20\,s^{-1}$ with an initiation temperature of 400 K was applied for the constant-rate devolatilisation model from the ANSYS® Fluent data-base for wood.

The specific heat of the solid particles was identified as another important input and a correlation from Ragland and Aerts (1991) was used. A constant particle size of 200 μm was modelled. This value is the equivalent spherical diameter of a cylindrical particle volume. The cylinder diameter is the average diameter of the sieve size range, 75 to 90 μm. The length of the cylinder is based on an aspect ratio of 10. The aspect ratio was determined visually by inspecting bagasse particles and corresponds to the findings of Riaza *et al.* (2014). Although the particles are needle-like, Panahi *et al.* (2017) found that biomass particles experience intense shrinking, fusion and apparent spheroidisation during high heating-rate devolatilisation. Since the particles were dried before the experiment, the duration of the test is almost exclusively above the spheroidising temperature. A spherical shape factor was thus chosen to correspond to the spheroidising phenomena from ignition.

The first-order implicit transient formulation was applied with the fixed time-stepping method and a time step size of 1×10^{-4} s for the flow and the discrete phase.

5.3.6 Mesh independence investigation

The mesh counts were incrementally increased for the simulation with ANN-Bio-CPD in order to verify that the combustion of the particle is independent of the mesh resolution.

The duration of the volatile flame, duration of the char combustion and maximum particle temperature were compared for each refinement stage. Table 5.10 shows the percentage change and cell counts. The table shows that the changes are small considering the accuracy of the experiment, confirming mesh independence.

Table 5.10: Mesh refinement data

Mesh size	12 980	25 039	49 220
Volatile flame duration	-	7.075 %	-5.286 %
Char combustion duration	-	1.863 %	5.793 %
Maximum particle temperature	-	0.393 %	0.392 %

In order to show that the model is grid-independent for the mesh size of 12 980, the discretisation error was calculated in accordance with Roache (1997) for the first refinement stage. In Table 5.11 the error on the coarse mesh is $E_{U,1}$ and the error on the fine mesh is $E_{U,2}$. The discretisation order was taken as 2 and the refinement ratio as 1.93 for these calculations. The table indicates a small error, showing grid independence.

Table 5.11: Discretisation error

Parameter	$E_{U,1}$	$E_{U,2}$
Volatile flame duration [ms]	-0.551	-2.051
Char combustion duration [ms]	-0.22	-0.82
Maximum particle temperature [K]	-2.94	-10.94

5.3.7 Results

A comparison of the measured axial gas temperature profile with the CFD results at the start of the combustion simulation is given in Appendix D. The agreement of the CFD results with the experimental measurements is reasonable with a maximum deviation of 4.9 %. A bare thermocouple was used and corrected for radiation effects and therefore larger errors than the standard 1 % indicated is possible.

Burn-out times of volatiles and chars were taken from the cinematographic, Figure 5.8, and pyrometric observations, respectively. Char combustion temperatures were deduced from the pyrometric measurements.

The bagasse particles burned in two phases: volatile combustion in spherical nearly-transparent flames, followed by short shrinking-core char combustion. Ignition took place homogeneously at an estimated 700 K (±30 K). The delay to ignition was in the order of only 1 to 2 ms. Biomass volatiles generated low-luminosity low-soot content flames and since the radiative properties could not be detected pyrometrically, the temperatures were not recorded. The duration of the volatile flame was measured with high speed cinematography at 35 ms (±5 ms). The flame size was viewed from the top of the furnace as the particle fell. The bagasse flames were 300 μm diameter and perfectly spherical with an aspect ratio of one. The char combustion phase lasted 15 ms (±5 ms) with a peak temperature of 1 900 K (±70 K).

The CFD simulation also executed the devolatilisation and combustion phases sequentially as witnessed in the experiments. Two devolatilisation models are compared to ANN-Bio-CPD in Figure 5.9 and Figure 5.10. A sharp decrease in

particle mass corresponding to a sharp increase in CO_2 was considered as the ignition. The next point on the curve where the gradient changed substantially and the mass corresponded to the value of char and ash was considered as the end of the volatile flame and the start of char combustion. Char combustion ended when the mass remained constant at the value of ash in the particle. The peak of the temperature curve is the maximum char combustion temperature. Model results are compared to experimental data in Table 5.12.

The delay to ignition is longer than the experiments for both ANN-Bio-CPD and the single-rate model. This is due to the size of the particle. A size of 75 μm had a delay of 2 to 3 ms. This indicates that the intra-particle heat transfer is important in order to capture the correct delay to ignition for 200 μm particles. The constant-rate model starts to devolatilise at 400 K and, therefore, the delay to ignition is much lower close to the experiments.

The ignition temperature of both ANN-Bio-CPD and the single-rate model at 616 K is reasonably close to the lower range of the experimental value of 670 K, but closer to the upper range of values found by Grotkjaer *et al.* (2003) of 500 to 600 K. ANN-bio-CPD predicts a change in the mass loss rate corresponding to 20 % volatile yield. This effect is due to the more reactive hemicellulose and is not seen with the single-rate model. The constant-rate model ignition temperature is too low.

The volatile flame durations of ANN-Bio-CPD and the single-rate model are shorter than the experimental observations. The char burn time of both models are longer than the experimental data. The total burn time of both these models, however, compares well to measurements. The single-rate model correlates slightly better to the experimental data of volatile flame duration compared to ANN-Bio-CPD. The difference between the two models is the split between volatiles and char. Due to lack of data, the ASTM proximate volatile analysis value of 91.65 w % daf was used for the single-rate model and ANN-Bio-CPD predicted a value of 90 w % daf. Stubington and Aiman (1994) found that a value for the bagasse volatile yield of 2 % higher than the ASTM proximate analysis gave the best fit with the single-rate model. Lewis (2014) found that the maximum volatile yield exceeded the ASTM proximate value by $\approx$ 10 w % daf for the biomass tested at high heating conditions. Therefore, a higher volatile content than the ASTM proximate value is recommended and would bring both models closer to the individual experimental durations of volatile and char flames. Since the same ASTM proximate analysis volatile char split was used for the constant-rate model, the duration of char combustion is similar; however, the volatile flame is twice as long as the single-rate model. The total burn time is thus over-predicted by the constant-rate model.

A kinetic rate recommended by Stubington and Aiman (1994) for the single-

rate model delivered a volatile flame duration that is three times the experimental value and a delay to ignition that is twice the duration of the results with the rate of Gera *et al.* (1999). Another kinetic rate from Drummond and Drummond (1996) produced a similar extended delay to ignition. These results can be seen in Appendix D. A constant rate of $12\,s^{-1}$ at an initiation temperature of 600 K as recommended for coal by ANSYS (2016) also produced a volatile flame duration that is too long. Therefore, these single-rate and constant-rate results were discarded. It does, however, indicate that care should be taken when using kinetic rates from wire-mesh experiments for combustion simulations at high heating rates. The rate of Gera *et al.* (1999) is based on the burnout data from the Sandia National Laboratories Multifuel Combustor of the Combustion and Environmental Engineering Facility at the Federal Energy Technology Center in Pittsburgh. The combustor is a pilot scale experimental setup. The rates of Stubington and Aiman (1994) and Drummond and Drummond (1996) were determined in wire-mesh reactors. It also shows that the constant-rate model requires calibration to experimental values by adjusting the rate constant and initiation temperature.

The peak char temperature of 2034 K on average predicted in the CFD simulations is slightly higher than the upper value of the experiments of 1970 K. This temperature and the reasonable durations of char combustion predicted confirms the validity of the diffusion limited char combustion model used.

In conclusion, ANN-Bio-CPD initiates ignition at the correct temperature and the total burn time corresponds to the experimental data. The delay to ignition is longer than the experiments and requires intra-particle gradients to be taken into account for higher accuracy. The split between volatile content and char content has an effect on volatile and char flame duration. Due to the under-prediction in maximum volatile yield, ANN-Bio-CPD predicts a slightly shorter volatile flame duration and longer char burn time compared to the experiments. The single-rate model compared better to the experimental value of volatile burn time, due to the larger volatile content used, but did not produce a higher reactivity of part of the particle as is the case with hemicellulose. The constant-rate model initiated ignition at too low a temperature and over-predicted the total burn time due to a resulting longer volatile flame duration. Therefore, ANN-Bio-CPD is the model of choice when considering realistic energy release due to the more reactive hemicellulose component. There is, however, room for improvement, considering maximum volatile yield.

The diffusion limited char combustion model predicts a burn time and peak temperature that correspond reasonably to experimental data. The peak temperature prediction is 3 % higher than the upper limit of the measurements. It is therefore a suitable simplistic model considering the small amount of char in biomass.

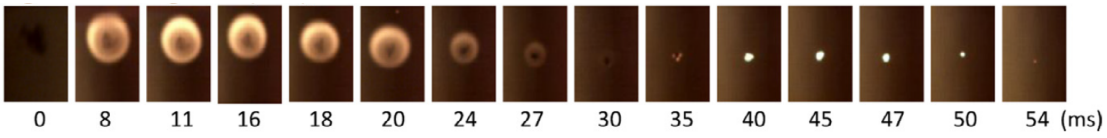

Figure 5.8: Bagasse cinematography [Khatami and Levendis (2015)]

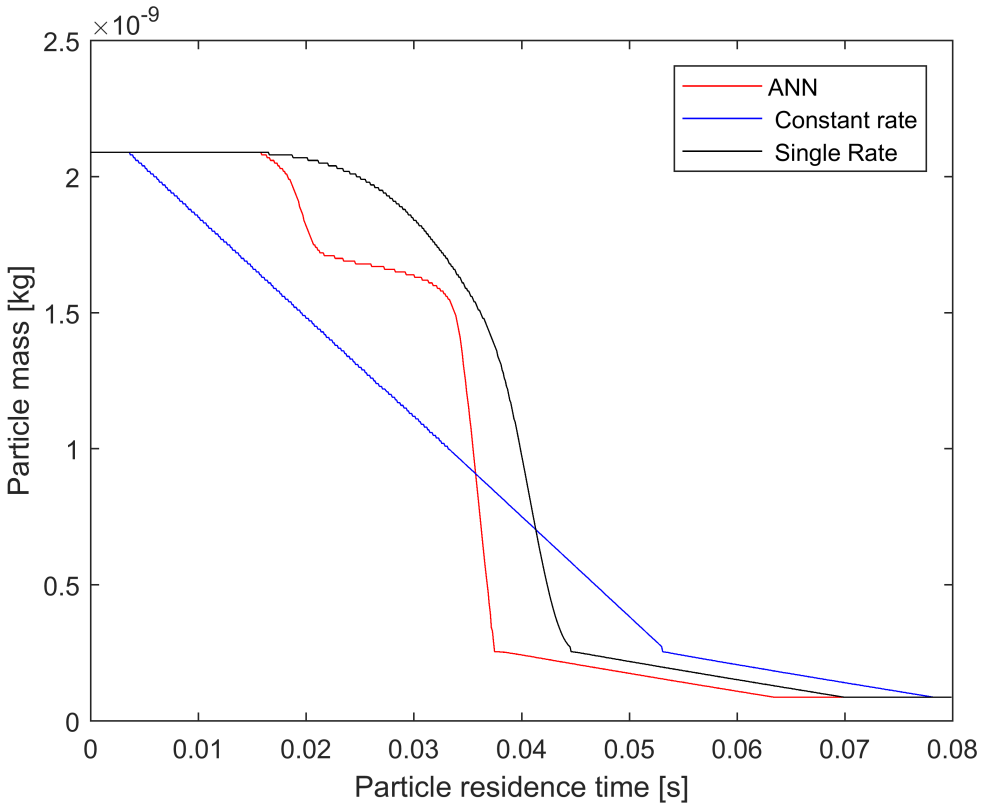

Figure 5.9: Particle mass as a function of residence time

Table 5.12: Combustion observations compared to model predictions

Phenomena	Experiment	ANN	Single rate	Constant rate
Delay to ignition [ms]	1-2	16	16	3
Ignition temperature [K]	700 ±30	616	616	400
Volatile matter burn time [ms]	35 ±5	21	29	50
Char burn time [ms]	15 ±5	32	25	25
Char peak temperature [K]	1 900 ±70	2 035	2 036	2 030

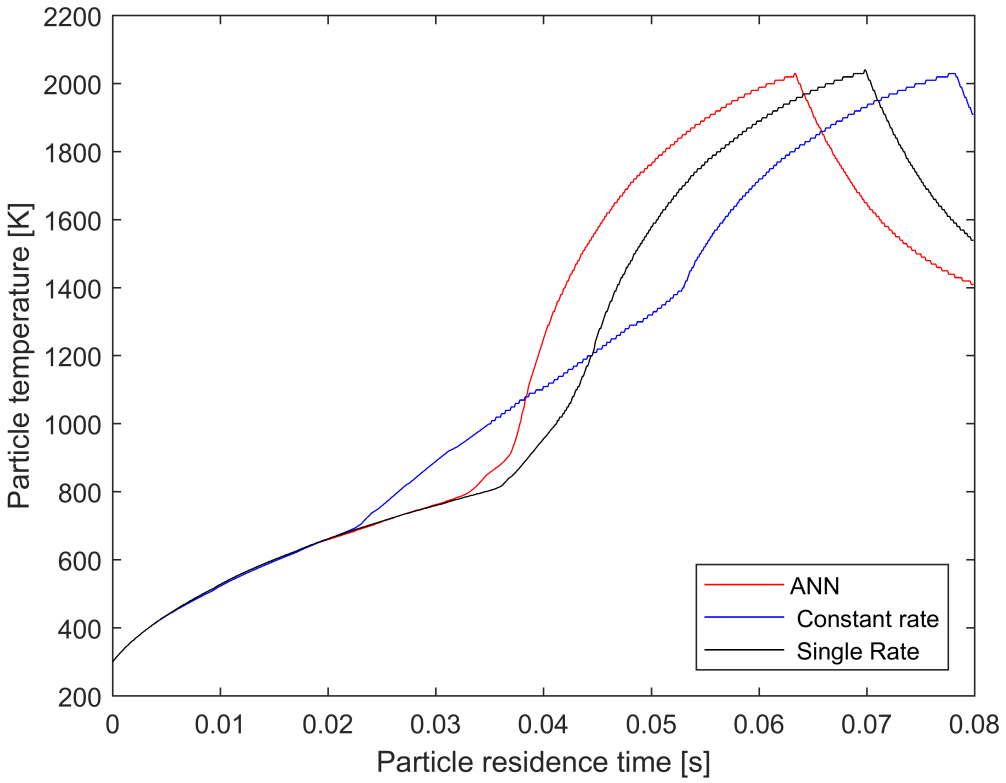

Figure 5.10: Particle temperature as a function of residence time

Chapter 6

Industrial CFD simulation

An industrial-scale solid fuel combustion simulation contains a wide spectrum of spatial and temporal scales. The range of temperatures, particle effects and chemical reactions are also wide, especially in a bagasse-fired boiler with a combination of fixed bed- and suspension burning. A CFD model of such a complex system involves numerous submodels, each contributing to the accuracy of the final goal, which in this case is predicting detailed chemistry in the future.

In the current study, the devolatilisation submodel was singled out and a methodical approach followed in the chapters leading up to this section in order to validate a custom code, namely ANN-Bio-CPD. In each section of the previous chapter, the level of complexity of the physics involved was increased up to single particle level in an environment as close as possible to that of the boiler furnace.

The final application of ANN-Bio-CPD is investigated in this chapter. Predictions from an upgraded version of the model developed by Du Toit (2015) are compared to measurements of Du Toit (2015).

6.1 Description of experimental setup and procedure

Du Toit (2015) conducted experiments on boiler no. 3 at RCL Komati sugar mill. This boiler is a typical example of a bagasse-fired design on an industrial scale, 25 MWe and medium pressure, 31 bar. It is 22 m high and 12 m wide.

Due to the complexity of the plant and the specific boiler terminology required in this body of work, the operation of the boiler is discussed next with reference to Figure 6.1.

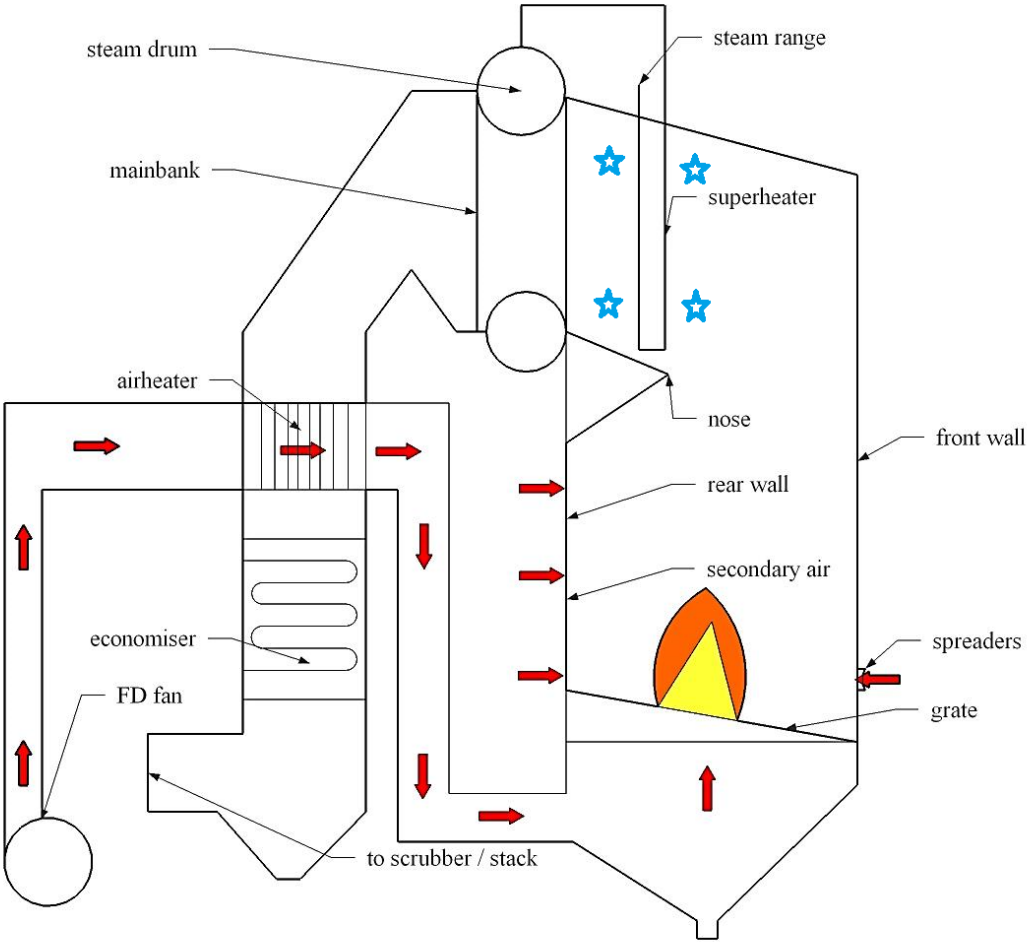

Figure 6.1: Diagram of boiler sectional side elevation [Du Toit (2015)]

The forced draught (FD) fan supplies the primary air to the grate via the air heater at 85 % of the total air flow. The remaining unheated fractions are 6 % spreader- and 9 % secondary air that is supplied with a separate high-pressure fan.

The bagasse is metered by feeders located above the pneumatic spreaders on the front wall. The spreading of the fuel is achieved by a jet of air over a flat metal plate. The particles are injected into the furnace when it falls on the spreader plate. Secondary air enters the furnace at high velocity through three rows positioned at different elevations on the rear wall.

Combustion takes place primarily below the nose of the furnace. The combustion gas flows upwards under a slight negative pressure due to the balanced

draught conditions maintained by the FD and induced draught (ID) fans. The gas flows through the superheater tube bank and across the mainbank, heating the steam and saturated steam water mixture, respectively. The combustion gas enters the air heater tubes to heat the air and flows over the finned economiser bank in order to heat the feed water. The energy in the gas at the exit of the economiser is considered a loss as no more heat is recovered on the way to the gas cleaning equipment, a wet scrubber in this case. The gas flows from the ID fan to the stack.

On the water-side, the feed water flows from the economiser to the drum. Natural circulation transports the water to the furnace walls and main bank riser tubes where it flows upwards back to the drum. Saturated steam flows from the steam drum to the superheater. The resulting superheated steam flows to the turbine via the outlet header and high-pressure piping.

The biomass specific boiler components are the air heater, static pinhole grate and refractory band around the furnace perimeter in the combustion zone. Fuel is spread to the rear of the grate and ash transported to the front hoppers with intermittent blowing of steam through rows of nozzles on the grate.

Bagasse was burnt exclusively during the experiments. The moisture content of the fuel was 47 % and the ash percentage 3.41 %. Since this mill utilises a diffuser to extract the sucrose, the size grading was slightly coarser compared to material from a milling train.

A suction pyrometer was used to measure gas temperatures across the width of the boiler. The same water-cooled titanium lance was also utilised to transport the products of combustion to a gas analyser. The composition of the flue gas was determined by means of chemical cells. The positions of the traverse measurements are indicated in Figure 6.1 with four blue stars. It is the position where SNCR will be applied to JT bagasse-fired boilers due to the temperature range of 1 123 to 1 243 K. A lower temperature would result in too slow $DENO_x$ reaction and at a higher temperature some of the injected NH_3 will burn and form additional NO_x. It is therefore a good location to measure gas species considering the motivation of this study, which is the prediction of pollutant emissions such as NO_x.

Thermal cameras were also utilised to obtain temperatures by means of optical pyrometry. The images of the camera also indicated the position of the flame, particle movement and combustion intensity.

Prior to the experiments, the spreaders were set at the correct angles and air pressures to achieve an even fuel bed on the grate. The secondary air pressures were adjusted as per the boiler's original equipment manufacturer (OEM) standards with the highest pressure at grate level.

The boiler was maintained at a constant load and air-fuel ratio. The load was manually set at the maximum continuous rating (MCR) of the plant. The

combination of steam flow, feed water flow, steam pressure and drum level was continuously monitored to anticipate upset conditions. The most important parameter monitored was the flue gas oxygen content at the main bank outlet by means of two Zirconian probes on the left- and right-hand sides of the boiler. This indicated correct fuel distribution and combustion stability in combination with the furnace pressure reading. Blockages of fuel-feeding equipment, piling of fuel on the grate, plugging of measuring equipment due to the high particle loading and process load swings were managed. A team of people conducted the experiments in order to obtain the best quality data in this difficult and aggressive testing environment far from laboratory conditions.

6.2 Geometry

The geometry was modelled as a three-dimensional domain, as shown in Figure 6.2. The image illustrates the decomposition of the volume in order to create a structured hexahedral mesh. Important geometrical parameters are given in Table 6.1. Only half of the boiler was modelled and a symmetry plane applied in the middle of the furnace. The validity of this approach considering the air supply system was confirmed by Du Toit (2015).

Table 6.1: Boiler dimensions

Height of domain	22 581 mm
Width of domain	4 787 mm
Grate level	6 600 mm
Depth of furnace	6 576 mm
Primary air inlet	3 282 x 900 mm
Spreader slots	600 x 10 mm
Secondary air slots	140 x 10 mm
Superheater tube size	63.5 mm OD
Superheater tube pitch (transverse x longitudinal)	200 x 127 mm OD
Superheater cavity (height x depth)	6 737 x 1 229 mm
Mainbank cavity (height x depth)	5 777 x 2 450 mm
Outlet duct depth	2144 mm

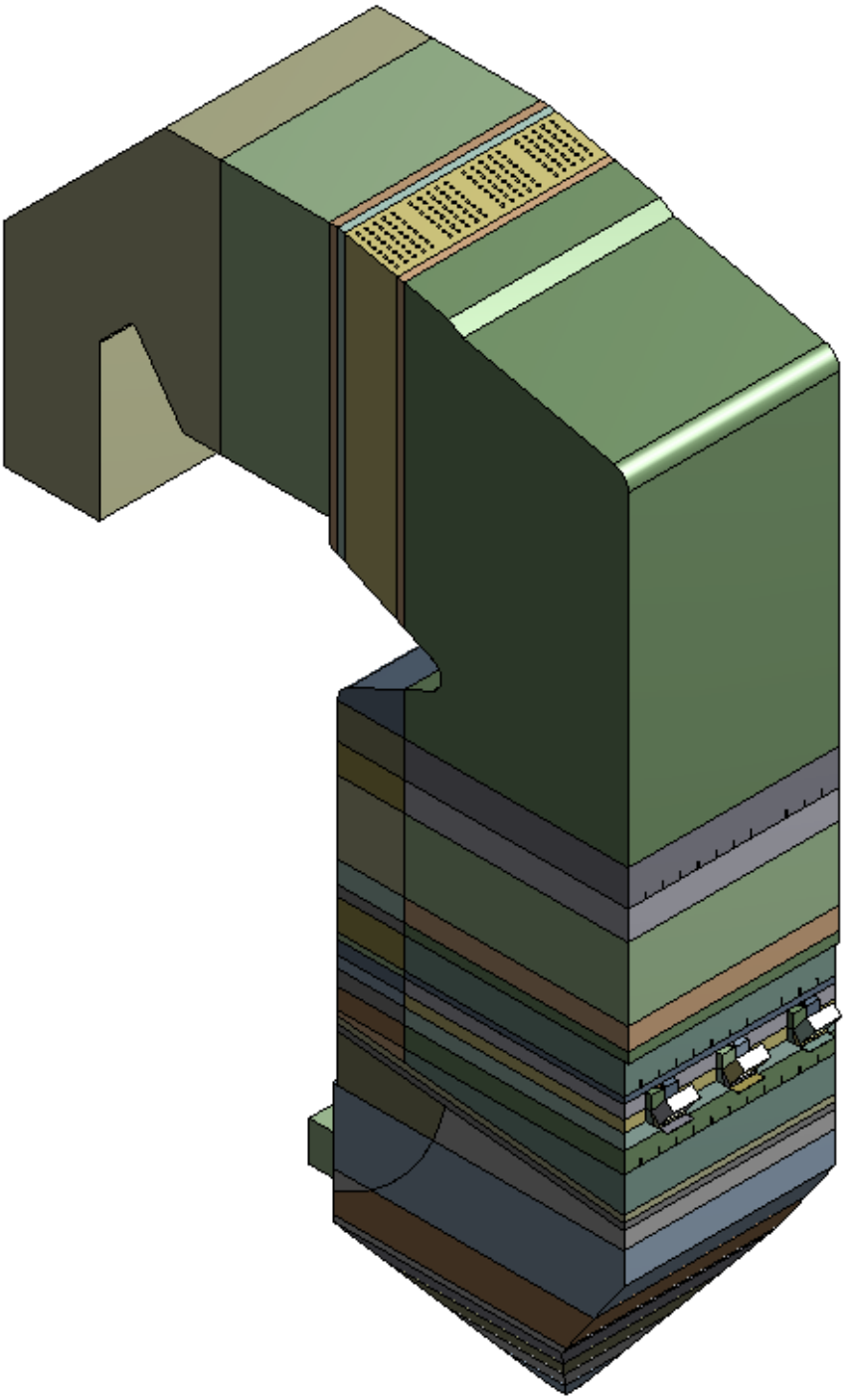

Figure 6.2: Three-dimensional computational domain of boiler

6.3 Boundary conditions

The important boundary conditions used for the homogeneous phase is given in Table 6.2. Du Toit (2015) modelled the steam in the superheater tubes, but in the current study only surface temperatures were applied. These temperatures were varied with tube row corresponding to the steam flow inlet- and outlet temperature.

Table 6.2: Boundary conditions

Boundary condition name	**Boundary condition type**	**Assigned values**
Primary air inlet	Velocity inlet	Velocity magnitude = 12.1 m/s Temperature = 462 K
Spreader air inlets	Velocity inlet	Velocity magnitude = 94.1 m/s Temperature = 309 K
Bottom secondary air inlets	Velocity inlet	Velocity magnitude = 71 m/s Temperature = 309 K
Middle secondary air inlets	Velocity inlet	Velocity magnitude = 60.3 m/s Temperature = 309 K
Top secondary air inlets	Velocity inlet	Velocity magnitude = 33.8 m/s Temperature = 309 K
Furnace tube walls	Wall	Material = Carbon steel Thickness = 0.00406 m Temperature = 518 K Emissivity = 0.95
Furnace refractory walls	Wall	Material = Refractory Thickness = 0.11 m Temperature = 518 K Emissivity = 0.4
Superheater tube walls	Wall	Material = Scale deposit Thickness = 0.00093 m Temperature = 518 to 667 K Emissivity = 0.6
Outlet	Pressure outlet	Backflow temperature = 667 K

6.4 DPM properties

Similar to the combustion model discussed in the previous section, the DPM was used. Important parameters with respect to the solid particle phase are given in Table 6.3. The different values for the volatile and carbon fractions are for ANN-Bio-CPD and the two other devolatilisation models, respectively. The values for the single-rate devolatilisation model differ from the DTF combustion simulations due to the slightly different bagasse ASTM proximate analysis.

Table 6.3: DPM properties

Property type	**Assigned values**
Injection	Flow rate = 2.7956 kg/s Temperature = 309 K Rosin-Rammler size distribution: Minimum = 0.0003 m Maximum = 0.01122 m Mean = 0.00143 m Spread parameter = 0.827656 Number of diameters = 10 Shape factor = 0.7
Material	Density = 500 kg/m^3 Specific heat as a function of temperature Swelling coefficient = 0.56 Volatile fraction = 0.8952, 0.8875 Carbon fraction = 0.1048, 0.1125
Devolatilisation	ANN UDF Single-rate model - Pre-Exponential factor = 3.12×10^6 s^{-1} Activation Energy =7.4×10^7 J/kgmol Constant-rate model - rate = 20 s^{-1} Vaporisation temperature = 400 K
Combustion	Diffusion limited - Binary diffusivity = unity Lewis number

6.5 Multiphase flow simulation setup

The theory section discusses the following models utilised. Similar models were utilised by Du Toit (2015).

The setup of the simulation is the same as the combustion case discussed in the previous chapter, except for the following.

There are local laminar zones above the grate at the front of the boiler due to low velocity. There are also multiple low Reynolds-number regions on the surfaces in the domain. However, the other areas, especially the jets, are highly turbulent. The realizable $k-\epsilon$ turbulence model of Shih *et al.* (1995) was used with non-equilibrium wall functions to simulate the near wall effects [Kim and Choudhury (1995)]. This choice of turbulence model differs from the simulations of Du Toit (2015) due to the current focus on the combustion before the superheater. Du Toit (2015) found that a low-Reynolds-number (LRN) approach for the turbulence model produced better results with respect to superheater heat transfer; however, the realizable $k-\epsilon$ model is superior with respect to jets, strong streamline curvature, vortices and rotating flow. The latter model was chosen since all these phenomena exist in the combustion chamber.

A two-step quasi-global chemical mechanism was used to reduce computational effort during the development phase of the research. It was found that the effect of turbulence on the rate of combustion is dominant in the boiler compared to the effect of chemistry and, therefore, a global mechanism or mixed-is-burnt approach is valid [Du Toit (2015)]. The mechanism utilised can be found in Appendix E.

The EDC of Magnussen (1981) was used for the turbulence-chemistry interaction which differs from the research of Du Toit (2015) where the EDM model of Magnussen and Hjertager (1976) was utilised.

The evaporation and boiling of the water from the bagasse particles were simulated with the convection/diffusion controlled model [Miller *et al.* (1998)][Sazhin (2006)] and boiling-rate equation [Kuo (2005)].

In addition to the bed model applied by Du Toit (2015) which captures the particles in a defined zone, fixed values of turbulent kinetic energy and dissipation rate were patched in the bed zone. These values were determined by CFD submodels of the grate bar nozzles and packed beds. Values of 6.82 and 2 331 were used for k and ϵ respectively. These values are required to account for the kinetic limited characteristic of the bed and turbulent diffusion of the species. A porous zone was also utilised to account for the pressure drop over the grate similar to Du Toit (2015). An inertial resistance of $2\,000\,\mathrm{m}^{-1}$ was used.

The bed model was implemented through UDF. A zone was defined which captures particles passing through. The particles stay in position until it becomes light enough to lift off due to mass loss. The primary air enters the furnace through this zone and lifts the particles if the drag force is greater than gravity.

The particle tracking in the bed zone is also modified to account for the longer time spent without adding unnecessary computations [Du Toit (2015)].

Polynomials from Peters and Weber (1995) were used for the specific heat of the species in the gas mixture. These polynomials have been modified in order to achieve more realistic temperature profiles with global reaction mechanisms.

The thermal conductivity and viscosity of the main species namely N_2, CO_2, O_2, H_2O and CO were taken from Rose and Cooper (1977).

A Rosin-Rammler particle size distribution from Du Toit (2015) was applied. Although the particles spheroidise from ignition, the wet bagasse particles spend a large part of the residence in the boiler below the ignition temperature due to the required evaporation and boiling of the water. Therefore, a non-spherical shape factor was used.

The steady state pressure-based solver was used with the SIMPLE algorithm for pressure-velocity coupling. The following spatial discretisation was used: least-squared cell based for gradients, the body force weighted scheme for pressure and the second-order upwind technique for momentum, k, ϵ, species and energy.

6.6 Mesh independence investigation

A formal mesh independence study as in the preceding sections was not conducted due to the size and complexity of the domain. However, Du Toit (2015) investigated grid independence and the same cell and particle count was used in this study.

The differences between the mesh of Du Toit (2015) and this research are the volumes for the secondary jets and the superheater tube bank.

The current study utilised hexahedral elements instead of tetrahedral cells for the secondary jet volumes. Mesh refinement in these volumes were done with adaption based on velocity gradients. The spreader jet volumes were also adapted. Adaption was applied until grid independence was obtained in these zones. Du Toit (2015) applied a finer mesh in the tetrahedral zones and no adaption for the spreader jets. The change from tetrahedral to hexahedral cells for the secondary air volumes was due to numerical stability, convergence and accuracy.

Yin *et al.* (2008) found that different mesh schemes lead to significant differences in the flow patterns, temperature- and species distributions. The mesh quality affects cell-face flux calculations and therefore directly impacts on the accuracy and convergence of the solution. Grid density also plays an important role in approximating the continuous solution discretely. A sensitivity study revealed the mesh as the most important parameter and a hexahedral grid was chosen, which is the same finding and choice of mesh in the current research. The size of

the domain, boiler geometry, thermal output and corresponding mesh cell count used by Yin *et al.* (2008) is also very similar to the current research.

The only differences between the mesh in the superheater tube bank of Du Toit (2015) and the current study is the fact that no steam flow was modelled and straight tube sections without bends were used. These changes simplified the mesh generation, improved the mesh quality and reduced the cell count considerably.

6.7 Results

The discussion of the results follow the development process of the boiler model with the future goal of simulating more detailed chemistry in order to predict pollutants.

A similar sensitivity analysis of model parameters as done by Du Toit (2015) was conducted. The use of a global chemical mechanism sped up the process considerably. Since similar qualitative conclusions as Du Toit (2015) were drawn, the model parameters were left unchanged, except the few alterations mentioned before. Only the results of the final mesh and model combinations are presented.

In the next step, the EDC model constants were tuned globally with respect to the measurements of species behind the superheater and flame temperatures observed with the thermal cameras.

In both cases the single-rate devolatilisation model was compared with ANN-Bio-CPD.

6.7.1 Standard EDC

The temperature predictions of the single-rate devolatilisation model and ANN-Bio-CPD are compared in Figures 6.3 and 6.4. The deviation from the experimental data of the two devolatilisation models is minimal with regard to temperature. The single-rate model correlates marginally better with the experimental data behind the superheater at the top elevation in Figure 6.3. There is a slight improvement using ANN-Bio-CPD when comparing the model to the measurements at the bottom elevation in front of the superheater in Figure 6.4. The overall correlation of both devolatilisation models with the experimental values is good.

However, the discrepancy of both devolatilisation models with the measurements of gas species is much larger, especially the CO data. The measurements of O_2 behind the superheater can be seen in Figure 6.5. The correlation of both models with measurements at the bottom elevation is similar and reasonably good. At the top elevation, the results of the single-rate model are marginally closer to the experimental data.

The results of CO in Figure 6.6 clearly indicates that both devolatilisation models under-predict this intermediate gas species considerably. The predictions of both models are very similar and thus the results of CO are insensitive to devolatilisation models.

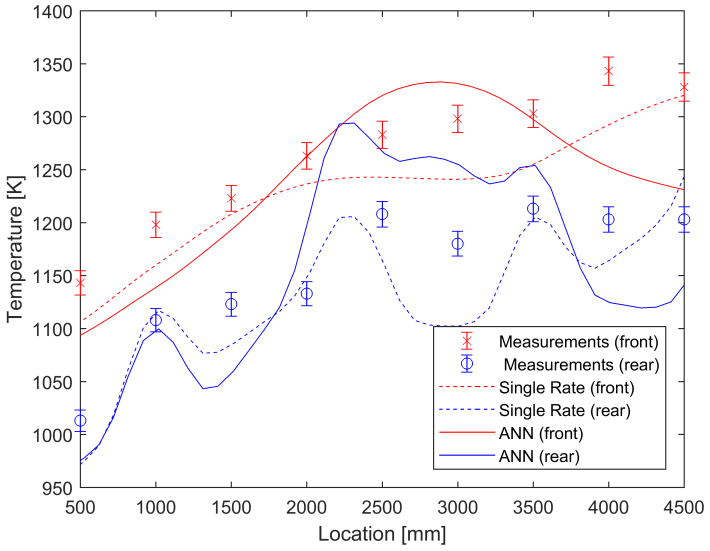

Figure 6.3: Temperature [K] at top elevation

Although temperatures were not measured in the lower furnace with the suction pyrometer, the thermal cameras can provide a good indication of the maximum temperatures expected. It was shown by Du Toit (2015) that the maximum temperature in the flame ball is approximately 1 500 K. In Figure 6.7 the maximum measured temperature with the Durag thermal camera was 1 393 K.

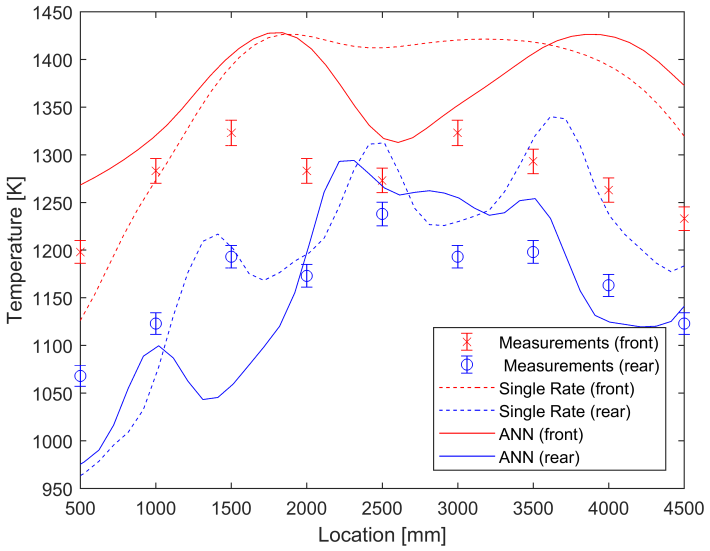

Figure 6.4: Temperature [K] at bottom elevation

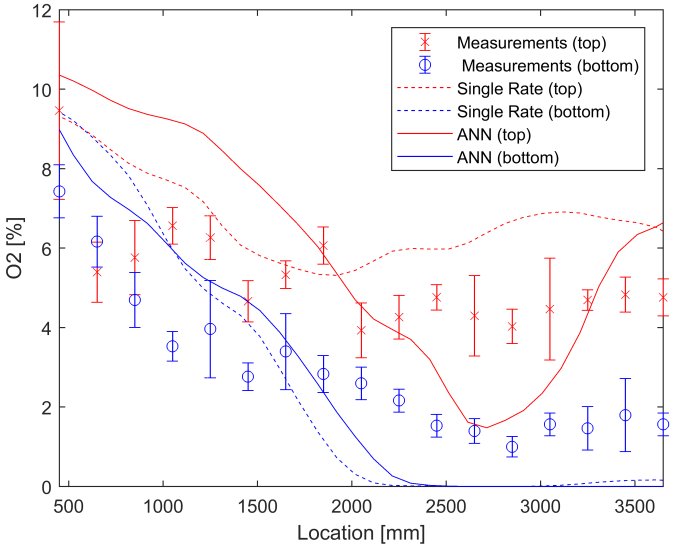

Figure 6.5: O_2 [%] at rear of superheater

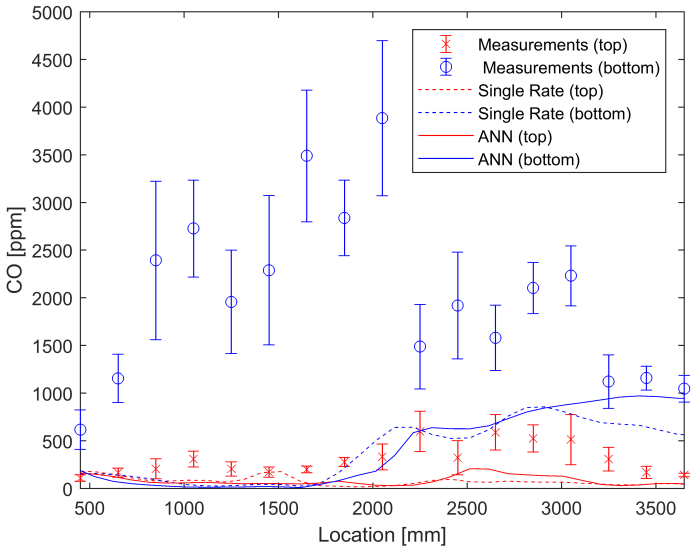

Figure 6.6: *CO* [ppm] at rear of superheater

The camera was positioned at grate level and towards the rear wall of the boiler. It was tilted upwards in order to view the bottom of the flame ball. In figure 6.8 the maximum measured temperature was 1 473 K. An in-house developed thermal camera was used for these measurements. The camera was positioned at nose level and towards the rear wall of the boiler. It was tilted downwards to view the top of the flame ball.

Figures 6.9a to 6.10b illustrate the temperature contours on planes through the middle of the boiler and in line with a spreader. The values have been clipped to a maximum of 1 500 K in order to identify the areas on the plane above the maximum measured temperature with the thermal cameras. It is clear that both devolatilisation models over-predict the temperature in the flame ball. The surface above 1 500 K is slightly smaller using ANN-bio-CPD on both planes.

Now that it has been established that the *CO* reaction is too fast in the region of the boiler simulation upstream from the *CO* measurements and the temperature prediction too high in this volume, the cause of the model inaccuracies needs to be identified. Since the main deficiencies of the current implementation of the EDC is low Reynolds-number regions and low Damköhler number flows, contours of these parameters were investigated.

It can be seen in Figures 6.11a and 6.11b that there is a region above the grate up to the first jet where the turbulent Reynolds number is below 64, which is outside the operational range of the EDC model. It is also evident from Figures 6.12a and 6.12b that areas where the Damköhler number is 1 and below exist

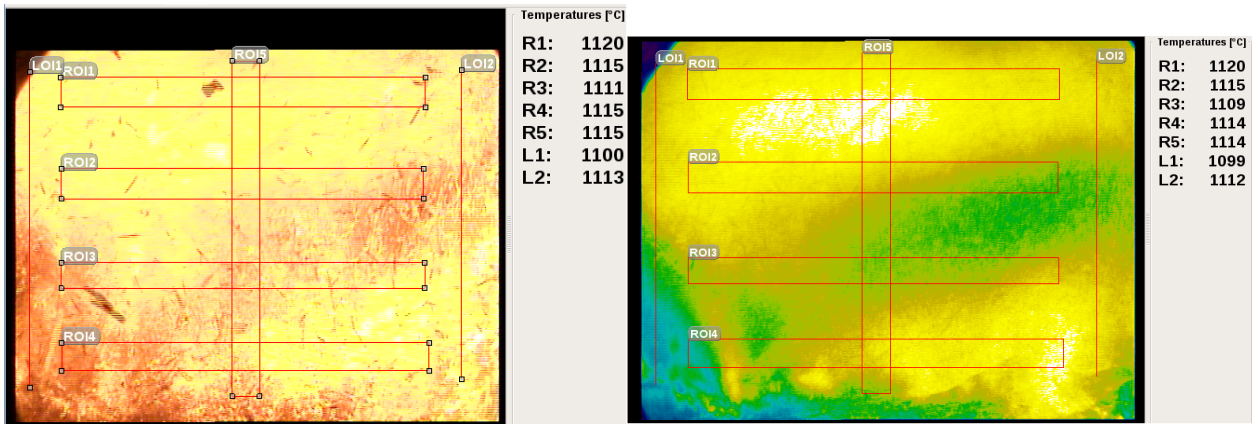

Figure 6.7: Temperature measurements below flame ball with Durag thermal camera

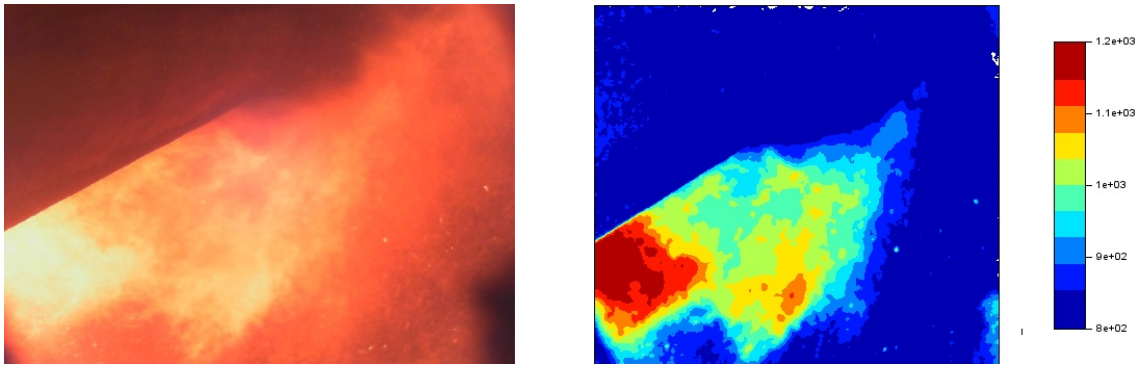

Figure 6.8: Temperature measurements above flame ball with John Thompson thermal camera [Du Toit (2015)]

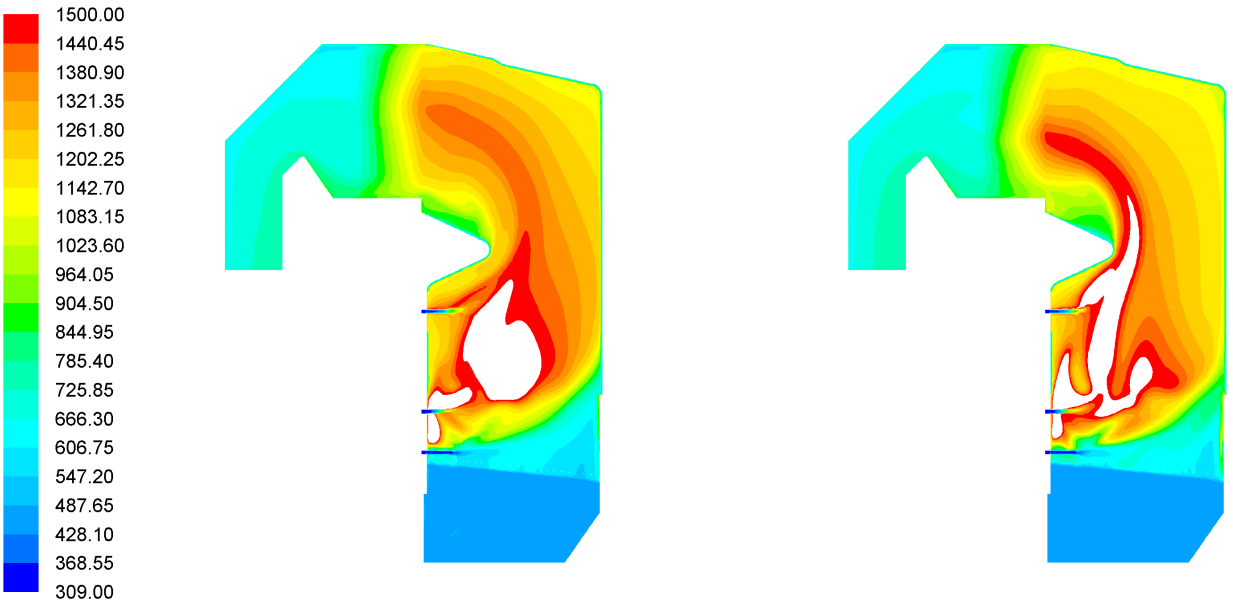

(a) Single rate (b) ANN-Bio-CPD

Figure 6.9: Temperature contours on symmetry plane of boiler simulation

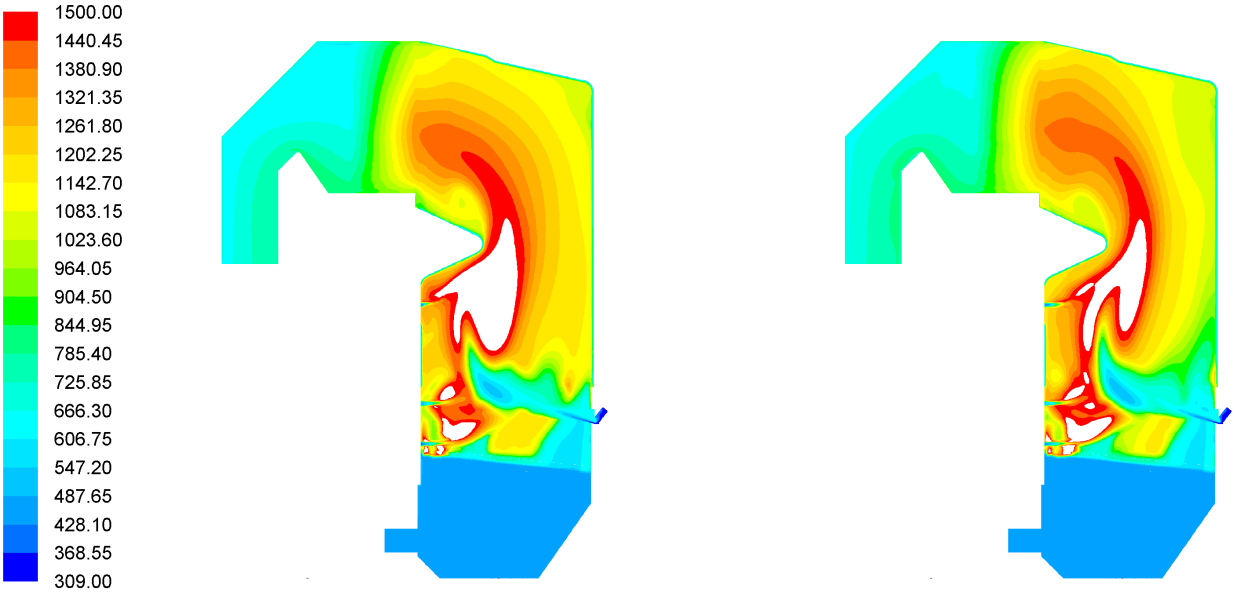

(a) Single rate (b) ANN-Bio-CPD

Figure 6.10: Temperature contours on spreader plane of boiler simulation

directly above these low Reynolds-number regions. The reaction rate constant of the CO reaction was used to calculate the Damköhler number, since the volatile reaction is infinitely fast.

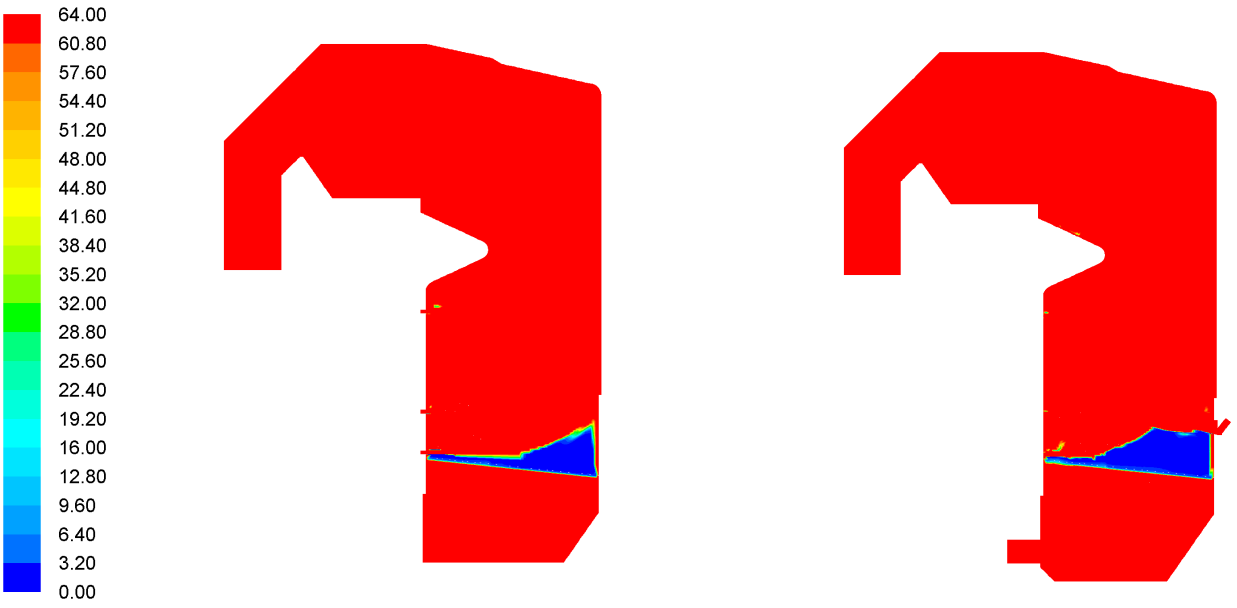

(a) Symmetry plane (b) Spreader plane

Figure 6.11: Turbulent Reynolds-number contours of boiler simulation with ANN

It is therefore hypothesised that the formulation of the EDC model in ANSYS® Fluent is not valid in parts of the boiler simulation upstream of the CO measurements. This could be the cause for the under-prediction of CO in the boiler simulation behind the superheater and corresponding over-prediction of temperature in the flame ball.

6.7.2 Modified EDC

In order to investigate the hypothesis made in the previous section, simulations with different EDC model constants were run. Farokhi and Birouk (2016*b*) simulated a small-scale fixed-bed furnace with variations of these parameters. C_γ and C_τ of 1.75 and 5.62 respectively produced the lowest temperatures in their tests and good correlation with experimental values. These values were therefore used as a starting point for the current investigation. The resulting values of CO were slightly too high but much closer to the measurements. Only very small zones exceeded the maximum measured temperature of 1 500 K. It was decided to reduce

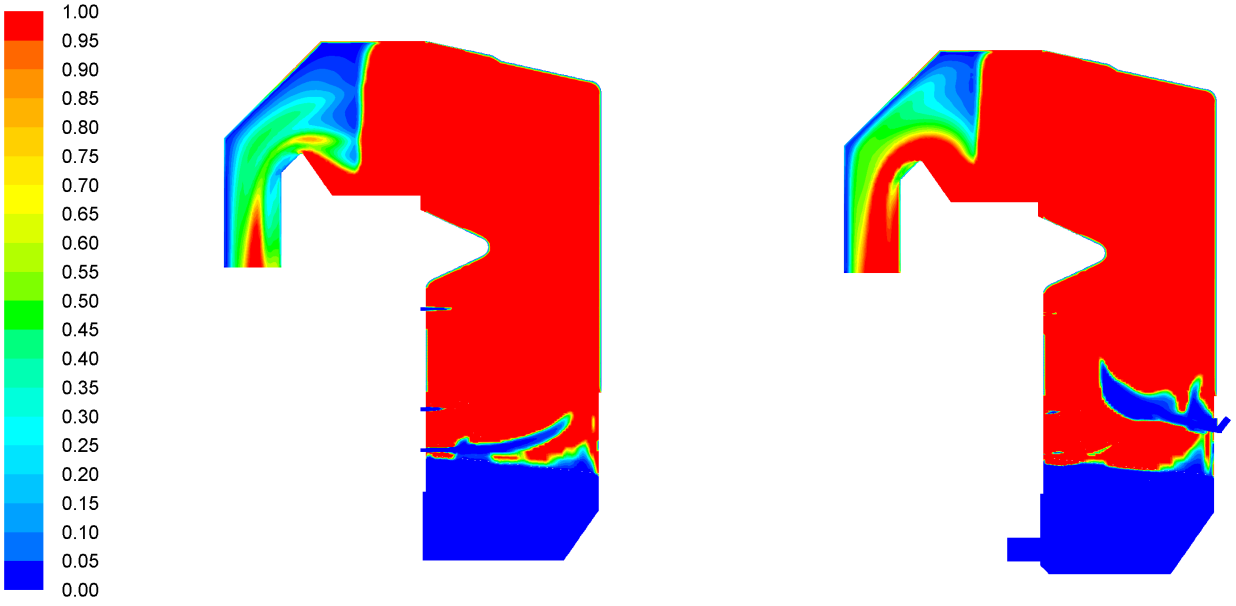

(a) Symmetry plan (b) Spreader plane

Figure 6.12: Damköhler number contours of boiler simulation with ANN

the value of C_τ in order to lower the CO predictions behind the superheater. The final value of the results presented below is 4.31.

The temperature predictions of the single-rate devolatilisation model and ANN-Bio-CPD are compared in Figures 6.13 and 6.14. It is striking that the results of the two devolatilisation models are almost identical, especially at the top elevation. Although the model results at the top elevation in front of the superheater are very similar to using the default constants, the results at the top elevation behind the bank shows a larger discrepancy with the measurements than before. A peak of approximately 100 K higher than the temperatures at the front can be seen. None of the temperature measurements are higher at the rear compared to the front of the superheater at the same elevation. The results of temperature at the bottom elevation in front of the superheater shows better correlation with the measurements compared to the results with the default EDC model constants. However, the temperatures at the rear are also higher than the measurements compared to using the default constants. There is also a peak where the temperatures at the rear is higher than the front, although it is marginal.

However, the discrepancy of both devolatilisation models with the measurements of gas species is much less compared to using the default model constants, especially the CO data. The measurements of O_2 behind the superheater can be

seen in Figure 6.15. The correlation of both models with measurements at the top- and bottom elevations is similar and reasonably good. The correlation with site data is better at the top elevation compared to using the default EDC model constants.

The results of CO in Figure 6.16 clearly indicates that using the modified EDC model constants increases the values predicted for this intermediate gas species behind the superheater considerably bringing the model results closer to the measurements. Although the values at the top elevation are higher than the measurements in areas and higher compared to using the default model constants.

Again, as with the temperature model predictions, it is striking how close the results of both devolatilisation models are with regard to gas species.

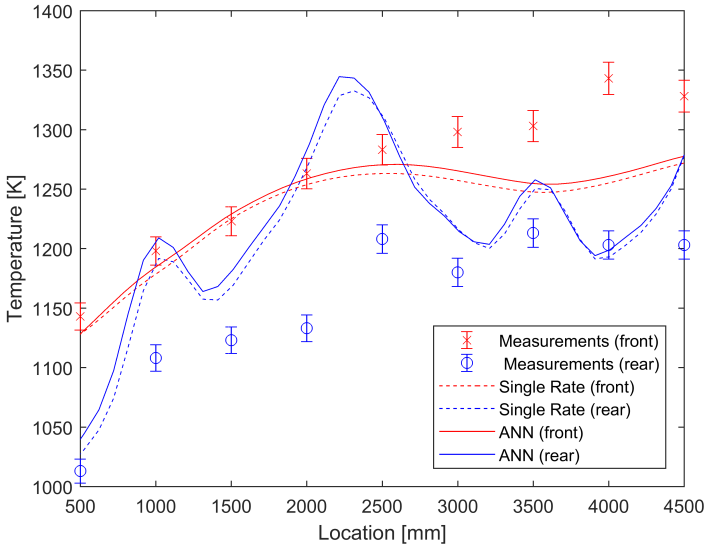

Figure 6.13: Temperature [K] at top elevation, modified EDC

Figures 6.17a to 6.18b illustrate the temperature contours on planes through the middle of the boiler and in line with a spreader. The values have been clipped to a maximum of 1 500 K in order to identify the areas on the plane above the maximum measured temperature. It is clear that the temperature in the flame ball is drastically reduced with the modified EDC model constants. The surface above 1 500 K is similar for both devolatilisation models and only in the region of the bottom two secondary air jets.

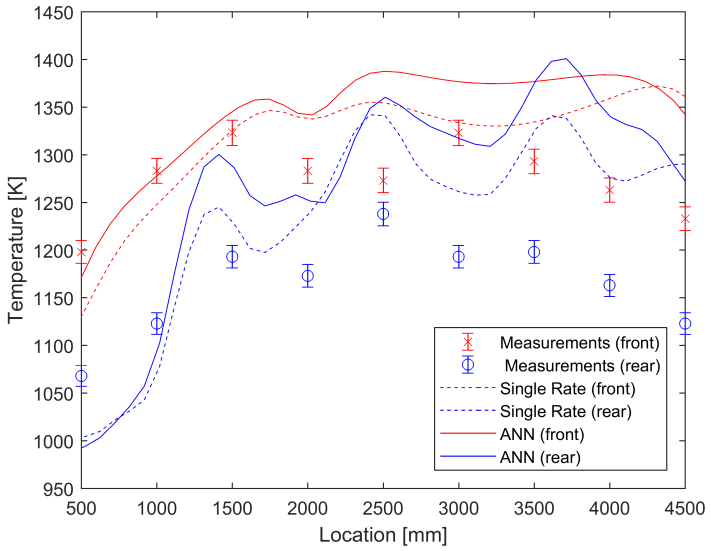

Figure 6.14: Temperature [K] at bottom elevation, modified EDC

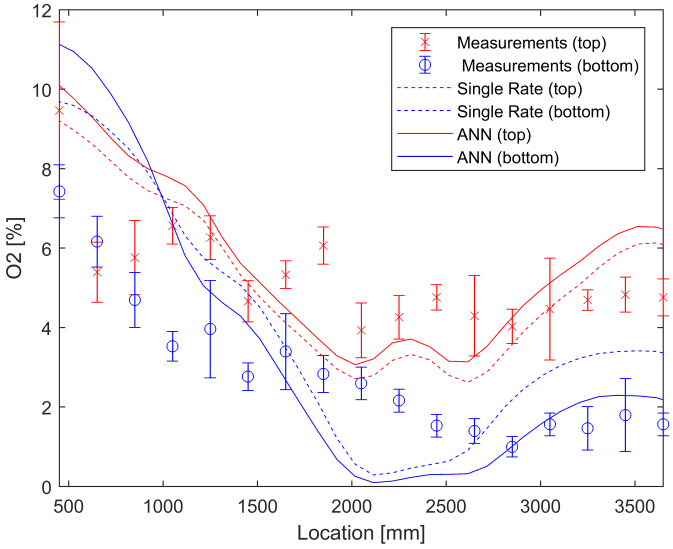

Figure 6.15: O_2 [%] at rear of superheater, modified EDC

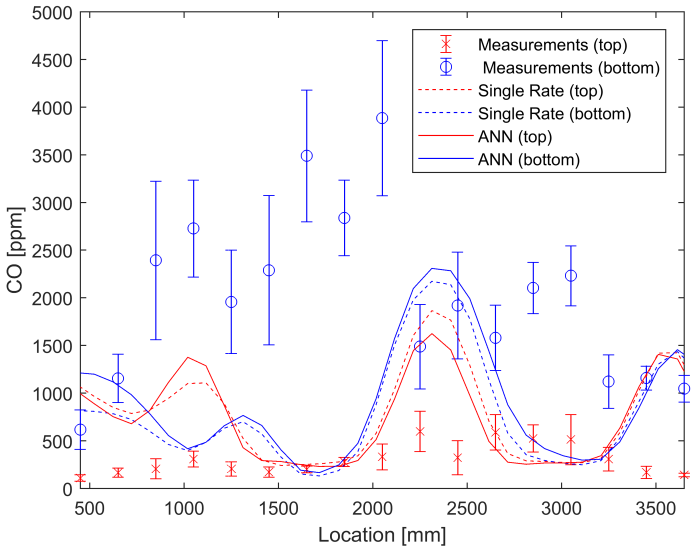

Figure 6.16: *CO* [ppm] at rear of superheater, modified EDC

Therefore, the largest impact of changing the EDC model constants is lowering the temperature of the flame ball in the middle of the boiler simulation below the maximum values observed with the thermal cameras. Streaks of high temperatures are seen on grate level at the front of the boiler simulation using the ANN devolatilisation model, which is also more realistic.

In Figure 6.19, the position of the top part of the flame can be seen. The Durag thermal camera was positioned in front of the superheater and the footage taken from the front wall of the boiler. It is clear that the flame extends to the roof of the combustion chamber. At times, it was even observed behind the superheater and in the main bank.

Since the *CO* species is the last intermediate product, it was chosen as the marker of the flame volume. The 0.01 contour of the near-zero ratio (the local *CO* molar fraction divided by the maximum over the whole domain) was used as the boundary of the reaction zone [Mei *et al.* (2012)].

The flame volume in the region before the *CO* measurements is compared in Figures 6.20a and 6.20b for the simulation results using the default- and modified EDC model constants respectively. The iso-surfaces are not an accurate representation of the boundary of the flame, but a good indication for a qualitative comparison. The flame is considerably lower in the simulation with the default model constants. The modification of the constants extends the flame to the roof of the furnace and up to the exit of the superheater. This flame boundary is much closer to the observations with the thermal camera in Figure 6.19.

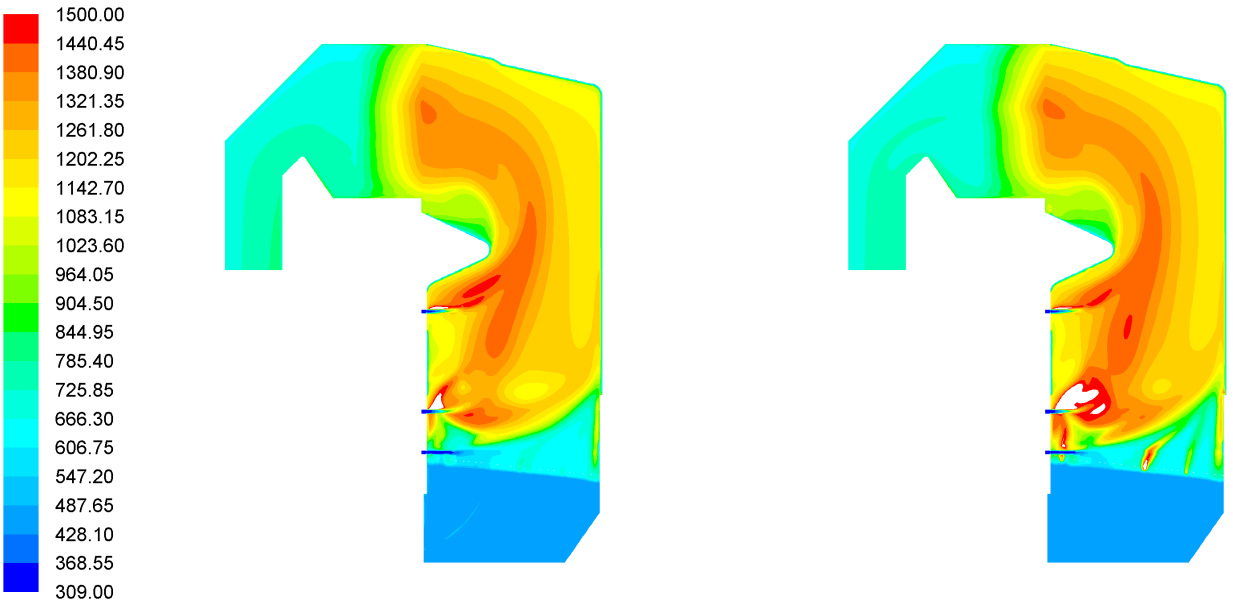

(a) Single rate (b) ANN-Bio-CPD

Figure 6.17: Temperature contours on symmetry plane of boiler simulation

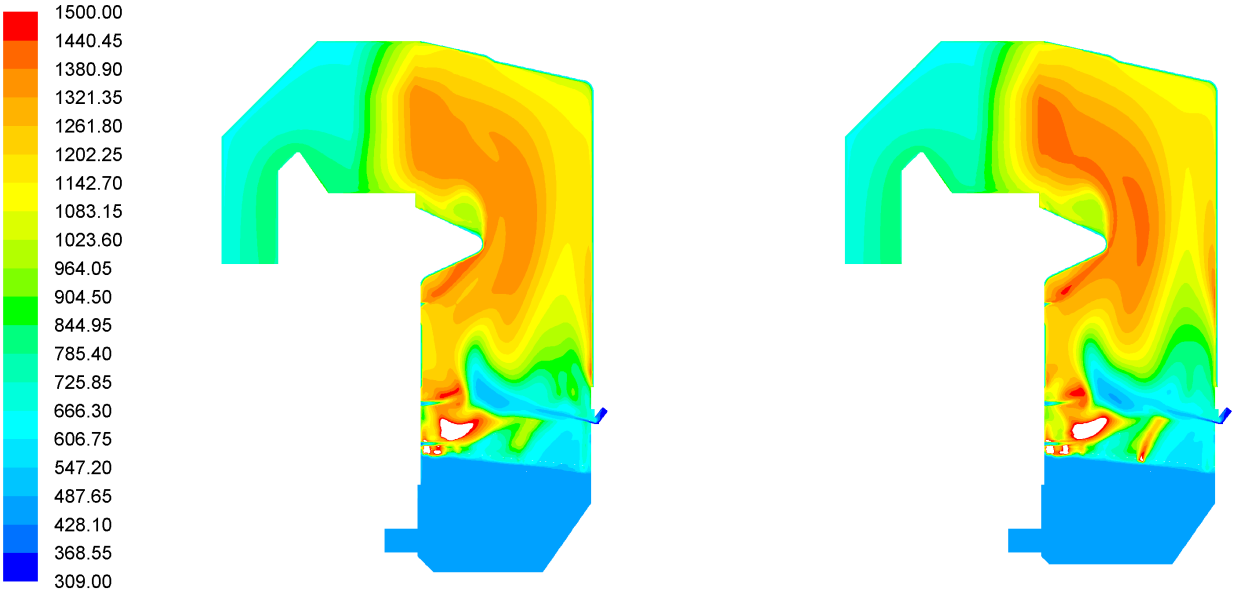

(a) Single rate (b) ANN-Bio-CPD

Figure 6.18: Temperature contours on spreader plane of boiler simulation

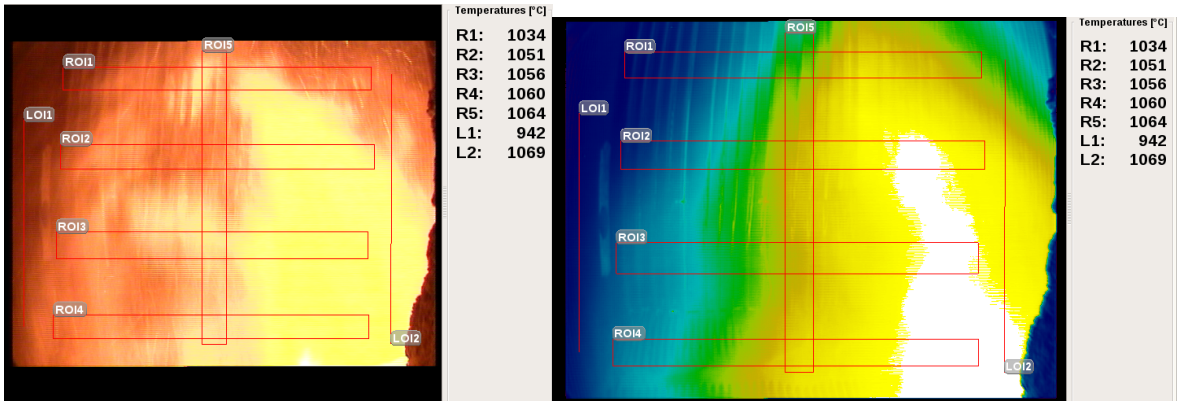

Figure 6.19: Temperature measurements in front of superheater with Durag thermal camera

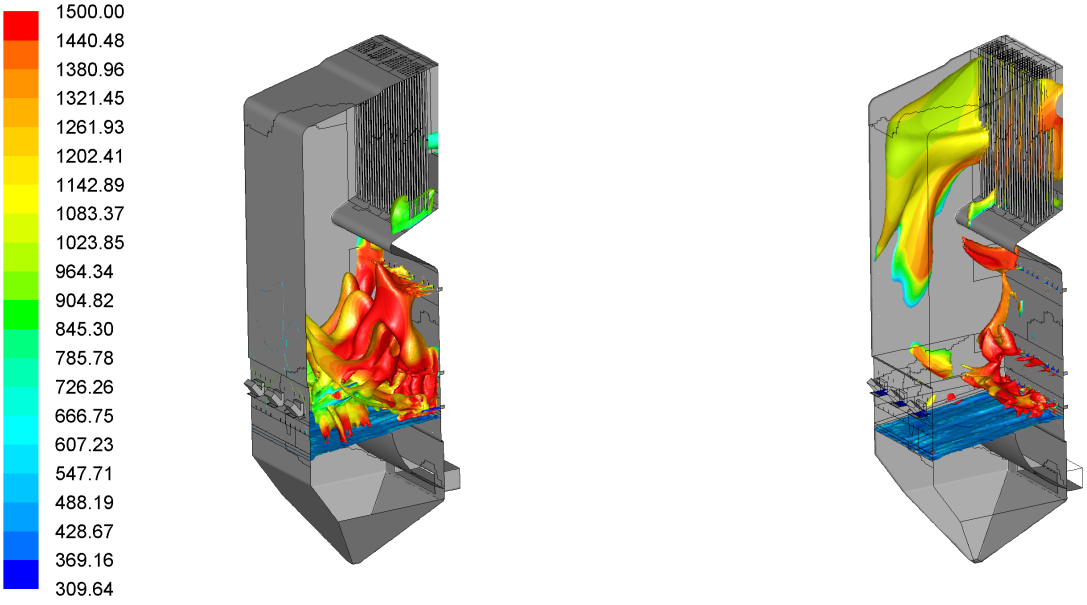

(a) Defualt constants (b) Modified constants

Figure 6.20: Flame position of boiler simulation

The heat transfer to the different boiler components is tabulated in Appendix E. It also indicates a faster CO reaction and resulting higher temperatures upstream from the superheater with the default EDC model constants. The modified constants produced results closer to Du Toit (2015) with regard to furnace heat transfer.

It is interesting that the improvement of the model predictions was achieved by lowering C_γ and increasing C_τ. Aminian and Galetti (2012), De *et al.* (2011), Evans *et al.* (2015), Parente *et al.* (2016) and Bao (2017) came to the same conclusion for MILD combustion.

Moderate and Intense Low-oxygen Dilution (MILD) combustion is defined in the following ways:

- MILD combustion occurs when the reactants are preheated above their self-ignition temperature and when enough inert products are entrained in the reaction region to dilute the flame [Aminian and Galetti (2012)]. The resulting flame front is not identifiable and therefore it is also called flameless combustion. The maximum temperature increase achieved during this form of combustion usually remains lower than the auto-ignition temperature of the mixture.
- High Temperature Air Combustion (HiTAC) is based on the dilution of fuel and combustion air by burnt gases and have similar characteristics with the MILD regime.
- It has also been called Flameless Oxidation (FLOX).

MILD combustion has the following characteristics:

- One of the key points is that the slower reaction rates cause a very strong coupling between turbulence and chemistry. The time scales of these two phenomena are similar in MILD combustion and therefore the Damköhler number usually approaches unity. It is therefore a real test for turbulence-chemistry interaction models.
- The oxygen content for transitional to MILD conditions are 9 to 3 % respectively in the oxidiser stream.
- The temperature band of MILD flames is 1 100 to 1 500 K. The regime is characterised by a more uniform and homogeneous reaction zone leading to lower temperatures and less temperature peaks with a smooth radiation flux.
- The flame is hardly visible or audible and thus inherently stable [De *et al.* (2011)].

- Flames in the transitional to MILD regime has been reported to be visually lifted [Evans *et al.* (2015)].
- The flame can be totally colourless, blue or green in rare cases [Bao (2017)].
- High combustion efficiency with low pollutant emissions is achieved.
- MILD combustion can accommodate a large fuel flexibility and is therefore ideal for low-calorific fuels [Parente *et al.* (2016)].
- MILD combustion is stable when the ratio of the recirculated exhaust gas over the total mass flow is more than 3 and the furnace temperature is larger than 1 073 K [Bao (2017)].

These characteristics are achieved by the following:

- The product gases of combustion are recirculated into the incoming fresh air, thereby raising the reactant temperature and reducing the oxygen concentration. It is achieved by the internal aerodynamics of the combustion chamber in conjunction with high velocity burners.
- Flue-gas recirculation and staged combustion with advanced secondary-air systems in boilers can also be used to create transitional to MILD zones.

The EDC over-predicts temperature of MILD combustion. The intermediate species, CO, was also incorrectly predicted. The results were consistently better with a lower value of C_γ and higher value of C_τ. Parente *et al.* (2016) formulated these constants in terms of turbulent Reynolds number and Damköhler number. The following improvement was derived by Bao (2017):

$$C_\tau = \frac{1}{2}\frac{1}{\sqrt{Re_t + 1}Da} \tag{6.1}$$

$$C_\gamma = \sqrt{\frac{3}{2}(Re_t + 1)Da^{3/4}} \tag{6.2}$$

From Equations 6.1 and 6.2 it can be seen that lower values of Re_t and Da increase C_τ and decrease C_γ, respectively.

Kjäldman *et al.* (1999) also found that increasing the time scale of the EDC improved predictions of local extinction and re-ignition in flames.

It has been established in the previous section that there are regions in the boiler with a Damköhler number of unity. The temperature range measured in the flame is around 1 100 to 1 500 K. Comparing the circled reaction zone in Figures 6.21a and 6.21b, an oxygen content of 3 to 9 % can be seen in the co-flow. The

flame appeared to be visually lifted in the boiler when viewed through the thermal camera. Bagasse combustion is also unstable due to the high moisture of the fuel. A cyclic phenomena is common with drying and subsequent ignition. Therefore, this bagasse-fired boiler shares characteristics of transitional to MILD combustion with local extinction and re-ignition, which explains why the corresponding modification of the model constants delivered better results.

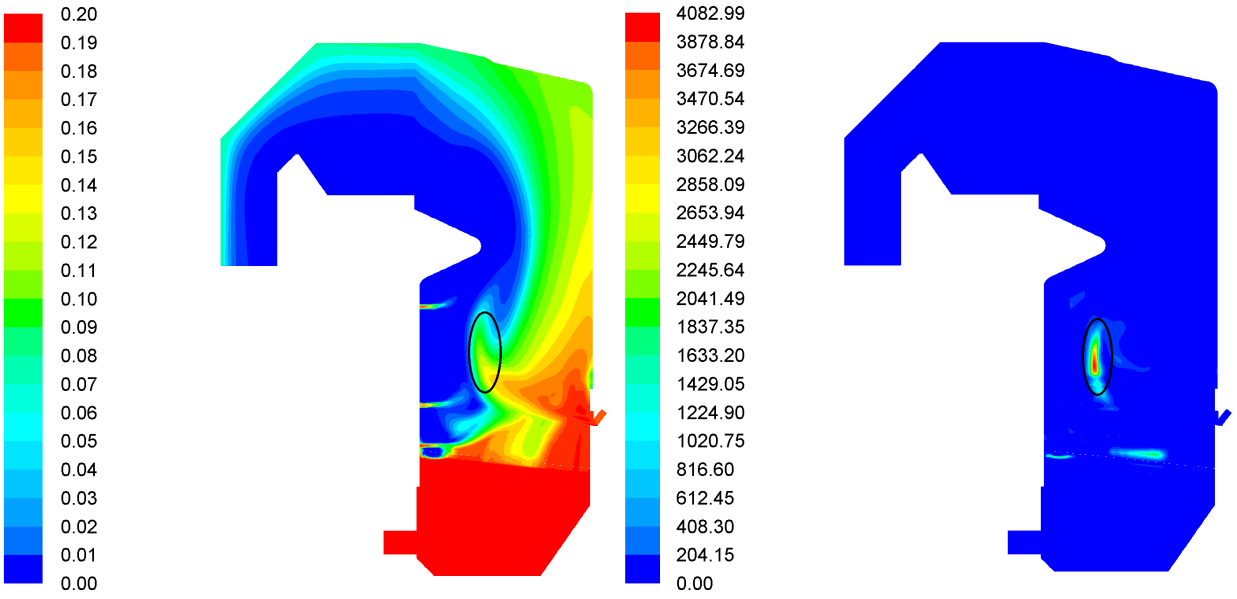

(a) O_2 molar fraction (b) Heat of reaction (W)

Figure 6.21: Characteristics of transitional to MILD combustion in the boiler simulation

The hypothesis from the previous section was not categorically proven, but a strong case was formed considering the comparison of the results from the simulation with the modified EDC model constants to measurements and visual observations in the boiler. The modified EDC produced more realistic results consistently. In some areas, the results deviated slightly more from measurements, e.g. the temperature measurements behind the superheater bank and CO measurements behind the superheater at the top elevation, but the overall global effects were closer to reality.

These discrepancies with the measurements could potentially be improved with local tuning of the model constants, as the majority of the reaction volume before the CO measurements are within the validity of the default EDC. However, simula-

tions using Equations 6.1 and 6.2 delivered similar results compared to the default model constants. This could indicate that the local extinction and re-ignition phenomena is a larger contributor to the model inaccuracies than the transitional to MILD regime. Therefore, the extinction criteria of Gran *et al.* (1994) with the standard EDC was utilised. Extinction occurred when the EDC time scale is less than the chemical time scale. Unfortunately, it also delivered similar results compared to the default model.

Ultimately, the hybrid low-Reynolds model of Shiehnejadhesar *et al.* (2014) is recommended in combination with a modification of Equation (3.28) to account for the reactions in the surrounding fluid as shown in Magnussen (2005). These modifications would account for the deficiencies of the current implementation in ANSYS® Fluent in the low Reynolds- and Damköhler-number regions identified in the boiler simulation. The local extinction and re-ignition phenomena also need further consideration; revision of the EDC was suggested by Kjäldman *et al.* (1999) due to the different time scales involved.

The observed results with the standard EDC model constants namely, a CO reaction which is too fast and corresponding over-prediction of temperature, are typical outcomes from using global chemistry. Therefore a study on the effect of more detailed chemistry with the EDC is recommended as a next step before EDC modifications are explored further.

Chapter 7

Conclusion and recommendations

In this section, the body of work will be summarised and a discussion will follow, leading to conclusions and recommendations.

7.1 Summary and conclusions

The objective of this study was to implement and validate the EDC turbulence-chemistry interaction and CPD model on an industrial scale in a bagasse-fired boiler.

Since the version of the CPD model suitable for biomass, Bio-CPD, is not available in commercial or open-source CFD software, it had to be added to the commercial software package, ANSYS® Fluent, by means of UDFs. A reduced-order model was created with machine-learning techniques in order to achieve ease of implementation and computational cost reduction.

The motivation for using the EDC and Bio-CPD model on an industrial scale is the need for more detailed chemistry in order to predict pollutants formed during the combustion process. Other applications are fouling-, combustion instabilities-, gasification- and torrefaction modelling.

A literature review was conducted and structured in three parts, namely turbulence-chemistry interaction modelling, devolatilisation modelling and machine learning in CFD.

An overview of the models available and the motivation for the specific choice of models was provided in Chapter 2. Applications by research groups were investigated.

A brief section covering the conservation equations and closure involved in CFD modelling was included. Since the heterogeneous process of devolatilisation was considered in detail, a concise description of the solid particle phase was added.

An in-depth discussion of the theory behind the advanced models and artificial intelligence techniques utilised was given in Chapter 3.

Combining the knowledge from the literature review with the in-depth study of the theory, the advanced models and techniques could be effectively applied in order to achieve the objective of the research and prove the hypothesis.

Development of reduced-order model

Since ANNs are the most accurate and adaptable machine-learning technique it was used to develop a ROM of Bio-CPD. Only the volatile yield as a function of final temperature and heating rate was captured.

A hybrid model consisting of an ANN and one-step reaction was used. It assumes that the rate of devolatilisation is first-order dependent on the volatiles remaining, similar to the single-rate approach. However, the kinetic rate obtained from the ANN is a function of temperature and heating rate. The ANN database can be visualised as a hyper plane of temperature, heating rate and volatile yield. Since Bio-CPD considers biomass as a mass weighted-average of cellulose, hemicellulose and lignin, three hybrid models were utilised.

MATLAB® was used in order to generate the data for ANN training with Bio-CPD as a simulator. The limits on heating rate of the data set were determined by inspecting the time-temperature history of the fuel particles in the boiler simulation.

A two-layer network was chosen due to the simplicity of the hyper-plane relationship. The hyperbolic tangent sigmoid function in both layers delivered the best results. A network with 10 neurons in the hidden layer was chosen to reduce computational effort, which resulted in an average error of 0.6 %. Partitioning the data space in combination with 30 neurons in the hidden layer reduced this error to 0.3 %.

The in-sample and out-of-sample error is exact, confirming that the data is sufficient. The suitability of the network architecture was checked by varying the amount of neurons and regression plots.

The speed-up of executing the ROM was tested in MATLAB®. Data-set generation with the CPD code was compared to processing the data with the ANN. The overall model speed-up is 450 times faster compared to using the traditional ODE solver of the CPD code.

A constant heating rate reactor model was developed in C combining the three hybrid modules in order to test the functionality without interfacing with ANSYS® Fluent.

The reactor model was implemented in the CFD model. Variables tracked were stored with DEFINE_DPM_SCALAR_UPDATE and the devolatilisation rate customised with DEFINE_PR_RATE.

Validation of reduced-order model

The reactor model was used to simulate constant heating rate wire mesh experiments with bagasse. Heating rates of 1 K/s and 1 000 K/s were investigated by comparing widely published experiments of Stubington and Aiman (1994) and Drummond and Drummond (1996) to model predictions. The chosen rates are typical extreme cases in bagasse-fired boilers.

ANN-Bio-CPD qualitatively captured the effect of heating rate on bagasse devolatilisation with a slight under-prediction in maximum volatile yield. An encouraging characteristic noted is the change in slope of the curve for the model predictions at 20 % yield. Rabacal *et al.* (2014) noticed the same trend. It corresponds to the release of hemicellulose and is typically seen in TGA experiments. The quantitative values of the lower and higher heating rates also corresponded reasonably well to the experimental data.

The DTF devolatilisation experiments of Wagenaar *et al.* (1993) were modelled. The temperatures and heating rates involved in the experiments correspond well to the conditions in a bagasse-fired boiler. The added benefit of choosing this experiment is the Bio-CPD model results of Lewis and Fletcher (2013) that could be compared.

The ANN-Bio-CPD model captured the devolatilisation behaviour of Pine sawdust at high heating-rate conditions reasonably well. The qualitative trends of predicted mass conversion with varying heating rate in the temperature band from 773 K to 873 K compares well to the measurements. The quantitative values also correspond reasonably well, except for an under-prediction in maximum yield as found with the bagasse wire-mesh reactor experiments. Therefore, the CFD implementation of ANN-Bio-CPD functions correctly for devolatilisation in an inert environment.

The DTF combustion experiments of Khatami and Levendis (2015) with single bagasse particles were simulated. These tests were designed for boiler conditions. The added benefits of modelling these experiments were isolating the combustion phenomena from turbulence due to quiescent flow conditions and eliminating inter-particle effects since only a single particle was used. The char combustion model and release of multiple species from the particle surface which, is required for detailed chemistry, could also be validated.

The results of ANN-Bio-CPD compared reasonably well to the experiments. ANN-Bio-CPD initiates ignition at the correct temperature and the total burn time corresponds to the experimental data. The delay to ignition is longer than the experiments and requires intra-particle gradients to be taken into account for higher accuracy. The split between volatile content and char content has an effect on volatile and char flame duration. Due to the under-prediction in maximum volatile yield, ANN-Bio-CPD predicts a slightly shorter volatile flame duration

and longer char burn time compared to the experiments. The single-rate model compared better to the experimental value of volatile burn time, due to the larger volatile content used, but did not produce a higher reactivity of part of the particle, as is the case with hemicellulose. The constant-rate model initiated ignition at too low a temperature and over-predicted the total burn time due to a resulting longer volatile flame duration. Therefore ANN-Bio-CPD is the model of choice when considering realistic energy release due to the more reactive hemicellulose component. There is, however, room for improvement, considering maximum volatile yield.

The diffusion limited char combustion model predicts a burn time and peak temperature that correspond reasonably to experimental data. It is therefore a suitable simplistic model, considering the small amount of char in biomass.

Industrial CFD simulation

The final application of ANN-Bio-CPD was investigated by modelling the experiments of Du Toit (2015) on boiler no. 3 at RCL Komati sugar mill. This boiler is a typical example of a bagasse-fired design on an industrial scale. Predictions from an upgraded version of the model developed by Du Toit (2015) were compared to measurements of Du Toit (2015).

A two step global mechanism was used with the standard EDC. The use of a global chemical mechanism sped up the process considerably during the sensitivity analysis. The results were compared to measurements on the boiler. The standard EDC under-predicted CO in the boiler simulation behind the superheater and correspondingly over-predicted temperature in the flame ball. Areas in the boiler with turbulent Reynolds numbers below 64 and Damköhler number of unity and less were identified. From these findings, it is hypothesised that the formulation of the EDC in ANSYS® Fluent is not valid in parts of the boiler simulation upstream of the CO measurements.

In the next step, the EDC model constants were tuned globally with respect to the measurements of species behind the superheater and flame temperatures observed with the thermal cameras. The hypothesis was not categorically proven, but a strong case was formed considering the comparison of the results from the simulation with the modified EDC model constants to measurements and visual observations in the boiler. The modified EDC produced more realistic results consistently. In some areas, the results deviated slightly more from measurements, e.g. the temperature measurements behind the superheater bank and CO measurements behind the superheater at the top elevation, but the overall global effects were closer to reality.

By interrogating the results further, it was established that the boiler shares characteristics of transitional to MILD combustion with local extinction and re-ignition. It explains why the corresponding modification of the model constants

delivered better results since similar changes to the EDC improved the prediction of these phenomena by other researchers, namely Aminian and Galetti (2012), De *et al.* (2011), Evans *et al.* (2015), Parente *et al.* (2016), Bao (2017), Gran *et al.* (1994) and Kjäldman *et al.* (1999).

In both cases, the single-rate devolatilisation model was compared with ANN-Bio-CPD and similar results were seen. Only with the modified EDC model constants were streaks of high temperatures seen on grate level at the front of the boiler simulation using the ANN devolatilisation model, which is more realistic.

The discrepancies with the measurements could potentially be improved with local tuning of the model constants, as the majority of the reaction volume before the *CO* measurements are within the validity of the default EDC. However, simulations using Equations 6.1 and 6.2 delivered similar results compared to the default model constants. This could indicate that the local extinction and re-ignition phenomena is a larger contributor to the model inaccuracies than the transitional to MILD regime. Therefore, the extinction criteria of Gran *et al.* (1994) with the standard EDC was utilised. Extinction occurred when the EDC time scale is less than the chemical time scale. Unfortunately, it also delivered similar results compared to the default model.

Ultimately, the hybrid low-Reynolds model of Shiehnejadhesar *et al.* (2014) is recommended in combination with a modification of Equation (3.28) to account for the reactions in the surrounding fluid as shown by Magnussen (2005). These modifications would account for the deficiencies of the current implementation in ANSYS® Fluent in the low Reynolds- and Damköhler-number regions identified in the boiler simulation. The local extinction and re-ignition phenomena also need further consideration; revision of the EDC was suggested by Kjäldman *et al.* (1999) due to the different time scales involved.

However a study on the effect of more detailed chemistry with the EDC is recommended as a next step before model modifications are explored further.

The composite industrial model developed in this body of work can be used in new boiler design and plant modification. Simulations with large low Reynolds- and Damköhler-number zones should be approached with caution, although the model has been tuned for these effects.

With reference to Section 1.5, the applications of slow reactions could deliver conservative results due to slower overall reaction rates in the absence of the reactions in the surrounding fluid. Other applications will be improved due to the higher level of detail captured compared to the EDM with a single-rate devolatilisation model.

The reactor and DTF models can be used to validate ANN-Bio-CPD for other biomass fuels. ANN-Bio-CPD can confidently be used for other applications on a laboratory, pilot and industrial scale.

Boiler design houses do not use the level of CFD simulation developed in this research as best practice. The norm is EDM with the single-rate devolatilisation model, although most boilers are designed with lumped parameter approaches. Pollution emissions are becoming important, though; especially NO_x for bagasse firing, requiring SNCR. CFD is used for SNCR design by boiler companies, but the chemistry of the NO_x reactions is rarely modelled. If it is modelled, it is only done so in a post-processor mode. The model developed in this body of work is therefore a contribution to industry.

7.2 Recommendations and future work

As an extension to the model developed in the present thesis, the following research can be further investigated:

1. Study the effect of more detailed chemistry with the EDC in a boiler simulation as a next step.

2. Apply the modelling strategy developed in this body of work to another case study. After a recent testing campaign at Sezela sugar mill, boiler no. 1 is an ideal case. During the campaign, suction pyrometer measurements were taken in the lower furnace and therefore the prediction of temperature by the EDC in this region can be further investigated.

3. Split the solid volatile fraction in the particles into tar, light gas and fuel-bound nitrogen fractions. Release each component separately with multiple surface reactions. The rates can be determined by an extension of ANN-Bio-CPD that includes these extra parameters as outputs. The resulting model will be more accurate with regard to detailed chemistry.

4. Change ANN architecture to 30 neurons and partition the data space by using more ANNs. This will reduce the error at a higher computational expense.

5. Collaborate with BYU in order to investigate the deficiencies of Bio-CPD and adjust the structural and kinetic parameters accordingly. The resulting ROM could potentially be more accurate with regard to maximum volatile yield.

6. Use the CHL devolatilisation model of Biagini (2003) as a simulator in order to generate training data. The resulting ROM could potentially be more accurate.

7. Implement the hybrid low-Reynolds model of Shiehnejadhesar *et al.* (2014) in combination with a modification of Equation (3.28) to account for the reactions in the surrounding fluid as shown by Magnussen (2005). These modifications would account for the deficiencies of the current implementation in ANSYS® Fluent of the EDC in the low Reynolds- and Damköhler-number regions identified in the boiler simulation. The local extinction and re-ignition phenomena also need further consideration; revision of the EDC was suggested by Kjäldman *et al.* (1999) due to the different time scales involved and this approach can be pursued.

8. Investigate the Unsteady Flamelet Model (UFM) and run boiler simulations with it as alternative turbulence-chemistry interaction. Farokhi and Tabet (2017) found this approach promising for grate biomass furnaces.

9. Investigate the composition PDF transport model and run boiler simulations on a high-performance computing platform with it as alternative turbulence-chemistry interaction. If the resulting improvement merits further investigation, a physics-informed machine-learning approach could be pursued in order to reduce the computational cost.

10. Refine the boiler simulation by incorporating a thermally thick particle model similar to Chungen *et al.* (2010). Thermophoretic forces, more accurate drag coefficients as recommended by Du Toit (2015) and non-spherical heat and mass transfer correlations should be applied to the particles. The inclusion of inter-particle effects such as packing and heat transfer are also required in the bed volume on the grate of the boiler simulation. Streak formation above the bed can be accounted for as per Shiehnejadhesar *et al.* (2015).

11. Conduct a measurement campaign in the area of the grate in order to validate the refinement of the bed model.

Appendices

Appendix A

ROM vs Bio-CPD

The volatile yields at different temperatures of ANN-Bio-CPD and Bio-CPD are compared in Figures A.1, A.2 and A.3 for cellulose, hemicellulose and lignin, respectively.

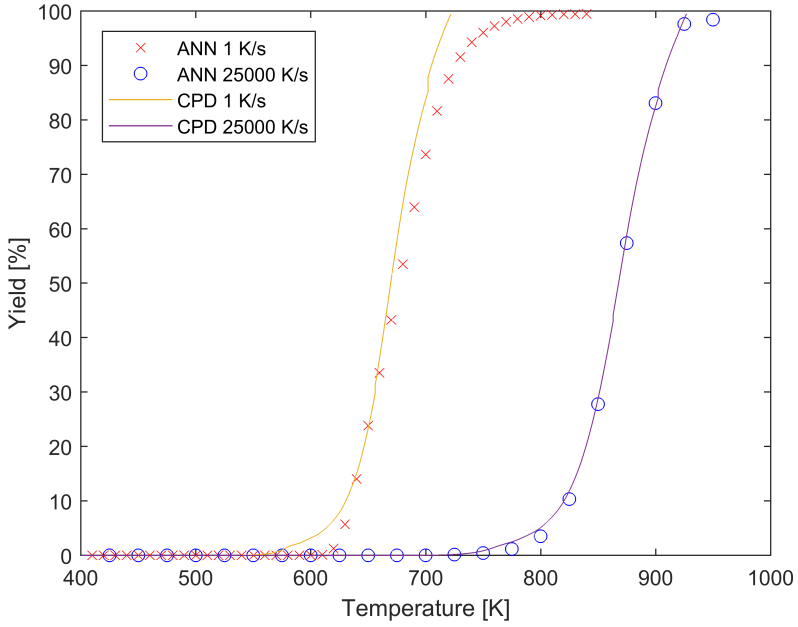

Figure A.1: ANN vs Bio-CPD for cellulose

Good correlation between ANN-Bio-CPD and Bio-CPD can be seen. The largest discrepancy is for cellulose at the upper range of the conversion and lowest heating rate.

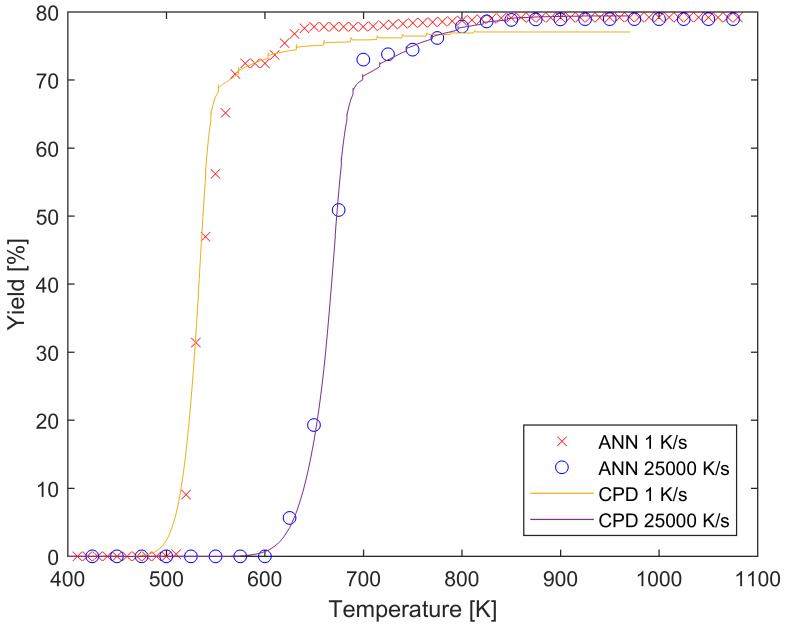

Figure A.2: ANN vs Bio-CPD for hemicellulose

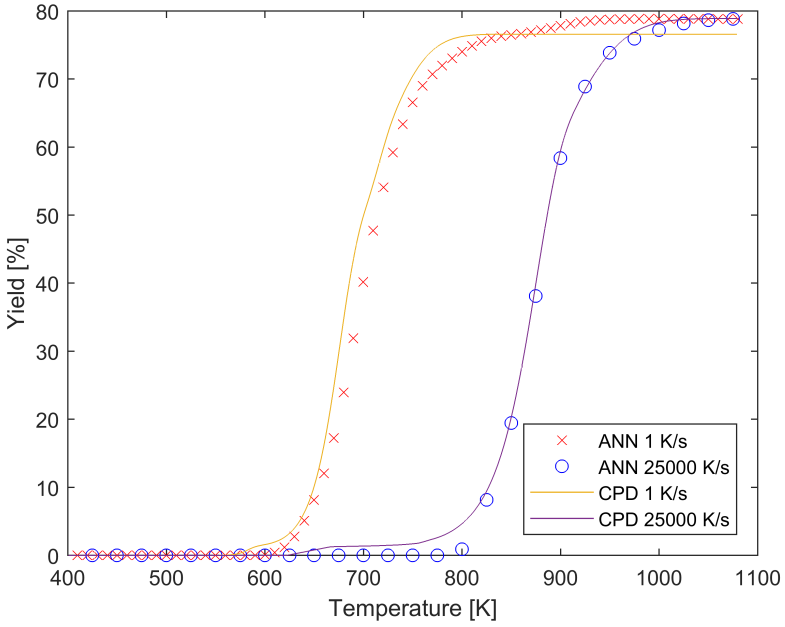

Figure A.3: ANN vs Bio-CPD for lignin

There is a slight difference in maximum volatile yield between the two heating rates for hemicellulose and lignin of Bio-CPD not seen for ANN-Bio-CPD. The reason is because ANN-Bio-CPD has been normalised with the maximum volatile yield, which is for 25 000 K/s, to reduce computational effort. The slight difference was not worth the extra computational cost. When the Bio-CPD model is improved to account for the larger, more realistic difference in volatile yield at higher heating rates, the code can be adjusted to access the ANN a third time for each component in order to normalise the rate with the maximum yield at the specific heating rate. This will allow a larger yield for higher heating rates and not the same yield as is the current implementation.

Appendix B

ROM CFD implementation additional information

The implementation of ANN-Bio-CPD with the DEFINE_PR_RATE macro follows:

All the sequential sub-processes of the particle phase take place as normal according to the standard Fluent wet combustion set up, apart from devolatilisation and char combustion, which are customised.

In the material panel for the bagasse combusting particle, the volatile percentage is specified as zero and instead grouped together with the combustible material. The swelling factor is also specified as 1. The multiple surface reactions combustion model is selected.

Solid carbon- and solid bagasse volatile material are created. The molecular weight and enthalpy of formation of the solid bagasse volatile material is the same as the gaseous bagasse volatile material. The specific heat of both solid materials is also equal to the particle material.

In the species transport panel, particle surface reactions are enabled. The chemical reactions for the devolatilisation and char combustion are added to the reaction mechanism as particle surface reactions after adding the solid species to the gas mixture.

In the injection panel, the fractions of char and volatiles are specified under the multiple surface reaction tab. These values are calculated based on the fractions of cellulose, hemicellulose and lignin in the fuel.

The DEFINE_PR_RATE macro is used to specify custom particle surface reaction rates in order to update the mass. IF statements are used to initiate char combustion after devolatilisation. Equation (3.25) is used for char combustion. The rate from the DEFINE_DPM_SCALAR_UPDATE macro based on Equation (4.3) for the three components is used for devolatilisation.

The particle diameter and density are updated during devolatilisation based on the swelling coefficient with the DEFINE_DPM_SCALAR_UPDATE macro.

The heat transfer during devolatilisation and char combustion is described by Equation (3.17) with added terms, as explained in Section 3.2.

The chemical reaction for devolatilisation allows the release of multiple species from the particle surface instead of a pseudo volatile that needs to be broken into species with a pseudo gas phase reaction.

The approach explained in the preceding paragraphs was also used with Equation (3.23) for the single rate instead of Equation (4.3) in order to compare the results to the standard Fluent setup. The results were the same for the DTF and boiler combustion simulations, validating the implementation.

Appendix C

University of Twente DTF temperature profile

The temperature contours on a plane through the centre line of the DTF CFD simulation is shown in Figure C.1. The temperature profile on the centre line over the length of the reactor is given in Figure C.2. The reactor wall temperature was 773 K.

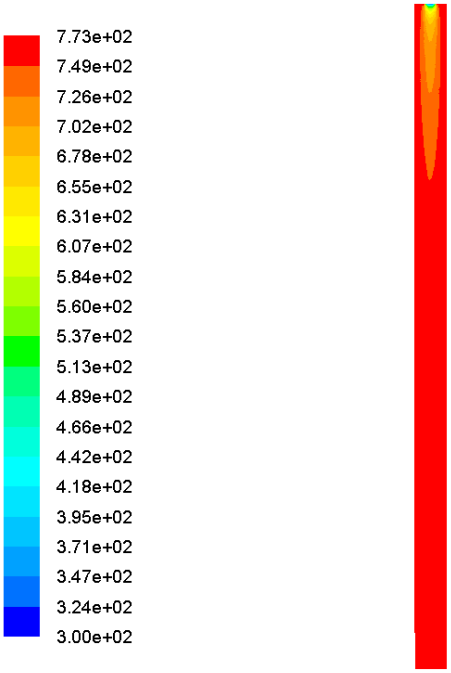

Figure C.1: Temperature contours [K]

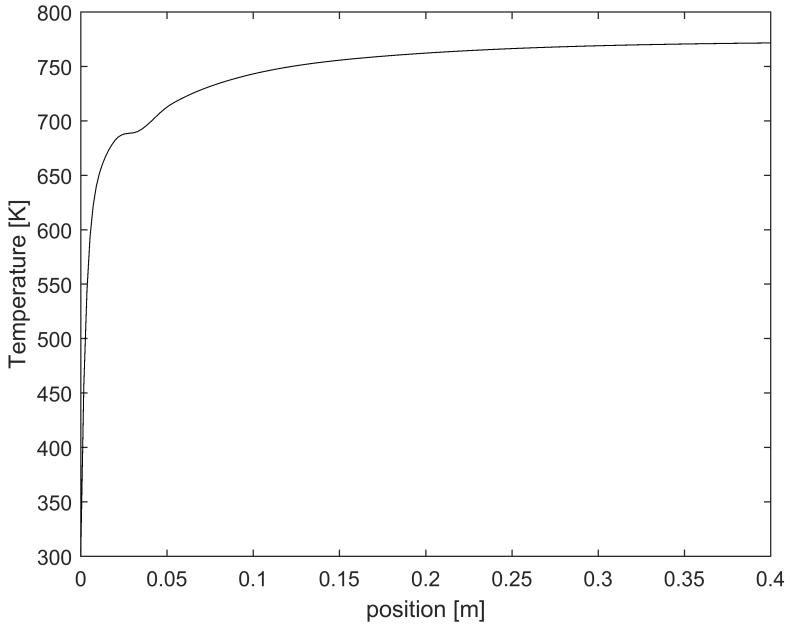

Figure C.2: Temperature profile on centre line [K]

It is clear that using an isothermal temperature profile as the approach of Lewis and Fletcher (2013) can lead to higher devolatilisation yields compared to the CFD model, especially in the first third section of the DTF.

Appendix D

Northeastern University DTF additional information

D.1 Species release for GRI 3.0

A volatile pseudo molecule was split into the constituting species suitable for the GRI 3.0 reaction mechanism by balancing the elements and using the amount of CO_2 to balance the energy:

$$CH_{1.85}O_{0.94}N_{0.0068} \rightarrow aCH_4 + bH_2 + cCO + dHCN + eNH_3 + fCO_2 \quad \text{(D.1)}$$

The table below contains the stoichiometric balance coefficients for the reaction (D.1).

Table D.1: Species breakdown

a	0.45531
b	0.00621
c	0.14837
d	0.00068
e	0.0061
f	0.39564

The split between the NO_x precursors was taken as 0.9 NH_3 and 0.1 HCN which is similar to the research of Chungen *et al.* (2010) and in accordance with low-rank coal [Ranade and Gupta (2015)].

The pseudo volatile molecule, $CH_{1.85}O_{0.94}N_{0.0068}$, with molecular weight of 29 kg/kmol is based on the following ASTM proximate - and ultimate analysis of bagasse from Riaza *et al.* (2014):

Table D.2: Proximate analysis

Moisture [%wt, dry]	0
Fixed carbon [%wt, dry]	8
Volatiles [%wt, dry]	87.8
Ash [%wt, dry]	4.2

Table D.3: Ultimate analysis

C [%wt, dry ash free]	46.3
H [%wt, dry ash free]	5.9
O [%wt, dry ash free]	47.5
N [%wt, dry ash free]	0.3

Based on the higher heating value (HHV) of the dried bagasse sample of 16300 kJ/kg the enthalpy of formation of the pseudo molecule was calculated as -2.064×10^8 J/kmol.

D.2 Temperature profile

The temperature contours on a plane through the centre line of the DTF CFD simulation is shown in Figure D.1. The temperature profile on the centre line over a third of the length of the reactor is given in Figure D.2. The reactor wall temperature was set at 1 400 K in the CFD simulation, as measured by embedded thermocouples in the wall.

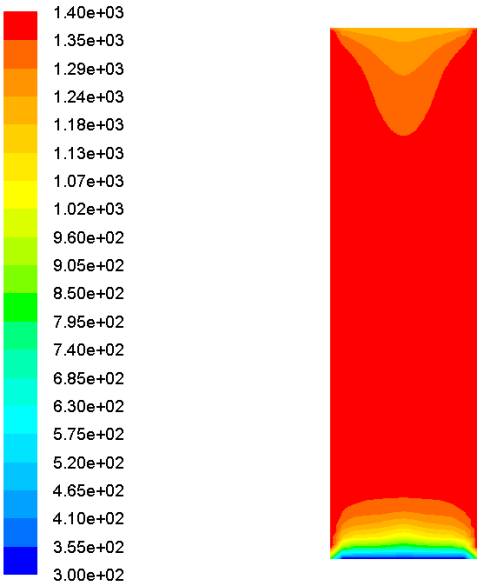

Figure D.1: Temperature contours [K]

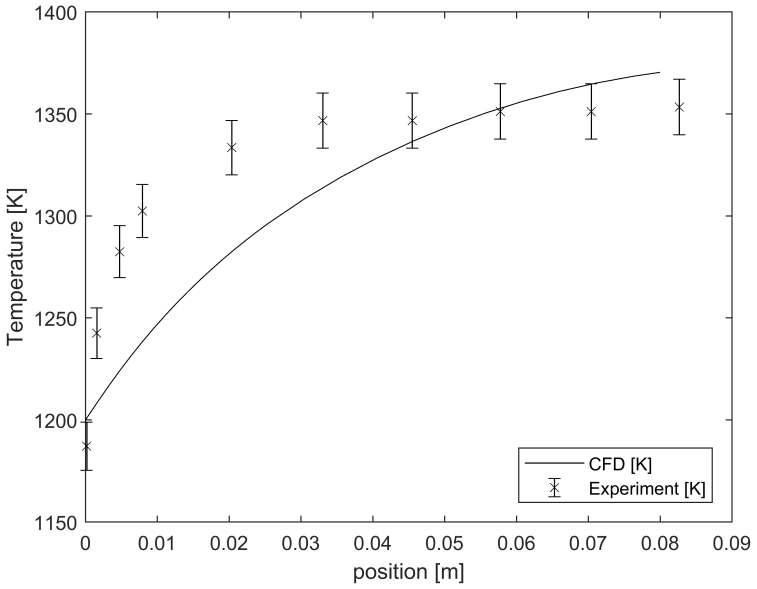

Figure D.2: Temperature profile on centre line [K]

The maximum deviation of the CFD model from the measurements was 4.9 %. Since a bare thermocouple was used and the measurements corrected for radiation effects, it is within acceptable agreement. A suction pyrometer would be the appropriate piece of measuring equipment at these high temperatures; however, it could not be used in the absence of flow.

D.3 Results

Three kinetic rates with the single-rate devolatilisation model are compared in Figure D.3 and Figure D.4.

A kinetic rate recommended by Stubington and Aiman (1994) for the single-rate model delivered a volatile flame duration that is three times the experimental value and a delay to ignition that is twice the duration of the results with the rate of Gera *et al.* (1999). Another kinetic rate from Drummond and Drummond (1996) produced a similar extended delay to ignition.

The rate of Stubington and Aiman (1994) produced the lowest peak particle temperature of 2 003 K and the rate of Drummond and Drummond (1996) delivered the highest particle temperature of 2 062 K.

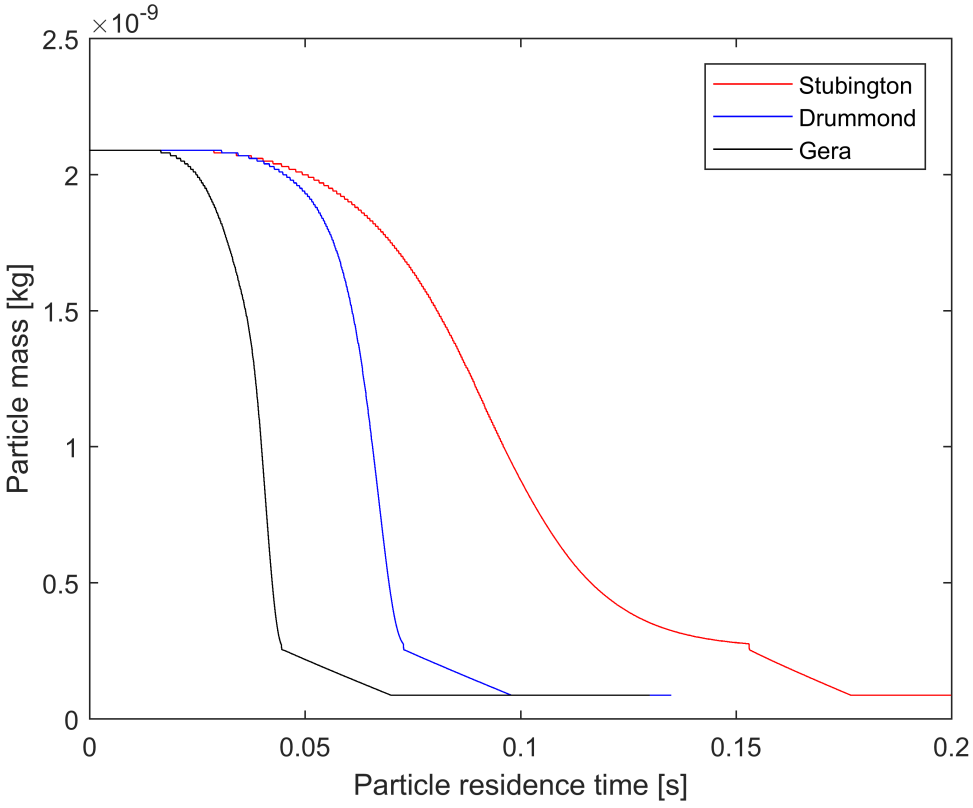

Figure D.3: Particle mass as a function of residence time

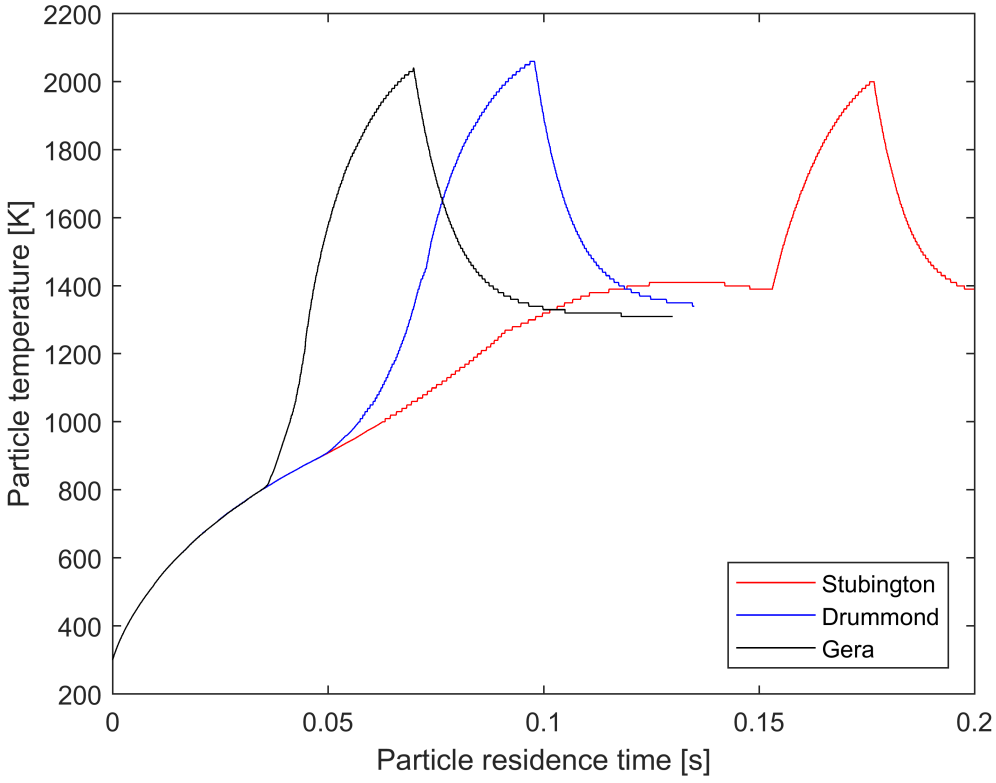

Figure D.4: Particle temperature as a function of residence time

Appendix E

Boiler simulation additional information

E.1 Reaction mechanism

A two-step quasi-global mechanism with a very fast first step and the CO oxidation rate of Howard *et al.* (1973) was used in this study. The following describes the mechanism:

$$\begin{aligned} (1) \quad CH_{1.92}O_{0.91}N_{0.0423} + 0.52O_2 &\rightarrow CO + 0.96H_2O + 0.0211N_2 \\ (2) \quad CO + 0.5O_2 &\rightarrow CO_2 \end{aligned} \tag{E.1}$$

The table below contains the kinetic data for the reaction mechanism in (E.1).

Table E.1: Two-step reaction mechanism kinetic data

No.	A [s^{-1}]	β	E_a [J/kg]	Reaction order
1	2.119×10^6	0	0	$[CH_{1.92}O_{0.91}N_{0.0423}][O_2]$
2	1.3×10^{11}	0	1.26×10^8	$[CO][O_2]^{0.5}[H_2O]^{0.5}$

The pseudo volatile molecule, $CH_{1.92}O_{0.91}N_{0.0423}$, with molecular weight of 29.2 kg/kmol is based on the following ASTM proximate- and ultimate analysis of bagasse:

Table E.2: Proximate analysis

Moisture [%wt, as received]	47.06
Fixed carbon [%wt, as received]	5.57
Volatiles [%wt, as received]	43.96
Ash [%wt, as received]	3.41

Table E.3: Ultimate analysis

C [%wt, dry ash free]	47.7
H [%wt, dry ash free]	5.9
O [%wt, dry ash free]	44.6
N [%wt, dry ash free]	1.8

Based on the HHV of the as-received bagasse sample of 9 890 kJ/kg the enthalpy of formation of the pseudo molecule was calculated as -1.327×10^8 J/kmol.

E.2 Heat transfer

The heat transfer to the different boiler components can be seen in Table E.4. It indicates a faster CO reaction and resulting higher temperatures upstream from the superheater with the default EDC model constants compared to the modified constants. The latter are closer to the CFD results of Du Toit (2015) with regard to furnace heat transfer, which were obtained with a tuned EDM.

It can also be seen that the modified EDC results in 7.7% over-prediction in superheater performance compared to the lumped parameter model. Therefore, the amount of fouling used by Du Toit (2015) to tune the model to the correct superheater performance would have to be revised slightly when using the EDC.

Table E.4: Heat transfer to various boiler components

	Lump	MSc	EDC1 SR	EDC1 ANN	EDC2 SR	EDC2 ANN
Heat absorbed in furnace [kW]	21533	12107	16054	15274	13019	13204
Heat absorbed in superheater [kW]	9167	9032	9367	9409	9748	9870
Convective heat transfer [%]	58	67	75	75	76	76
Radiative heat transfer [%]	42	33	25	25	24	24
Heat absorbed in cavity [kW]	254	1132	755	788	967	796
Heat absorbed in main bank [kW]	22173	29605	24871	25530	27150	27573
Sum Total [kW]	53127	51876	51147	51101	50984	51543
Furnace gas outlet temperature [K]	1250	1239	1245	1255	1227	1235
Superheater gas outlet temperature [K]	1098	1224	1130	1147	1181	1192
Mainbank gas outlet temperature [K]	669	699	672	678	692	693

With reference to Table E.4:

- Lump — Lumped parameter model of boiler from Du Toit (2015)
- Msc — CFD results from Du Toit (2015)
- EDC1 SR — EDC with default constants and single rate devolatilisation model
- EDC1 ANN — EDC with default constants and ANN-Bio-CPD devolatilisation model
- EDC2 SR — EDC with modified constants and single rate devolatilisation model
- EDC2 ANN — EDC with modified constants and ANN-Bio-CPD devolatilisation model

List of References

Aminian, J. and Galetti, C. (2012). Numerical investigation of a mild combustion burner: analysis of mixing field, chemical kinetics and turbulence-chemistry interaction. *Flow Turbulence Combustion*, vol. 88, pp. 597–623.

Andersen, J. (2009). *Experimental and CFD investigation of gas phase freeboard combustion*. Ph.D. thesis, Technical University of Denmark.

ANSYS (2016). *FLUENT documentation*.

Awais, M.M., Godoy, S. and Lockwood, F.C. (1999). The development of a neural network model for NO_x predictions based on a flat flame turbulent jet apparatus. In: *Fifth International Conference on Technologies and Combustion for a Clean Environment*, vol. II, pp. 825–837.

Bao, H. (2017). *Development and validation of a new eddy dissipation concept (EDC) model for MILD combustion*. Master's thesis, TUDelft.

Barlow, R.S. and Frank, J.H. (1998). Effects of turbulence on species mass fractions in methane / air jet flames. *Symposium (International) on Combustion*, vol. 27, pp. 1087–1095.

Baum, M.M. and Street, P.J. (1971). Predicting the combustion behavior of coal particles. *Combust. Sci. Tech.*, vol. 3, no. 5, pp. 231–243.

Biagini, E. (2003). *Energy and material recovery by thermal treatment of biomasses and wastes (co-combustion, pyrolysis and gasification)*. Ph.D. thesis, University of Pisa.

Biagini, E., Falcitelli, M. and Tognotti, L. (2006). Devolatilisation and pyrolysis of biomasses: Development and validation of structural models. In: *Meeting on Combustion*.

Bramer, E.A. (2017). Drop tube furnace. Tech. Rep., University of Twente.

Brink, A. (1998). *Eddy break-up based models for industrial diffusion flames with complex gas phase chemistry*. Ph.D. thesis, Abo Akademi University.

Brink, A., Boström, S., Kilpinen, P. and Hupa, M. (2001). Modeling nitrogen chemistry in the freeboard of biomass-fbc. *IFRF Combustion Journal*.

Chungen, Y., Kaer, S.K., Rosendahl, L. and Hvid, S.L. (2010). Co-firing straw with coal in a swirl-stabilised dual-feed burner: Modelling and experimental validation. *Bioresource Technology*, vol. 101, pp. 4169–4178.

Da Silva, A.B. (2008). Review of devolatilisation models and their application to pulverised fuel combustion simulation. Tech. Rep., Instituto Superior Tecnico.

De, A., Oldenhof, E., Sathiah, P. and Roekaerts, D. (2011). Numerical simulation of delft-jet-in-hot-coflow (DJHC) flames using the eddy dissipation concept model for turbulence chemistry interaction. *Flow Turbulence Combusiton*, vol. 87, pp. 537–567.

Deidda, A., Grassi, C. and Tognotti, L. (2001). A neural approach for biomass devolatilisation in comprehensive modelling of industrial combustion systems. In: *Proceedings of the International Conference on Industrial Application of Neural Networks*.

Drummond, A.F. and Drummond, I.W. (1996). Pyrolysis of sugar cane bagasse in a wire-mesh reactor. *Industrial & Engineering Chemistry Research*, vol. 35, pp. 1263–1268.

Du Toit, P.C. (2015). *The development and validation of a computational fluid dynamics model of an industrial watertube boiler burning bagasse*. Master's thesis, Stellenbosch University.

Ertesvag, I.S. and Magnussen, B.F. (1999). The eddy dissipation turbulence energy cascade model. *Combustion Science and Technology*, vol. 159, pp. 213–235.

Evans, M.J., Medwell, P.R. and Tian, Z.F. (2015). Modeling lifted jet flames in a heated coflow using an optimised eddy dissipation concept model. *Combustion Science and Technology*, vol. 187, pp. 1093–1109.

Farokhi, M. and Birouk, M. (2016*a*). Application of eddy dissipation concept for modeling biomass combustion, part1: Assessment of model coefficients. *Energy & Fuels*, vol. 30, no. 12, pp. 10789–10799.

Farokhi, M. and Birouk, M. (2016*b*). Application of eddy dissipation concept for modeling biomass combustion, part2: Gas-phase combustion modeling of a small scale fixed bed furnace. *Energy & Fuels*, vol. 30, no. 12, pp. 10800–10808.

Farokhi, M.and Birouk, M. and Tabet, F. (2017). A computational study of a small-scale biomass burner: the influence of chemistry, turbulence and combustion sub-models. *Energy Conversion and Management*, vol. 143, pp. 203–217.

Fletcher, T.H., Kerstein, A.R., Pugmire, R.J. and Grant, D.M. (1990). Chemical percolation model for devolatilization: 2. temperature and heating rate effects on product yields. *Energy & Fuels*, vol. 4, no. 1, pp. 54–60.

Fletcher, T.H., Kerstein, A.R., Pugmire, R.J., Solum, M. and Grant, D.M. (1992). A chemical percolation model for devolatilisation: summary. techreport, Sandia National Laboratories.

Fletcher, T.H., Pond, H.R., Webster, J., Wooters, J. and Baxter, L. (2012). Prediction of tar and light gas during pyrolysis of black liquor and biomass. *Energy & Fuels*, vol. 26, no. 6, pp. 3381–3387.

Gera, D., Mathur, M.P., Freeman, M.C. and Robinson, A.L. (1999). A numerical study of the effects of biomass coal cofiring on unburned carbon and NO_x emissions. In: *American flame reserach committee (AFRC) fall symposium.*

Gran, I.R., Melaaen, M.C. and Magnussen, B.F. (1994). Numerical simulation of local extinction effects in turbulent combustor flows of methane and air. In: *Twenty-Fifth Symposium (International) on Combustion. The Combustoin Institute*, vol. 25, pp. 1283–1291.

Grotkjaer, T., Dam-Johansen, K., Jensen, A.D. and Glarborg, P. (2003). An experimental study of biomass ignition. *Fuel*, vol. 82, pp. 825–833.

Guillas, S., Glover, N. and Malki-Epshtein, L. (2014). Bayesian calibration of the constants of the k-epsilon turbulence model for a CFD model of street canyon flow. *Computer methods in applied mechanics and engineering*, vol. 279, pp. 536–553.

Hagan, M. and Menhaj, M. (1999). Training feed-forward networks with the marquardt algorithm. *IEEE Transactions on Neural Networks*, vol. 5, pp. 989–993.

Hagan, T. and Demuth, H.B. (2014). *Neural network design.* 2nd edn. PWS Publishing Co.

Haider, A. and Levenspiel, O. (1989). Drag coefficient and terminal velocity of spherical and nonspherical particles. *Powder Technology*, vol. 58, pp. 63–70.

Hill, S.C. and Smoot, L.D. (2000). Modeling of nitrogen oxide formation and destruction in combustion systems. *Progress in Energy and Combustion Science*, vol. 26, pp. 417–458.

Houkema, M., Fryda, L., van de Kamp, W., Riley, G., Smart, M., Whitehouse, M., Kakietek, S., Miliewska, A., Brinker, S. and Azevedo, J.L.T. (2012). Application of the biomass, oxyfuel and flameles combustion for the utilisation of pulverised coal for electricity generation. Tech. Rep., Reseach fund for coal and steel.

Howard, J.B., Williams, G.C. and Fine, D.H. (1973). Kinetics of carbon monoxide oxidation in postflame gases. In: *14th Symposium on Combustion, Combustion Institute.*

Jessee, J.P., Gansman, R.F. and Fiveland, W.A. (1993). Calculation of chemical reacting flow using finite kinetics. *Heat transfer in Fire and Combustion Systems*, vol. 250, pp. 43–53.

Jordan, C. and Harasek, M. (2011). Improvement of a combustion unit based on a grate furnace for granular dry solid biofuels using CFD methods. *Heat Transfer Engineering*, vol. 31, pp. 774–781.

Kaer, S.K. (2001). *Numerical investigation of ash deposition in straw-fired boilers*. Ph.D. thesis, Aalborg University.

Khatami, R. and Levendis, Y.A. (2015). An overview of coal rank influence on ignition and combustion phenomena at the particle level. *Combustion and Flame*, vol. 164, pp. 22–34.

Kim, S.E. and Choudhury, D. (1995). A near wall treatment using wall functions sensitized to pressure gradient. *ASME FED Seperated and complex flows*, vol. 217.

Kjäldman, L., Brink, A. and Hupa, M. (1999). Micro mixing time in the eddy dissipation concept. *Combustion Science and Technology*, vol. 154, pp. 207–227.

Klason, T. and Bai, X.S. (2006). Computational study of the combustion process and *NO* formation in a small-scale wood pellet furnace. *Fuel*, vol. 86, pp. 1465–1474.

Kuo, K.K. (1986). *Principles of Combustion*. 1st edn. Wiley.

Kuo, K.K. (2005). *Principles of combustion*. 2nd edn. Wiley.

Lapp, M., Drake, M., Penney, C.M., Pitz, R.W. and Correa, S. (1983). Turbulent combustion experiments and modeling. Final report, Power Systems Division, U.S. Dept. Energy.

Laubscher, R. (2017). *Utilization of artificial neural networks to resolve chemical kinetics in turbulent fine structures of an advanced CFD combustion model*. Ph.D. thesis, Stellenbosch University.

LeCun, Y., Bottou, L. and Orr, G.B. (1998). *Neural networks: Tricks of the trade*. Springer-Verlag Berlin Heidelberg.

Lewis, A.D. (2011). *Sawdust pyrolysis and petroleum coke CO_2 gasification at high heating rates*. Masters, Brigham Young University.

Lewis, A.D. (2014). *Gasification of biomass, coal and petroleum coke at high heating rates and elevated pressure*. Ph.D. thesis, Brigham Young University.

Lewis, A.D. and Fletcher, T.H. (2013). Prediction of sawdust pyrolysis yields from a flat-flame burner using the CPD model. *Energy & Fuels*, vol. 27, pp. 942–953.

Lins, C. (2016). Renewables 2016 global status report. Tech. Rep., REN21.

Lysenko, D., Ertesvag, I.S. and Rian, K.E. (2014). Numerical simulations of the Sandia flame D using the eddy dissipation concept. *Flow Turbulence Combustion*, vol. 93, pp. 665–687.

Magel, H., Schneider, R., Risio, B., Schnell, U. and Hein, K.R.G. (1995). Numerical simulation of utility boilers with advanced combustion technologies. In: *Eighth International Symposium on Transport Phenomena in Combustion.*

Magnussen, B. (2005). The eddy dissipation concept a bridge between science and technology. In: *ECCOMAS Thematic Conference on Computational Combustion.*

Magnussen, B.F. (1981). On the structure of turbulence and a generalised eddy dissipation concept for chemical reaction in turbulent flow. In: *19th American Institute of Aeronautics and Astronautics Aerospace Science Meeting.*

Magnussen, B.F. and Hjertager, B.H. (1976). On mathematical models of turbulent combustion with special emphasis on soot formation and combustion. *16th Symposium (International) on Combustion. The Combustion Institute.*

Marquardt, D.W. (1963). An algorithm for least-squares estimation of nonlinear parameters. *SIAM Journal on Applied Mathematics*, vol. 11, pp. 431–441.

Mehrabian, R., Shiehnejadhesar, A., Scharler, R. and Obernberger, I. (2014). Multiphysics modelling of packed bed biomass combustion. *Fuel*, vol. 122, pp. 164–178.

Mei, Z., Mi, J., Wang, F. and Zheng, C. (2012). Dimensions of CH_4-jet flame in hot O_2/CO_2 coflow. *Energy and Fuels*, vol. 26, pp. 3257–3266.

Meldgaard, T. (2009). *Numerical investigation with detailed chemistry of CO reduction in biomass combustion.* Master's thesis, Aalborg University.

Miller, R.S., Harstad, K. and Bellan, J. (1998). Evaluation of equilibrium and non-equilibrium evaporation models for many droplet gas-liquid flow simulations. *International Journal of Multiphase Flow*, vol. 24, pp. 1025–1055.

Miltner, M., Makaruk, A., Harasek, M. and Friedl, A. (2006). CFD-modelling for the combustion of solid baled biomass. In: *Fifth International Conference on CFD in the Process Industries.*

Muller, S., Milano, M. and Koumoutsakos, P. (1999). Application of machine learning algorithms to flow modelling and optimisation. Tech. Rep., Center of Turbulence Research.

Myhrvold, T., Ertesvag, I.S. and Gran, I.R. (2003). Modeling turbulent reacting near-wall flow. In: *Joint Meeting if the Scandinavian-Nordic and Italian Sections of the Combustion Institute.*

Norman, T., Andersen, P. and Madsen, O.H. (2012). Development of an improved secondary air system using CFD. In: *Fourth International Symposium on Energy from Biomass and Waste.*

Orszag, S., Yakhot, V., Flannery, W., Boysan, F., Choudhury, D., Maruzewski, J. and Patel, B. (1993). Renormalisation group modelling and turbulence simulations. In: *International Conference on Near-Wall Turbulent Flows*.

Panahi, A., Levendis, Y.A., Vorobiev, N. and Schiemann, M. (2017). Direct observations on the combustion characteristics of Miscanthus and beechwood biomass including fusion and spherodization. *Fuel Processing Technology*, vol. 166, pp. 41–49.

Parente, A., Malik, M.R., Contino, F., Cuoci, A. and Dally, B.B. (2016). Extension of the eddy dissipation concept for turbulence/chemistry interaction to mild combustion. *Fuel*, vol. 163, pp. 98–111.

Peters, A.A. and Weber, R. (1995). Mathematical modeling of a 2.25 MWt swirling natural gas flame part1: eddy break-up concept for turbulent combustion; probability density approach for nitric oxide formation. *Combustion Science and Technology*, vol. 110, pp. 67–101.

Prince, D.R. (2014). *Measurement and modeling of fire behaviour in leaves and sparse shrubs*. Ph.D. thesis, Brigham Young University.

Rabacal, M., Costa, M., Vascellari, M. and Hasse, C. (2014). Kinetic modelling of sawdust and beech wood pyrolysis in drop tube reactors using advanced predictive models. *Chemical Engineering Transactions*, vol. 37, pp. 79–84.

Ragland, K.W. and Aerts, D.J. (1991). Properties of wood for combustion analysis. *Bioresource Technology*, vol. 37, pp. 161–168.

Ranade, V.V. and Gupta, D.F. (2015). *Computational modeling of pulverized coal fired boilers*. Taylor & Francis Group.

Ranz, W.E. and Marshall, W.R. (1952*a*). Evaporation from drops, part i and part ii. *Chem. Eng. Prog*, vol. 48, pp. 173–180.

Ranz, W.E. and Marshall, W.R. (1952*b*). Vaporation from drops, part i. *Chem. Eng. Prog.*, vol. 48, pp. 141–146.

Rehm, M., Seifert, P. and Meyer, B. (2008). Theoretical and numerical investigation on the EDC-model for turbulence-chemistry interaction at gasification conditions. *Computers & Chemical Engineering*, vol. 33, pp. 402–407.

Riaza, J., Khatami, R., Levendis, Y.A., Álvarez, L., Gil, M.V., Pevida, C., Rubiera, F. and Pis, J.J. (2014). Combustion of single biomass particles in air and oxy-fuel conditions. *Biomass & Bioenergy*, vol. 64, pp. 162–174.

Roache, P.J. (1997). Quantification of uncertainty in computational fluid dynamics. *Annu. Rev. Fluid. Mech.*, vol. 29, pp. 123–160.

Rose, J.W. and Cooper, J.R. (1977). *Technical data on fuel.* 7th edn. Wiley.

Sazhin, S.S. (2006). Advanced models of fuel droplet heating and evaporation. *Progress in Energy and Combustion*, vol. 32, pp. 162–214.

Scharler, R., Benesch, C., Schulze, K. and Obernberger, I. (2011). CFD simulations as efficient tool for the development and optimisation of small-scale biomass furnaces and stoves. In: *The proceedings of the 19th European Biomass Conference and Exhibition.*

Scharler, R., Widmann, E. and Obernberger, I. (2004). CFD modelling of NO_x formation in biomass grate furnaces with detailed chemistry. In: *6th International Conference, Science in thermal and chemical biomass conversion.*

Schmidt, U., Rexroth, C.H., Scharler, R. and Cremer, I. (2013). New trends in combustion simulation.

Sheng, C. and Azevedo, J.L.T. (2002). Modelling biomass devolatilization using the chemical percolation devolatilisation model for the main components. In: *Proceedings of the Combustion Institute*, vol. 29, pp. 407–414.

Shiehnejadhesar, A., Mehrabian, R., Scharler, R., Goldin, G.M. and Obernberger, I. (2014). Development of a gas phase combustion model suitable for low and high turbulence conditions. *Fuel*, vol. 126, pp. 177–187.

Shiehnejadhesar, A., Scharler, R., Mehrabian, R. and Obernberger, I. (2015). Development and validation of CFD models for gas phase reaction in biomass grate furnaces considering gas streak formation above the packed bed. *Fuel Processing Technology*, vol. 139, pp. 142–158.

Shih, T.H., Liou, W.W., Shabbir, A., Yang, Z. and Zhu, J. (1995). A new k-epsilon eddy viscosity model for high reynolds number turbulent flows - model development and validation. *Computers Fluids*, vol. 24, pp. 227–238.

Stubington, J.F. and Aiman, S. (1994). Pyrolysis kinetics of bagasse at high heating rates. *Energy & Fuels*, vol. 8, pp. 194–203.

Versteeg, H.K. and Malalasekera (2007). *An introduction to computational fluid dynamics, the finite volume method.* 2nd edn. Pearson Educational Limited.

Vizzini, G., Bardi, A., Biagini, E., Falcitelli, M. and Tognotti, L. (2008). Prediction of rapid biomass devolatilization yields with an upgraded version of the Bio-CPD model. In: *Meeting on Combustion.*

Wagenaar, B.M., Prins, W. and van Swaaij, W.P.M. (1993). Flash pyrolysis kinetics of pine wood. *Fuel Processing Technology*, vol. 36, pp. 291–298.

Wang, J., Wu, J., Ling, J., Iaccarino, G. and Xiao, H. (2017). A comprehensive physics informed machine learning framework for predictive turbulence modeling. Submitted to Elsevier.

Westbrook, C.K. and Dryer, F. (1981). Simplified reaction-mechanisms for the oxidation of hydrocarbon fuels in flames. *Combustion Science and Technology*, vol. 27, pp. 31–43.

Weydahl, T., Bugge, M., Gran, I.R. and Ertesvag, I.S. (2002). Computational modeling of nitric oxide formation in biomass combustion. Tech. Rep., Norwegian University of Science and Technology.

Winston, P.H. (1993). *Artificial intelligence*. 3rd edn. Addison-Wesley Publishing company.

Yarlanki, S., Rajendran, B. and Hamann, H. (2012). Estimation of turbulence closure coefficients for data centers using machine learning algorithms. In: *13th IEEE ITHERM Conference*.

Yin, C., Rosendahl, L., Kaer, S.K., Clausen, S., Hvid, S.L. and Hille, T. (2008). Mathematical modeling and experimental study of biomass combustion in a thermal 108 MW grate-fired boiler. *Energy & Fuels*, vol. 22, pp. 1380–1390.

Zahirovic, S., Scharler, R. and Obernberger, I. (2006). Advanced gas phase combustion models: validation for biogases by means of les and experiments as well as application to biomass furnaces. In: *7th European Conference on Industrial Furnaces and Boilers*.

Zhao, S., Fang, Q., Yin, C., Wei, T., Wang, H., Zhang, C. and Chen, G. (2017). New fuel air control strategy for reducing NO_x emissions from corner-fired utility boilers at medium -low loads. *Energy & Fuels*, vol. 31, pp. 6689–6699.